NAVAL POSTGRADUATE SCHOOL
Monterey, California

THESIS

A NUMERICAL STUDY OF THE FORCING MECHANISMS OF THE LEEUWIN CURRENT SYSTEM

by

Richard A. Kennedy, Jr.

September 2002

Thesis Advisor: Mary L. Batteen
Second Reader: Curtis A. Collins

Approved for public release; distribution is unlimited.

THIS PAGE INTENTIONALLY LEFT BLANK

REPORT DOCUMENTATION PAGE

Form Approved OMB No. 0704-0188

1. AGENCY USE ONLY ***(Leave blank)***	**2. REPORT DATE**	**3. REPORT TYPE AND DATES COVERED**
	September 2002	Master's Thesis

4. TITLE AND SUBTITLE A Numerical Study of the Forcing Mechanisms of the Leeuwin Current System

5. FUNDING NUMBERS

6. AUTHOR (S) LT Richard A. Kennedy, Jr.

7. PERFORMING ORGANIZATION NAME(S) AND ADDRESS(ES)
Naval Postgraduate School
Monterey, CA 93943-5000

8. PERFORMING ORGANIZATION REPORT NUMBER

9. SPONSORING / MONITORING AGENCY NAME(S) AND ADDRESS(ES)

10. SPONSORING/MONITORING AGENCY REPORT NUMBER

11. SUPPLEMENTARY NOTES The views expressed in this thesis are those of the author and do not reflect the official policy or position of the U.S. Department of Defense or the U.S. Government.

12a. DISTRIBUTION / AVAILABILITY STATEMENT
Approved for public release; distribution is unlimited.

12b. DISTRIBUTION CODE

13. ABSTRACT ***(maximum 200 words)***

To investigate the role of wind forcing, bottom topography and thermohaline gradients in the Leeuwin Current System (LCS), several experiments are conducted with a sigma coordinate primitive equation model on a beta-plane. Results show that the LCS is an anomalous eastern boundary current (EBC) that generates a coastal poleward current, an equatorward undercurrent, and highly energetic mesoscale features such as meanders and eddies. Thermohaline gradient effects were shown to be the primary mechanism in the generation of a poleward (equatorward) current (undercurrent), eddies and meanders in the LCS. Inshore of the poleward surface flow, next to the coast, wind forcing plays an important role in generating an equatorward coastal current and upwelling. Bottom topography is shown to be an important mechanism for intensifying and trapping currents near the coast, weakening subsurface currents and intensifying eddies off capes. Overall, the results of the study compare well with available observations in the LCS.

14. SUBJECT TERMS	**15. NUMBER OF PAGES**
Primitive equation model, Leeuwin Current System, currents, sigma-level, Princeton Ocean Model (POM)	117
	16. PRICE CODE

17. SECURITY CLASSIFICATION OF REPORT	**18. SECURITY CLASSIFICATION OF THIS PAGE**	**19. SECURITY CLASSIFICATION OF ABSTRACT**	**20. LIMITATION OF ABSTRACT**
Unclassified	Unclassified	Unclassified	UL

NSN 7540-01-280-5500 **Standard Form 298 (Rev. 2-89)**
Prescribed by ANSI Std. 239-18

THIS PAGE INTENTIONALLY LEFT BLANK

Approved for public release; distribution is unlimited

A NUMERICAL STUDY OF THE FORCING MECHANISMS OF THE LEEUWIN CURRENT SYSTEM

Richard A. Kennedy, Jr.
Lieutenant, United States Navy
B.S., United States Naval Academy, 1996

Submitted in partial fulfillment of the
requirements for the degree of

MASTER OF SCIENCE IN METEOROLOGY AND PHYSICAL OCEANOGRAPHY

from the

NAVAL POSTGRADUATE SCHOOL
September 2002

Author: Richard A. Kennedy, Jr.

Approved by: Mary L. Batteen
Thesis Advisor

Curtis A. Collins
Second Reader

Mary L. Batteen
Chairman, Department of Oceanography

THIS PAGE INTENTIONALLY LEFT BLANK

ABSTRACT

To investigate the role of wind forcing, bottom topography and thermohaline gradients in the Leeuwin Current System (LCS), several experiments are conducted with a sigma coordinate primitive equation model on a beta-plane. Results show that the LCS is an anomalous eastern boundary current (EBC) that generates a coastal poleward current, an equatorward undercurrent, and highly energetic mesoscale features such as meanders and eddies. Thermohaline gradient effects were shown to be the primary mechanism in the generation of a poleward (equatorward) current (undercurrent), eddies and meanders in the LCS. Inshore of the poleward surface flow, next to the coast, wind forcing plays an important role in generating an equatorward coastal current and upwelling. Bottom topography is shown to be an important mechanism for intensifying and trapping currents near the coast, weakening subsurface currents and intensifying eddies off capes. Overall, the results of the study compare well with available observations in the LCS.

THIS PAGE INTENTIONALLY LEFT BLANK

TABLE OF CONTENTS

THIS PAGE INTENTIONALLY LEFT BLANK

LIST OF FIGURES

THIS PAGE INTENTIONALLY LEFT BLANK

LIST OF TABLES

THIS PAGE INTENTIONALLY LEFT BLANK

ACKNOWLEDGEMENTS

I would like to thank Prof. Mary Batteen, my advisor, for her extraordinary guidance and commitment to helping me complete this study. Her extensive knowledge of the region was immense, along with her willingness to impart it to me, were vital to my understanding of the processes incorporated in this study. I would also like to thank Prof. Curt Collins for providing his editorial expertise and thoughtful input as my second reader. Thank you to Antonio Martinho for his willingness to spend countless hours teaching me the ins and outs of the POM model. His computer knowledge made this project possible. Thanks also to Robyn Phillips, who struggled with me through the initial steps of the numerical modeling process.

Most importantly, I would like to thank my wife, Sara, and children, Mackenzie and Jackson, for all of their support, love and encouragement. I could not have completed this study without them.

THIS PAGE INTENTIONALLY LEFT BLANK

I. INTRODUCTION

Subtropical eastern boundary currents (EBC) are usually equatorward at the surface, with poleward undercurrents, which are forced by prevailing equatorward winds. The major EBCs such as Peru, California, Benguela and Canary are distinguished by surface dynamic height fields which decrease toward the coast and near-surface isopycnals that slope upward (Wooster and Reid, 1963; McCreary et al., 1986). These systems are characterized by climatologically weak (<10 cm/s), broad (~1000 km wide) surface flow toward the equator, cold upwelled water at the surface, shallow (<30 m depth) thermoclines, and high biological production (Parrish et al., 1983) due to regions of significant upwelling. They are one component of the subtropical anticyclonic gyres, which are driven primarily by anticyclonic wind fields.

Along the coast of Western Australia, the prevailing winds are predominantly equatorward (Thompson, 1984; Godfrey and Ridgeway, 1985); however, unique to the region, is a poleward surface current known as the Leeuwin Current. Observational studies along the western coast of Australia have shown that this current is characterized by a strong (>150 cm/s at times), narrow (<100 km wide), poleward surface current that flows opposite the prevailing wind direction (Cresswell and Golding, 1980; Godfrey et al., 1986), anomalous warm water at the surface, a deep (>50 m depth) thermocline (Thompson, 1984) and lower biological production due to vast regions of downwelling (Batteen et al., 1992).

An anomalous EBC, the Leeuwin Current is driven by the uncharacteristically large thermohaline gradient along the western Australian coast. The current originates near Shark Bay and flows poleward along the continental shelf (~200 m depth) off the coast of western Australia to Cape Leeuwin (see Figure 1 for geographical locations) and then eastward into the Great Australian Bight (Cresswell and Golding, 1980). Associated with the system are near-surface isopycnals that slope downward, surface dynamic height fields that increase toward the coast, and an equatorward undercurrent (Thompson, 1984; McCreary et al., 1986). The equatorward wind stress is overwhelmed by the meridional pressure gradient created from excessive heating in the equatorial region and large amounts of cooling in the poleward region (Godfrey and Ridgway, 1985), generating the Leeuwin Current. The source for the Leeuwin Current is predominantly an alongshore steric height gradient due to tropical Pacific water from the Indonesian throughflow (Godfrey and Ridgway, 1985; Hirst and Godfrey, 1993), augmented by geostrophic inflow from the west (McCreary et al., 1986; Thompson, 1987). The poleward flow of the Leeuwin Current intensifies due to the strong inflow of the subtropical waters toward the coast (Batteen et al., 1992).

Below the Leeuwin Current, there is an anomalous equatorward current off western Australia (Church et al., 1989). This undercurrent is centered near 450 m depth and can attain speeds comparable to the surface flow, exceeding on average 10 cm/s (Smith et al., 1991). Smith et al. (1991) observed core speeds of the narrow undercurrent up to 30 cm/s between ~250 and 350 m depth and found that the current was usually confined to the continental shelf slope

between ~250 and 450 m depth. Although there is evidence of a westward flow of ~20 cm/s centered between ~400 and 700 m depth off the southern coast at 116^{o} E (Cresswell and Peterson, 1993), no studies to date have clearly resolved whether there is a westward undercurrent off Southern Australia.

Previous numerical modeling studies by Batteen et al. (1992) investigated the effects of annual climatological wind forcing and initialized thermohaline gradients on the Leeuwin Current System (LCS), but the study was limited to the coast off western Australia and did not include the influence of topography. Batteen and Huang (1998) studied the effects of salinity on the density of the LCS. Batteen and Butler (1998) examined the effects of continuously forced annual Indian Ocean thermohaline gradients on the LCS and extended the domain to include both the western and southwestern coasts of Australia. Batteen et al. (2000) investigated the effects of seasonal forcing on the LCS with a full primitive equation ocean model but again only considered flat bottom cases.

This study seeks to extend prior efforts in this area by including the addition of realistic topography, allowing a better understanding of the LCS by including the influences of topography. The Princeton Ocean Model (POM), a bottom following, sigma coordinate model, was chosen for this study because it has been widely used to simulate coastal processes associated with continental shelf flows and bottom boundary layer dynamics. The results of several numerical experiments (Table 1) are explored. Each experiment is run on a beta plane. In Experiment 1 the

horizontally averaged annual climatology is used with annual wind forcing on a flat bottom. Experiment 2 investigates the effect of thermohaline gradient forcing by using full annual climatology and no wind forcing on a flat bottom. The final flat bottom experiment, Experiment 3 includes both wind and thermohaline gradient forcing mechanisms to gain an understanding of the combined effect of the forcing mechanisms on the dynamics of the LCS. In Experiment 4, velocity errors produced by the pressure gradient force error (an error inherent in all three-dimensional, sigma coordinate models) in the presence of bottom topography are determined using horizontally averaged annual climatology with bottom topography and no wind forcing. Experiments 1 through 3 are repeated as experiments 5, 6 and 7, respectively, but with the addition of bottom topography.

Note that the results from experiments with wind forcing only, experiments 1 and 5, are more typical of classical EBCs than of the LCS. They are presented to highlight to effect of wind forcing in the absence of a thermohaline gradient. In contrast the final experiment, which includes bottom topography with annual thermohaline gradient and wind forcing, provides the most accurate representation of the LCS.

This study is organized as follows. In section II the numerical model is described along with the specific experimental conditions. The results of the numerical experiments are presented in section III, along with a discussion comparing the results to observations. A summary of the study is provided in section IV.

II. MODEL DESCRIPTION

A. DATA SETS

The model domain (Figure 1) encompasses the western and southwestern coasts of Australia, from 24.5^{o}S to 39^{o}S, and from 109^{o}W to 121^{o}W. The topographic data was obtained from the Institute of Geophysics and Planetary Physics, University of California San Diego (Sandwell and Smith, 1996). The bottom topography data set, compiled from over 30-years of bottom echo sounding by ships, has a resolution of 2 minutes (1/30 of a degree). Altimetry data was used to interpolate soundings in data sparse regions.

Annual temperature and salinity values were obtained from Levitus and Boyer (1994) and Levitus et al. (1994). These data sets incorporate a 1 by 1 degree horizontal resolution at the thirty-three vertical levels shown in Table 2.

B. PRE-PROCESSING

The original topography (Figures 2a and 2b) was interpolated to the resolution used in the POM Model, i.e., 10 km by 10 km offshore, 3 km by 10 km alongshore and 3 km by 3 km around the southwest corner of Australia with a total of 252 by 226 grid points (Figure 3). The highest resolution was used where the values of the slope parameter (defined by Mellor et al., 1998, as $\frac{|dH|}{2*\overline{H}}$, where $\overline{H}$ is the average depth and dH is the difference in depth between two adjacent cells), were the largest in both the latitude and

longitude directions. The higher resolution bands near the southwest corner of Australia were used to minimize the slope parameter (Figure 3). Since over much of the area the slope parameter was greater than 0.2, which is the suggested maximum value to be used in a sigma coordinate models (Mellor et al., 1998), the topography was first smoothed with a Gaussian filter. The new depth of each point calculated with this filter is a Gaussian-shaped, weighted average of 25 by 25 points with a standard deviation of 8. Subsequent depths greater than 2500 m were reassigned to depths of 2500m, with land assigned a depth of 20 m (to avoid divisions by zero in the model). The resulting topography is shown in Figures 4a and 4b.

The annual temperature and salinity values were interpolated for the horizontal spatial resolution of the model and for the 21 vertical sigma levels (Table 3 and Figure 5) with a three-dimensional (3D) linear interpolation scheme. This had to be done separately for smoothed topography and for flat bottom topography due to the change in vertical levels between the two data sets. Plots of annual temperature and salinity fields for the surface (sigma level one) are shown in Figures 6 and 7, respectively.

To obtain an annual non-weighted average wind vector field (Figure 8), ten years of daily seasonal winds were averaged. To be compatible with the other data fields, the wind vectors were interpolated to the same horizontal spatial resolution of the model with a 2D linear interpolation scheme.

C. BRIEF MODEL DESCRIPTION

The POM, a well documented model (e.g., Blumberg and Mellor, 1987; Mellor, 1996), was used in the model studies. POM is a primitive equation, free surface model with a second-moment turbulence closure scheme (Mellor and Yamada, 1982) that, through the use of bottom-following sigma levels, can realistically simulate processes associated with continental shelf flows and bottom boundary layer dynamics in local domains (e.g., bays, estuaries and coastal regions). Recently, the model has been used successfully to simulate decadal processes in entire ocean basins (see Ezer and Mellor, 1994, 1997).

As described earlier, the resolution of the horizontal orthogonal grid varies between 3 km by 3 km and 10 km by 10 km (Figure 3). The variable grid allows the use of more (less) points in regions of large (small) gradients.

The 21 vertical sigma levels used are shown in Figure 5 and Table 3. The sigma values range from zero at the surface to minus one at the bottom with the vertical grid spacing proportional to the ocean depth. The vertical resolution has been chosen to be higher near the surface and the bottom in order to resolve both the surface boundary layer and the bottom boundary layer, which are important in coastal regions. To eliminate the time constraints for the vertical grid related to higher resolution near surface, bottom and shallow water, an implicit vertical time differencing scheme is used.

The prognostic variables of the model are potential temperature, salinity, density, the three velocity components, surface elevation, turbulent kinetic energy and

length scale. The model has a split time step interval for external and internal modes. The external mode solves the equations for the vertically integrated momentum equations. It also provides the sea surface and barotropic velocity components, and has a time step of 6 seconds. The internal mode solves the complete 3D equations and has a time step of 300 seconds.

A Smagorinsky formulation (Smagorinsky et al., 1965) is used for the horizontal diffusion in which the horizontal viscosity coefficients depend on the grid size, the velocity gradient and a coefficient. In this study a value of 0.2 was assigned to this coefficient, consistent with other POM studies (e.g., Ezer and Mellor, 1997).

D. INITIALIZATION, FORCING AND BOUNDARY CONDITIONS

The model was initialized with annual temperature and salinity values obtained from Levitus and Boyer (1994) and Levitus et al. (1994). Since the model runs reached a quasi-equilibrium state in a relatively short time (~60 days), zero salinity and temperature fluxes were prescribed at the ocean surface. The annual climatological surface temperature (Figure 6) shows a strong north-south gradient with a maximum temperature near Shark Bay of ~24°C and a minimum of 14°C at the southern edge of the model domain. The climatological surface salinity (Figure 7) shows a maximum of ~38.9 at the center of the western edge of the model domain and a minimum of ~35.3 along the northern Australian coast. Models using horizontally averaged climatology use the same initial temperature and salinity over the entire model domain (e.g, 19.8°C and 35.39 are the

temperature and salinity values, respectively, for the surface).

The model was forced from rest with the annual European Center for Medium-range Weather Forecasting (ECMWF) wind fields, which were interpolated for the model grid. As seen in Figure 8, westerly winds dominate the southern portion of the model domain. Along the west coast of Australia the wind are southerly to south-southeasterly and generally increase in strength away from the coast.

Correct specification of the open boundary conditions (BC) is important to achieve realistic results, with no reflections, clamping, spurious currents or numerical alteration of the total volume of water in the model. The problem is that there is not a general criterion that can give the answer to what boundary conditions are the best for a specific model or study. For models with a free surface, such as used here, one of the important criteria is that the BCs should be transparent to the waves. In this model, a gradient boundary condition (Chapman, 1985), which allows geostrophic flow normal to the boundary, worked best for the elevation. For baroclinic velocity components normal to the boundary, an explicit wave radiation scheme based on the Sommerfield radiation conditions was used. For inflow situations, the model was forced with annual temperature and salinity values obtained from Levitus and Boyer (1994) and Levitus et al. (1994), while in outflow situations an advection scheme was used. An improvement on previous models, is the introduction of an advanced volume constraint subroutine based on research performed by Marchesiello et al., 2001, which drastically

reduced the loss of volume at the boundaries to insignificant levels.

For the barotropic velocity components, a Flather radiation plus Roed local solution (FRO) was used. Palma and Matano (2000) showed good results with the FRO solution during BC tests to determine the BCs response to an alongshelf wind stress. Palma and Matano (1998) also showed that the FRO BC demonstrated good reflection properties and results in a test that determined the BC response to the combined action of wind forcing and wave radiation. Their tests were executed with the barotropic version of POM and compared with the benchmark results (no boundary conditions).

III. RESULTS FROM MODEL SIMULATIONS

A. WIND FORCING ON A FLAT BOTTOM

In Experiment 1 (see Table 1), the model was initialized with the horizontally averaged annual climatological temperature and salinity. A realistic coastline and flat bottom (constant depth of 2500 m) were used, and the model was forced with annual climatological winds. The goal of this experiment was to highlight the role of wind forcing alone in the LCS.

As expected, the southerly winds along the coast have generated a weak equatorward current of ~20 cm/s (Figure 9a). By day 20, the equatorward winds induce net offshore surface Ekman transport, which generates regions of upwelling evidenced by the cool water along the coast near Shark Bay. The most intense upwelling is associated with the stronger winds in the north, but the upwelling effect is apparent all along the western coast of Australia. A typical cross-section of meridional velocity (Figure 9b), shows the core of the poleward undercurrent at ~600 m depth with a speed of ~2 cm/s underlying the equatorward surface current with a core speed of ~16 cm/s.

By day 40 (Figure 9c), the coastal upwelling has intensified bringing 18°C water to the surface near Shark Bay. In addition, the offshore extent of the coastal upwelling is much wider than at day 20. As expected, capes and promontories enhance the upwelling regions to the north. A cold core, cyclonic eddy has formed near Shark Bay. The velocity of the equatorward surface current remains at ~20 cm/s, implying that the wind has already

imparted its maximum amount of energy into the current. The width of the surface current has increased to ~50 km. Simultaneously, as the undercurrent intensifies to ~5 cm/s, it shallows and displaces the equatorward current offshore (e.g., see Figure 9d).

By day 60 (Figure 9e), the effects of upwelling are evident along the entire western coast and extend south around Cape Leeuwin. Meanders, eddies and filaments are much more apparent in the northern end of the domain where the upwelling is the most intense. Inside Shark Bay the water temperature has decreased about 2°C from the initial value at the start of the model run. The north-south velocity profile (Figure 9f), shows an eddy forming at 34.3°S, evidenced by the reversal in surface current direction.

The continued widening of the equatorward coastal jet (e.g., see Figures 9b, 9d and 9f) is consistent with the results of McCreary *et al*. (1987) and Batteen *et al*. (1989). They showed that, due to the beta (ß) effect, the surface coastal jet does not necessarily have to be confined to within a Rossby radius of deformation of the coast. The ß effect also allows the existence of freely propagating planetary waves, i.e., Rossby waves (Gill, 1982). The offshore propagation of these waves contributes to the generation of an alongshore pressure gradient field, which can aid the development of subsurface currents along the eastern boundary. As a result, the ß effect changes both the vertical and horizontal structure of the surface and subsurface currents. As the undercurrent intensifies and shoals, strong vertical and horizontal shear occurs in

the upper layers creating baroclinically and barotropically unstable coastal currents. This unstable condition leads to the development of the meanders, eddies and filaments evident in the northern end of the model domain.

The results from this experiment resemble the dynamic characteristics associated with classical EBCs, where wind forcing is the predominant forcing mechanism. Upwelling was produced due to favorable winds; however, these results were not representative of the LCS. Additional experiments will study other factors that distinguish the LCS from other EBC regions.

B. THERMOHALINE GRADIENT FORCING ON A FLAT BOTTOM

Experiment 2 (see Table 1) focuses on the thermohaline gradient. The experiment is initialized with annual climatology that has not been horizontally averaged but without wind forcing. It uses the same realistic coastline and flat bottom as in Experiment 1. This experiment introduces the conditions unique to the LCS.

In stark contrast to Experiment 1, by day 20 (Figure 10a) an energetic and dynamic poleward current has developed with a maximum velocity of ~120 cm/s. The poleward flow is evident along the entire western coast of Australia and extends around Cape Leeuwin into the Great Australian Bight. As the current rounds Cape Leeuwin it is steered eastward due to the Coriolis effect. As the current travels south, it advects warm, subtropical water with temperatures off the coast of Cape Leeuwin reaching 21°C. The strength of the surface current is created by the large north-south thermohaline gradient. The thermohaline

gradient generates a strong onshore geostrophic inflow. As the inflow nears the coast, it is deflected southward creating a narrow core of warm water along the entire coast of Western Australia. Continual onshore flow augments the poleward flow throughout the model's duration. In addition to a strong surface current, an intense equatorward undercurrent is established (e.g., see Figure 10b). The undercurrent is centered near 600 m depth with a maximum velocity of ~20 cm/s, and underlies the equatorward surface current with a core speed of ~ 80 cm/s.

By day 40 (Figure 10c), the poleward surface current has increased to ~140 cm/s. As was seen in Experiment 1, the width of the current increases due to the β effect. Warm, subtropical water has been advected farther around Cape Leeuwin, with surface temperatures off the Cape reaching 25°C. The barotropic instability of the current is enhanced by the horizontal temperature gradient and the increased strength of the current producing large horizontal shear. In addition, the undercurrent (Figure 10d) is intensifying, ~25 cm/s, and shoaling, increasing the baroclinic instability. Large meanders form south of Perth and around the coast to the east due to coastline irregularities and the instability of the current. Near Cape Leeuwin cold, sub-polar water is being entrained west of the main flow generating dipole eddy pairs, which subsequently propagate eastward along the southern coast of Australia.

By day 60 (Figure 10e), the dynamics of the current resemble those at day 40. Off of Perth the current continues to broaden due to β effects. The entrainment of

cold, subpolar water is evident in the large eddy dipole pairs. The dipole pairs are relatively flat and broad due to the β effect stretching them westward as they propagate eastward along the southern coast. The current has advected warm 25°C water well south of Cape Leeuwin. A north-south cross section (Figure 10f) dissects the eddy forming off Cape Leeuwin. The eddy is centered near 34.3°S, 113.5°W, with the broad, poleward surface current present along the coast.

The results of this experiment are more characteristic of the LCS, generating a strong poleward surface current with an equatorward undercurrent. It demonstrates the importance of the strong climatological thermohaline gradient. However, the model currents were too broad along the coast and the eddies were not very well defined.

C. WIND AND THERMOHALINE GRADIENT FORCING ON A FLAT BOTTOM

The final flat bottom experiment, Experiment 3 (see Table 1), most closely simulates the LCS by using both wind and thermohaline forcing. The model was initialized with full annual temperature and salinity climatology. In addition, annual wind forcing was added to determine the net result of both forcing mechanisms.

Similar to the no wind case, by day 20 (Figure 11a), a warm, poleward surface current has formed along the coast; however, because the wind and thermohaline forcing oppose each other, the current is not as strong as in Experiment 2 and has a maximum velocity of ~90 cm/s. Overall the dynamics and temperature advection of the current are very

similar to the results found at day 20 of Experiment 2 (Figure 10a). Additionally, a realistic equatorward undercurrent has formed off Cape Leeuwin, Lat 34.3°S, centered near 500 m depth with a speed of 20 cm/s (Figure 11b).

By day 40 (Figure 11c), the current speed has increased to 120 cm/s, consistent with the speed in Experiment 2. Again, compared to the no wind experiment (Experiment 2), the meanders and eddy formation regions are similar, with the exception of a decrease in the speed of the surface current. A typical cross-section (Figure 11d) also shows that the current does not have as wide a coastal extent as before. This can be attributed to the addition of wind forcing that opposes the thermohaline forced current and reduces its offshore extent.

Day 60 (Figure 11e) shows that although the velocity has not increased, the current broadens north of Perth, while also continuing to meander and create large eddies off Cape Leeuwin. The addition of wind forcing helps to drive equatorward flow in dipole eddy pairs making them more defined than in Experiment 2. A meridional cross-section (Figure 11f) shows generation of an eddy off Cape Leeuwin. The core of the current has moved off the coast and defines the outer edge of the eddy, with the poleward (blue shading) flow inshore of the main current. A meridional cross-section farther equatorward (Figure 11g) shows that as the main surface current leaves the coast off Perth (due to meanders or coastline irregularities), wind forcing dominates and creates an equatorward current. As expected, the equatorward flow generates regions of

upwelling which are distinguished by the slightly cooler surface temperatures off Perth and to the north of promontories, such as at ~28°S.

D. PRESSURE GRADIENT FORCE ERROR DETERMINATION

In Experiment 4, the model was initialized at rest with horizontally averaged annual climatological temperatures and salinities. A realistic coastline and bottom topography were used but no wind or thermohaline forcing was permitted.

With horizontally averaged climatology and no forcing mechanisms, we would expect that nothing will happen, i.e., the initial state of rest should be maintained. Due to pressure gradient force errors (explained below), however, this will not be the case and there will be velocities that result from these errors.

Velocity errors induced by the pressure gradient force are unavoidable in 3D sigma-coordinate models. Two types of sigma-coordinate errors exist, the sigma error of the first kind (SEFK) and of the second kind (SESK), as defined by Mellor et al. (1998). The first one goes to zero prognostically by advecting the density field to a new state of equilibrium. The second one, a vorticity error, is the most important because it does not vanish with time, and is present in both 2D and 3D cases.

There are several techniques to reduce the pressure gradient errors:

1. Smoothing the topography can reduce both SEFK and SESK. In particular, the slope parameter should not

be greater than 0.2 (Mellor et al., 1998). Greater values can artificially induce currents over 1 m/s.

2. Using the highest possible resolution can reduce the errors, since the pressure gradient error decreases with the square of the horizontal and vertical grid size.

3. Subtracting the horizontally averaged density before the computation of the baroclinic integral reduces the SESK.

4. Using a curvilinear grid that follows the bathymetry reduces the SESK.

This study used the first three techniques. The use of a curvilinear grid was not employed since the first three techniques successfully reduced the error to an acceptable level (to ~1 cm/s or less).

To show where the remaining velocity errors (induced by the pressure gradient force error) are present in the model domain, the velocity field for day 60 at sigma level 1 (surface) is shown in Figure 12. Maximum velocities of up to ~1 cm/s are found along the coast where the slope parameter is the greatest. These results are similar to those obtained by Martinho (2001) and indicate that with the use of the three error reduction techniques, the pressure gradient force error has been considerably reduced from values over ~1 m/s to values less than 1 cm/s.

E. WIND FORCING OVER TOPOGRAPHY

Experiment 5 (see Table 1) mimics Experiment 1, except instead of a flat bottom, topography was added with the same model forcing mechanisms. The model was initialized with horizontally averaged annual climatological temperature and salinity. The same coastline and annual climatological wind field were used. The results of Experiment 5 were run to isolate the effects of topographic beta and demonstrate its role in a wind-forced model.

By day 20 (Figure 13a), an equatorward current has developed with a maximum speed of ~40 cm/s. Weak, localized coastal upwelling is evident near promontories north of Perth. The upwelling is not as extensive or widespread as in the flat-bottom case (Experiment 1). A typical cross-section (Figure 13b) shows that the core of the surface current is situated above the shelf break instead of being directly at the coast. The undercurrent has a speed of ~2 cm/s and has deepened to greater than 1500 m depth.

Most obvious at day 40 (Figure 13c) is the intensification of upwelling south of Shark Bay and at ~29°S. Although it remains very localized, relatively cold water of 16.5°C has been upwelled to the surface. The main factor in increasing the upwelling is the strengthening of the equatorward surface current to ~80 cm/s. Although the current is present along the entire western and southern coast of Australia it is strongest in the northern end of the model domain, as expected due to the stronger winds in this region. As the surface current increases, the core

becomes more developed but continues to be centered over the shelf break (Figure 13d).

By day 60 (Figure 13e), the southerly winds have continued to enhance the equatorward surface current, which has reached a maximum velocity of ~120 cm/s. The areas of localized upwelling, off Shark Bay and at 29°S, have become relatively intense bringing ~14°C water to the surface. Temperature cross-sections for the same latitudes, (Figure 13h and 13i), respectively, show that the wide shelf to the north enhances the upwelling.

In addition to being much colder than the water offshore, the surface elevation in the upwelling regions is also lower. The alongshore pressure gradient induces an equatorward, geostrophic current which helps to enhance the wind-forced equatorward surface current. A relatively deep, poleward undercurrent of ~10 cm/s is trapped by the topography at ~1000 m depth from 26°S (Figure 13f) south to Cape Leeuwin (Figure 13g), where it becomes extremely narrow.

Based on these results, the addition of topography traps and enhances the equatorward surface current. Simultaneously, the topography hinders the development of some upwelling regions (e.g., coastal embayments) even with upwelling favorable winds; however, in areas where upwelling is present (e.g., off capes) the upwelling is very intense. The results of this experiment are representative of typical EBC regions other than the LCS.

F. THERMOHALINE GRADIENT FORCING OVER TOPOGRAPHY

Experiment 6 (see Table 1) is initialized with full annual climatology, but without wind forcing. It uses the same coastline and is run with realistic topography. It introduces conditions unique to the LCS.

By day 20 (Figure 14a), a poleward coastal current has developed with a maximum velocity of ~90 cm/s. The current extends from the northern edge of the domain around the southwest corner of Australia to the eastern edge. There is also a relatively broad movement of warm, offshore water to the south, with temperatures off Cape Leeuwin reaching 23°C. A typical cross-section (Figure 14b) shows that the surface current is centered over the shelf break and lies inshore of an equatorward current which intensifies with depth.

By day 40 (Figure 14c), the coastal current velocity has increased to ~140 cm/s. Warm, subtropical water of 25°C has been advected around Cape Leeuwin and into the entrance of the Great Australian Bight to the east of the model domain. Eddies have started to spin up off the coast near Cape Leeuwin and are subsequently advected eastward. An eddy dipole pair has formed off Perth. The cold core half of the dipole has been created by entraining cold water. A typical cross-section through a warm core eddy is shown in Figure 14d. Also showing is the undercurrent, which maintains its core velocity of ~20 cm/s at ~700 m depth along the slope below the poleward surface flow.

Despite the formation of many eddies, by day 60 (Figure 14e), the Leeuwin Current remains strong and continues to advect warm water south around Cape Leeuwin. The current remains trapped by the topography and is centered above the shelf break (e.g., see Figure 14f). The vertical velocity shear caused by the strong, poleward surface current and equatorward undercurrent create large meanders in the surface current, particularly in the north near Shark Bay. As the current travels around Cape Leeuwin, it continues to meander and create numerous eddies and dipole pairs, which are then advected eastward. One dipole pair, centered at ~35°S, 112°E, has separated from the Leeuwin Current and is no longer under the influence of topography. This pair will propagate westward due to the ß effect. As eddies form, their surface features deepen in time and subsequently merge with subsurface features (e.g., see Figure 14f).

Based on these results, the addition of bottom topography in this experiment isolates and traps the unique thermohaline gradient driven, poleward current all along the coast. The topography aids the development of realistic eddies and dipole pairs, but makes the core of the undercurrent too deep. Overall, the results of this experiment resemble the distinct dynamic features that set the LCS apart from classical EBCs.

G. WIND AND THERMOHALINE GRADIENT FORCING OVER TOPOGRAPHY

The final experiment, Experiment 7 (see Table 1), includes all the forcing mechanisms and most closely resembles the LCS in the annual sense. The model was

initialized with full annual temperature and salinity climatology and with a realistic bottom topography and coastline. In addition it was forced with the averaged annual wind field.

By day 20 (Figure 15a), a narrow poleward current has formed with a maximum speed of ~90 cm/s. This strong surface current is present all along the shelf break and advects warm subtropical water south, with temperatures off Cape Leeuwin reaching 23°C. A cross-section at Cape Leeuwin (Figure 15b) shows the core of the current located over the shelf break with an equatorward undercurrent of ~15 cm/s centered near 700 m depth. In regions where the continental shelf is wider, such as near Shark Bay, the main surface current is formed as far as 50-60 km offshore. This allows the wind forcing to dominate the flow inshore of the main current, generating an equatorward surface current directly at the coast. A cross-section in such a region (Figure 15c) shows a poleward surface flow offshore above the shelf break, with an equatorward surface flow inshore over the shallow continental shelf.

By day 40 (Figure 15d), the poleward surface current has velocity to speeds of ~120 cm/s and has advected relatively warm 24°C water south around Cape Leeuwin. As the surface velocity has increased, the meandering of the current also increases due to the baroclinic instability generated by the increasing the vertical velocity shear. Eddies are generated off Cape Leeuwin and subsequently propagate eastward along the southern coast. The equatorward wind forcing pushes the cold subpolar waters

northward, which get entrained by the current and help to develop eddy dipole pairs.

By day 60 (Figure 15e), the strength of the current is maintained, while it continues to advect warm, fresh water south. Figure 15f shows a surface plot of salinity, demonstrating the advection of fresh water by the surface current along the western coast. Many more meanders and eddies have formed in the current off the west coast. The addition of wind forcing, which opposes the poleward thermohaline induced current, helps to generate more well defined eddies. Two typical cross-sections at 34.3°S (Figure 15g) and 28°S (Figure 15h) show that, inshore of the warm core eddy, the surface current hugs the shelf break all along the coast. At 28°S, note that the wind forcing has also created an equatorward surface current, with a velocity of ~20 cm/s, inshore of the surface poleward current. This equatorward flow subsequently leads to localized areas of upwelling distinguished by slightly cooler waters along the coast, as seen by the rising of the temperature contours (e.g., Figure 15i) and increasing salinity (e.g.,Figure 15f) over the shelf.

The results of this final experiment show relatively realistic features of the LCS including a poleward surface current, equatorward undercurrent, meanders and eddies, as well as regions of localized upwelling. Unlike classical EBCs that are driven by wind forcing, the LCS is dominated by the effects of thermohaline gradients, which generate a poleward (equatorward) surface current (undercurrent) off the west coast. The thermohaline gradient and bottom topography trap the warm poleward flow along the coast,

despite the opposing wind forcing. The wind forcing influences the development of better defined eddies, and generates equatorward flow next to the coast in regions where the poleward surface flow is farther offshore.

H. DISCUSSION

Since Experiment 7 includes all the forcing mechanisms of the LCS, it is useful to qualitatively compare the final results of the model simulation with observational data to determine if the model developed a current system representative of the LCS. Because the study is not based on actual data but instead is a process-oriented study, direct comparisons to observational data cannot be made; however the dynamics of the model can be investigated to determine if there are qualitatively similar to observations of the LCS.

The results from Experiment 7, day 60 (Figure 15e), will be used in the comparison. The general features of the Leeuwin Current apparent in the satellite images (Figures 16 through 18) are similar to the results found in the final model experiment. The strong thermohaline gradient creates an onshore geostrophic flow, which then forms a narrow poleward current advecting warm subtropical waters southward around Cape Leeuwin and into the Great Australian Bight. All three satellite images show evidence of meanders, jets and eddies with varying length scales which are consistent with the model results. Studies have shown that the LCS has large spatial variations due to intensification of instabilities (Batteen and Butler, 1998; Cresswell, 1981; and Pearce and Giffiths, 1991). Current

velocity speeds of ~120 cm/s at day 60 of Experiment 7, agree with surface current measurements greater than 100 cm/s made by the R/V *Franklin* at Cape Leeuwin (Cresswell and Peterson, 1993). Overall the model results for this study are supported by their resemblence to both satellite images and previous studies of the LCS.

A final comparison of all the experiments is made to determine the role of each forcing mechanism in generating the LCS. For this comparison the last day of each experiment(excluding Experiment 4, the pressure gradient force error), i.e. day 60 (Figures 9e, 10e, 11e, 13e, 14e and 15e), will be analyzed. The obvious dominant forcing mechanism for the LCS is the thermohaline gradient which has a strong poleward component. The gradient sets up an onshore geostrophic flow, which when it approaches the coast, is forced poleward into a strong, narrow surface poleward current. The flow is steered down the coast and as it reaches Cape Leeuwin it forms meanders and eddies. In regions where the Leeuwin Current leaves the coast, the wind forcing can control the flow and create an equatorward flow, which is upwelling favorable. Since the wind opposes the main surface poleward current, the southerly wind generates considerable shear, which aids in the development of better defined eddies.

While wind and thermohaline forcing are the main driving mechanisms for the current, without topography, the results from the flat bottom experiments show broad currents, which do not accurately represent the LCS. In terms of current width, the topographic beta effect has greater influence, by trapping the current along the coast,

than the planetary beta effect, which broadens the current. In the flat bottom case, the current is steered by the coastline. When topography is added, the current is steered by the shelf break, frequently leaving the coast as it follows the 200m depth contour southward to Cape Leeuwin and eastward into the Great Australian Bight. A comparison of the wind only experiments shows that topography reduces the upwelling that was present along the entire coast in the flat-bottom experiment and enhances localized areas just north of Cape Leeuwin and of 30°S. When the current is not trapped along the coast, such as in the north near Shark Bay and just north of Cape Leeuwin, the wind forcing generates an equatorward current which consequently produces upwelling. The presence of upwelling in these areas is important to the biological productivity of the region, which is important to the fishing and tourism industries.

THIS PAGE INTENTIONALLY LEFT BLANK

IV. SUMMARY

The objective of this process-oriented study was to build on previous studies and to investigate the roles of wind forcing, thermohaline gradients, and bottom topography in the Leeuwin Current System. The results of several numerical experiments (see Table 1) using the POM, a bottom-following sigma coordinate model, was explored. The POM was chosen for this study because it has been widely used to simulate coastal processes associated with continental shelf flows and bottom boundary layer dynamics. In all experiments a beta-plane was used. Experiment 1 (Experiment 2) investigated the effect of annual wind forcing (full, annual climatology) over a flat bottom. Experiment 3 was run with both annual wind forcing and full, annual climatology over a flat bottom. The results of Experiment 4 were used to determine the pressure gradient force error created by the addition of bottom topography to the model. Experiment 5 (Experiment 6) investigated the role of annual wind forcing (full, annual climatology) over topography. The final experiment, Experiment 7, was run with full, annual climatology and wind forcing over topography.

In Experiment 1 the annual wind forcing, without a thermohaline gradient, forced a weak equatorward surface current. It also produced classical EBC features including upwelling, meanders, eddies and a poleward undercurrent. The upwelling was evident along the entire western coast of Australia, but was most intense near Shark Bay.

Experiment 2 removed the wind forcing but introduced the annual temperature and salinity gradients, over a flat bottom. The effects of the thermohaline gradient developed a strong, broad poleward surface current more characteristic of the LCS. Planetary beta effects created westward propagation of the current increasing its offshore extent. Warm, subtropical waters were advected southward around Cape Leeuwin. This experiment also generated meanders and eddies south of Perth, as well as an equatorward undercurrent.

The final flat bottom experiment, Experiment 3, combined the effects of annual wind forcing and the thermohaline gradient. The results resembled those of Experiment 2, showing that the thermohaline gradient is the dominating forcing mechanism in the LCS. The role of the wind was to slow the speed of the poleward current and enhance the generation of eddies. The wind also created localized upwelling regions along the coast where the poleward flow left the coastline. Finally, the wind forcing advected subpolar water northward, which frequently became entrained by current meanders and subsequently formed the cold core half of eddy dipoles.

Experiment 4 introduced topography but was run with no wind or thermohaline gradient forcing to determine the pressure gradient force error. It showed that the velocity errors inherent in a sigma coordinate model could be reduced from ~1 m/s to ~.01 m/s using three techniques. The techniques used were: 1) smoothing the topography, 2) using the highest possible resolution, particularly along the shelf break, and 3) subtracting the area-averaged

density before computation of the baroclinic integral. The results showed that the highest velocities induced by the pressure gradient force error were directly related to regions were the slope parameter was the largest, i.e. the shelf slope and coastline.

Experiment 5 explored the role of annual wind forcing, without annual climatology, over bottom topography. The topography had the effect of trapping the equatorward current along the coast, increasing its maximum velocity when compared to the flat bottom case (Experiment 1). Although the topography limited the extent of upwelling to regions north of 30°S, the intensity of the upwelling was increased. Relatively cool water of 14.5°C was upwelled near Shark Bay.

In Experiment 6, the thermohaline gradient forcing was isolated over bottom topography. Similar to Experiment 5, the addition of topography opposed the planetary beta effect and trapped the current along the coast creating a strong, narrow poleward current. The shelf break steered the current southward along the coast and around Cape Leeuwin into the Great Australian Bight region. The trapped coastal current had greater instabilities than in the flat bottom experiments resulting in more meanders, offshoots and eddies.

Experiment 7 provided the best representation of the LCS because it included annual wind, annual climatology, and bottom topography. In terms of location and velocity, it generated the most realistic equatorward surface current and poleward undercurrent. The results of this experiment show that, in an annual sense, the effects of thermohaline

gradients dominate and set the system apart from classical EBCs. The major role of the wind is to slow the poleward surface flow, enhance eddy spin-up and create localized upwelling regions. Bottom topography is shown to play an important role in intensifying and trapping currents near the coast, in weakening the subsurface current and in intensifying eddies off capes. Overall, Experiment 7, the most complete experiment of the study, compared well to observations and provided the most accurate representation of the LCS. Although, in the annual sense, the wind is an insignificant factor compared to the thermohaline gradient, it is the seasonality of the wind that determines when the Leeuwin Current flows. Further research using seasonal winds and seasonal thermohaline forcing is recommended due to the seasonal nature of the observed Leeuwin Current.

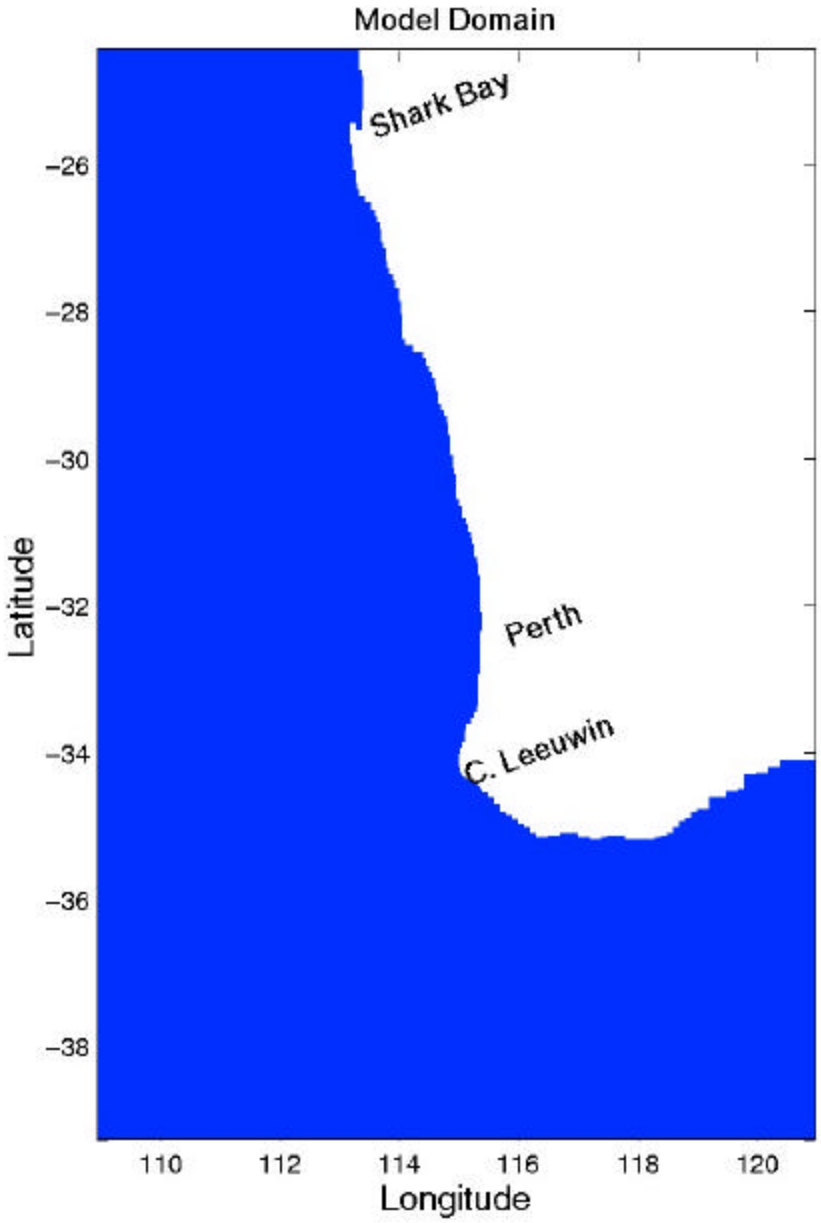

Figure 1. The model domain for the Leeuwin Current System (LCS) is bounded by 39°S to 24.5°S, 109°E to 121°E. The model domain has a closed boundary along the entire coast and four open boundaries.

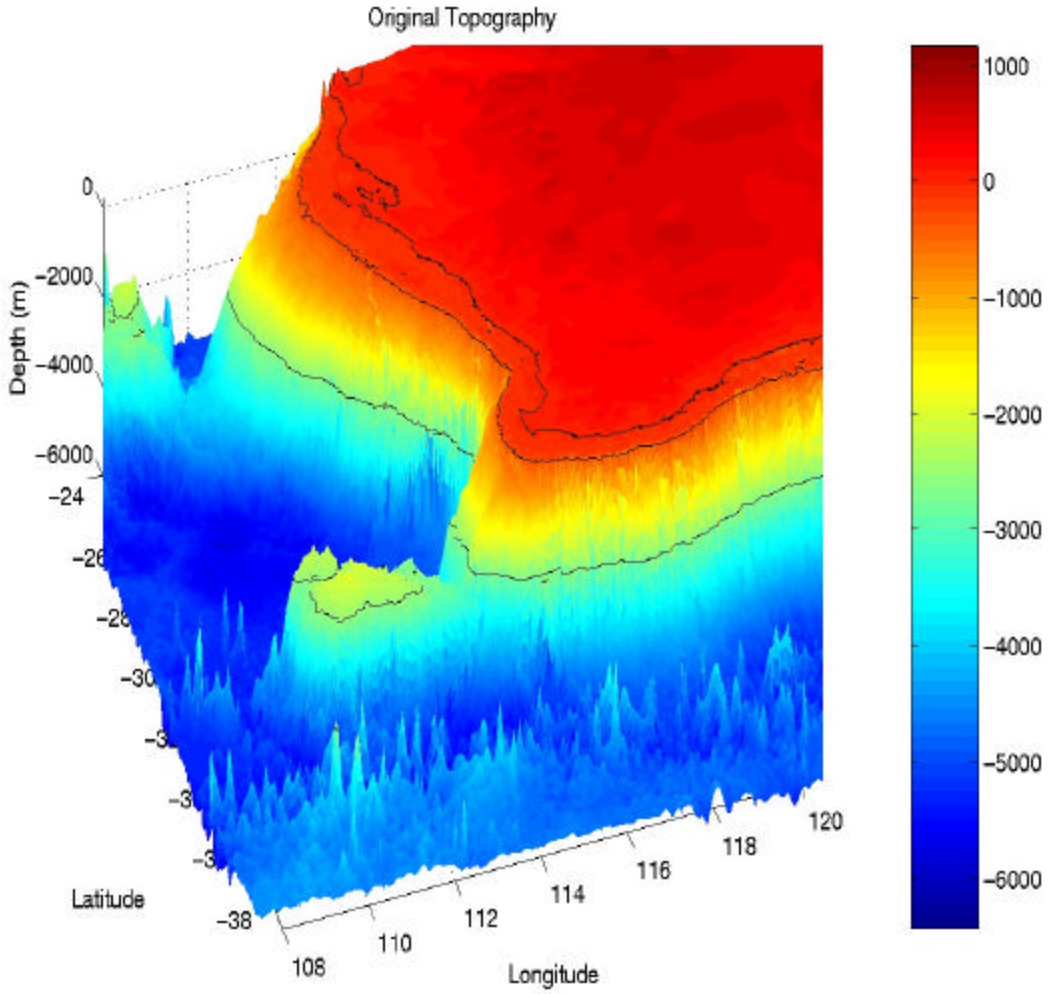

Figure 2a. Original topography (meters) in 3-D (from Sandwell and Smith, 1996) with a resolution of 2 minutes (1/30 degree). Contours depict the shoreline, 200m and 2500m isobaths.

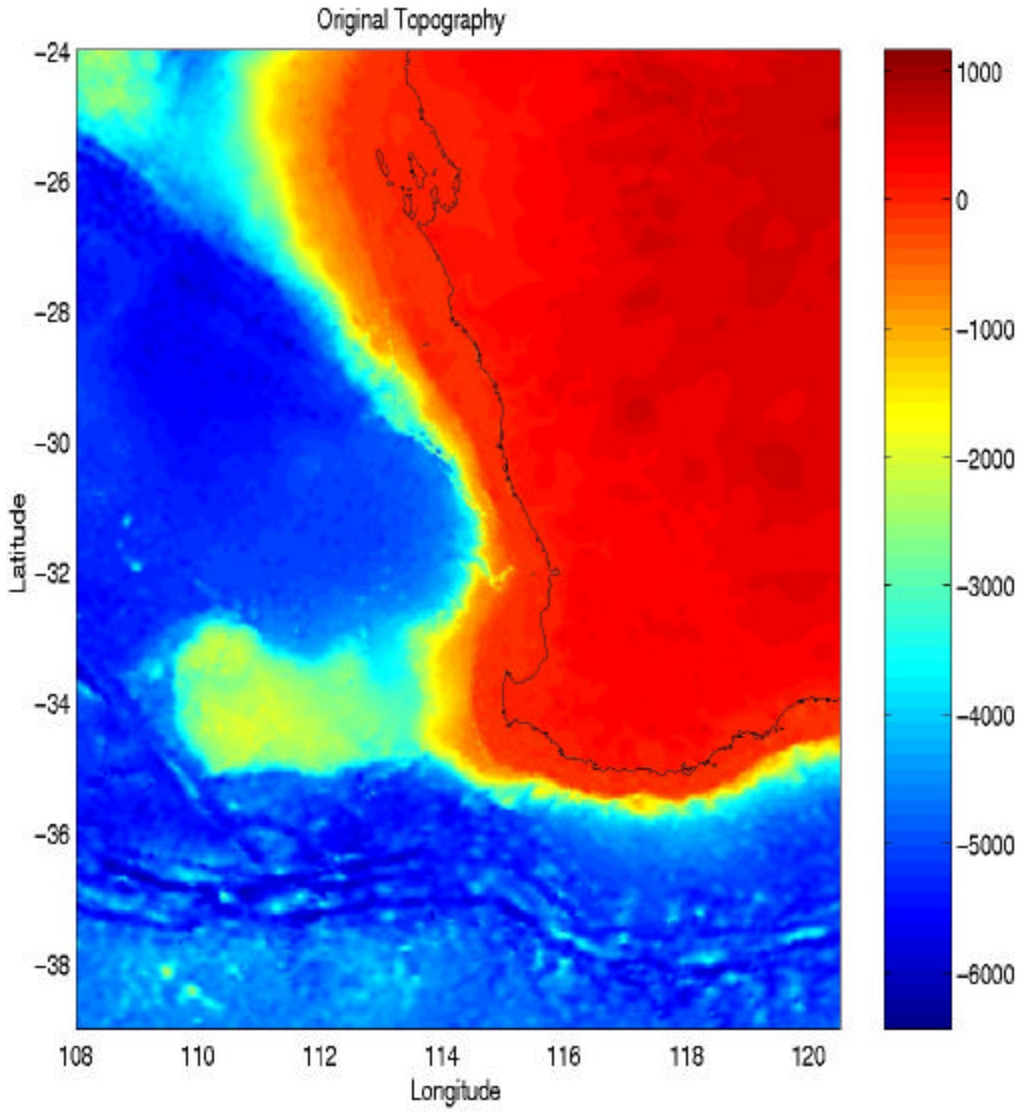

Figure 2b. Original topography (meters) in 2-D (from Sandwell and Smith, 1996) with a resolution of 2 minutes (1/30 degree).

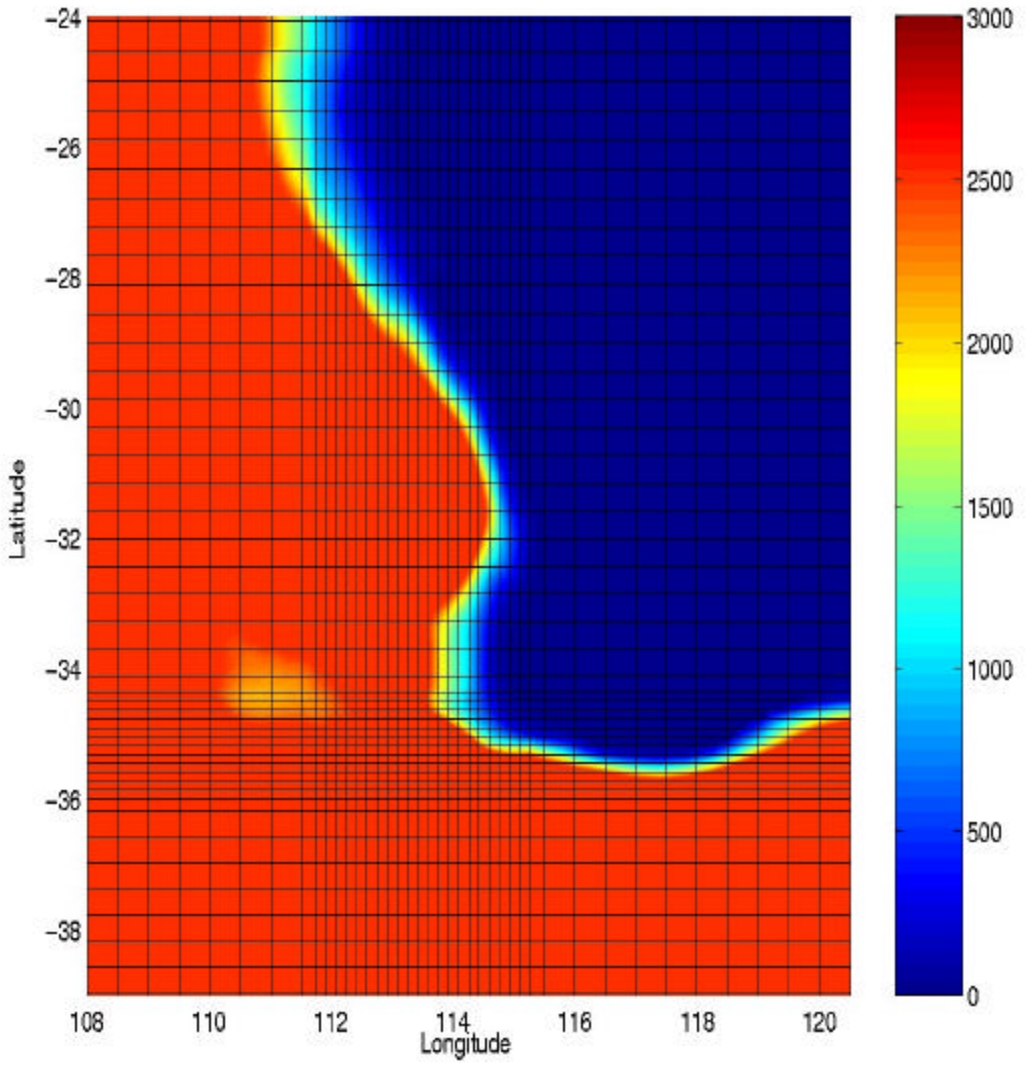

Figure 3. Resolution grid lines with every fifth grid line plotted. (10 by 10 km res. with two bands of 10 by 3 km and 3 by 10 km resolution).

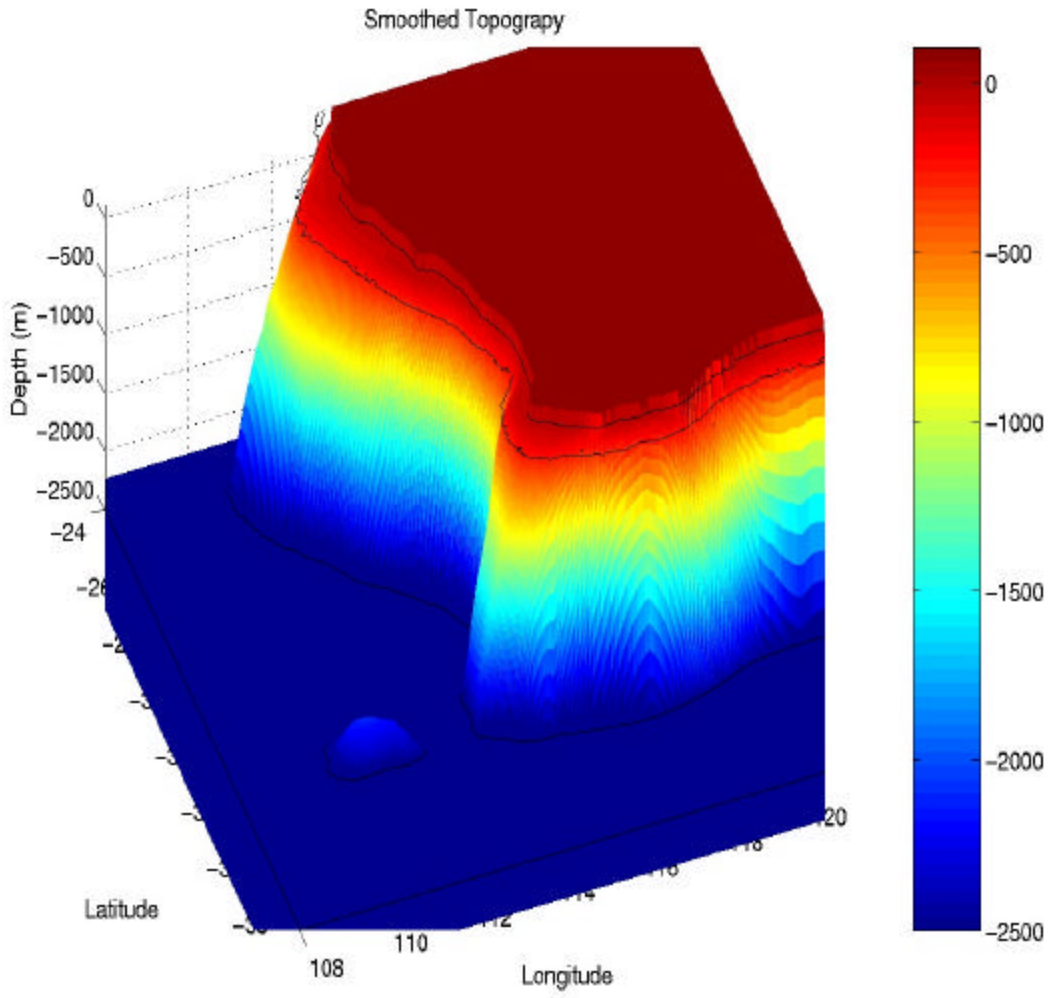

Figure 4a. Smoothed topography (meters) obtained after applying a two-dimensional Gaussian filter and reassigning depths greater than 2500 m to 2500 m. Contours depict the shoreline, 200 m and 2500 m isobaths.

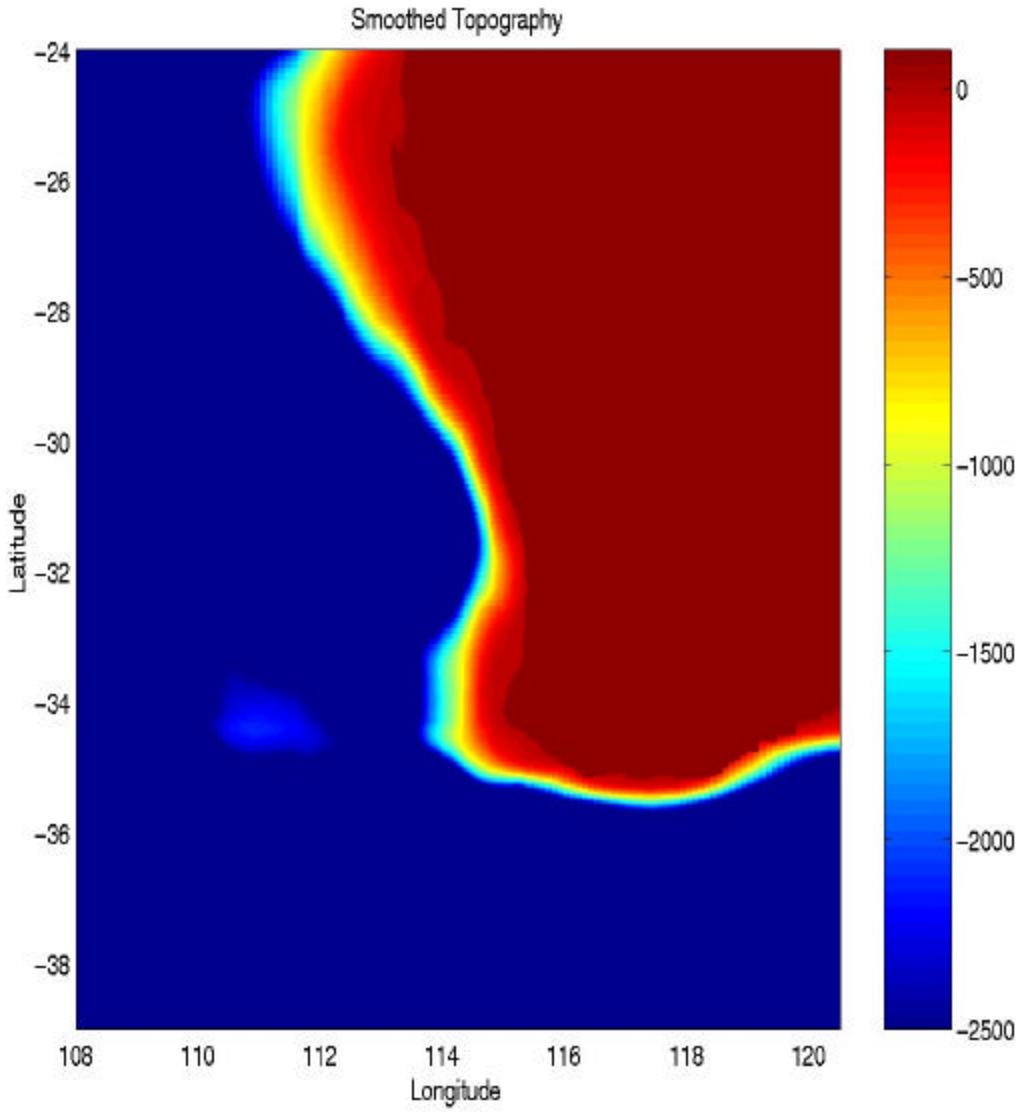

Figure 4b. Smoothed topography (meters) in 2-D obtained after applying a two-dimensional Gaussian filter and reassigning depths greater than 2500 m to 2500 m.

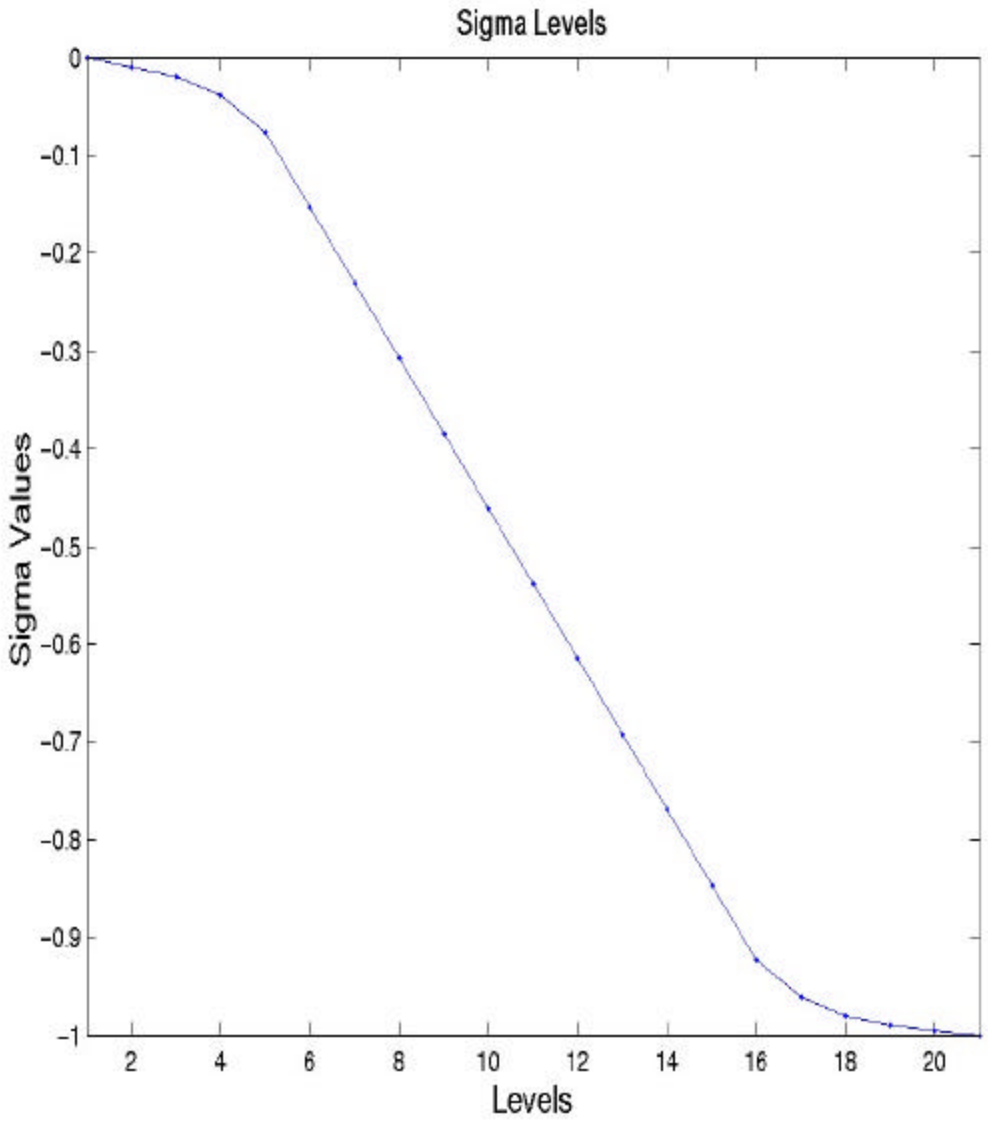

Figure 5. Plot of the 21 sigma levels.

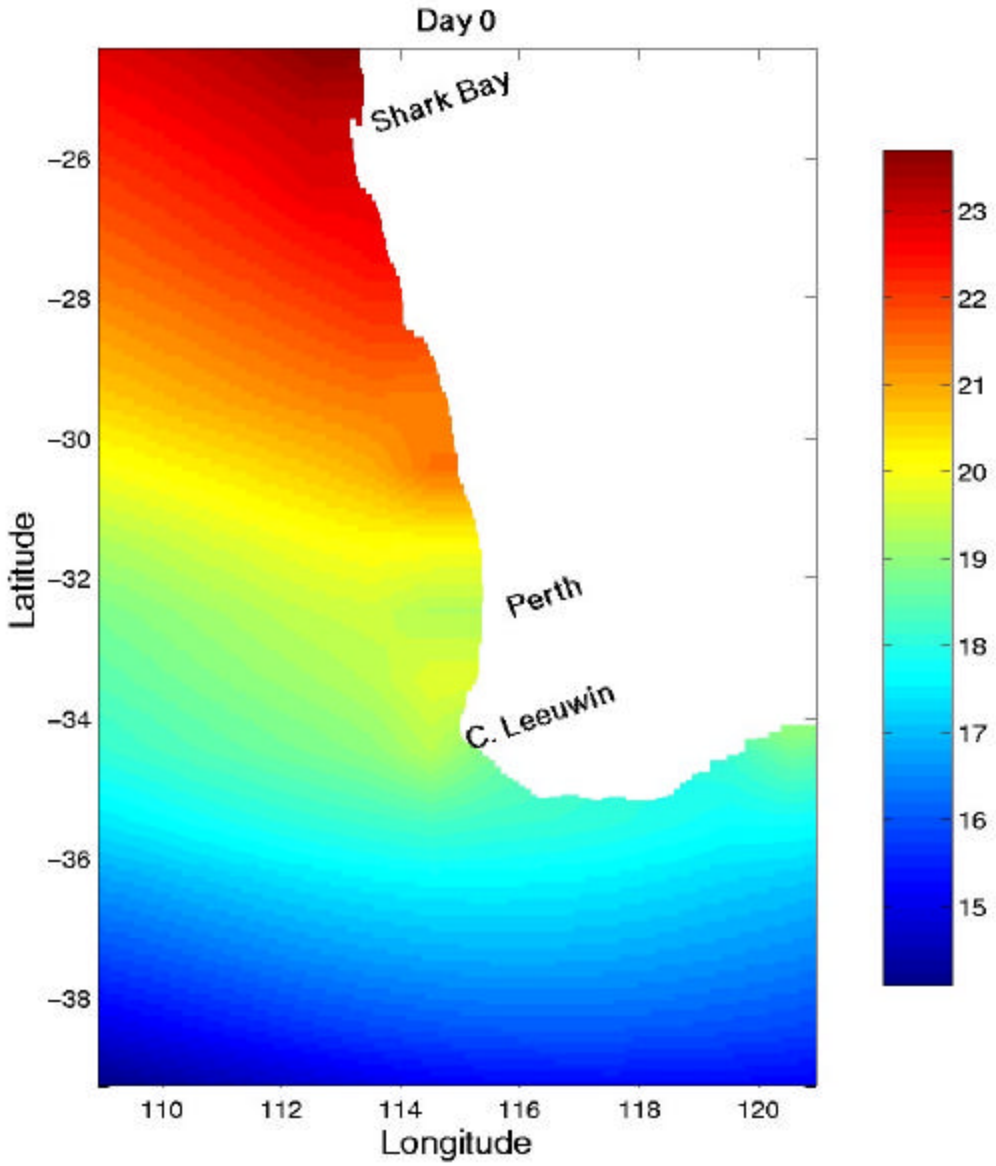

Figure 6. Annual climatological surface temperature (°C) obtained from Levitus and Boyer (1994).

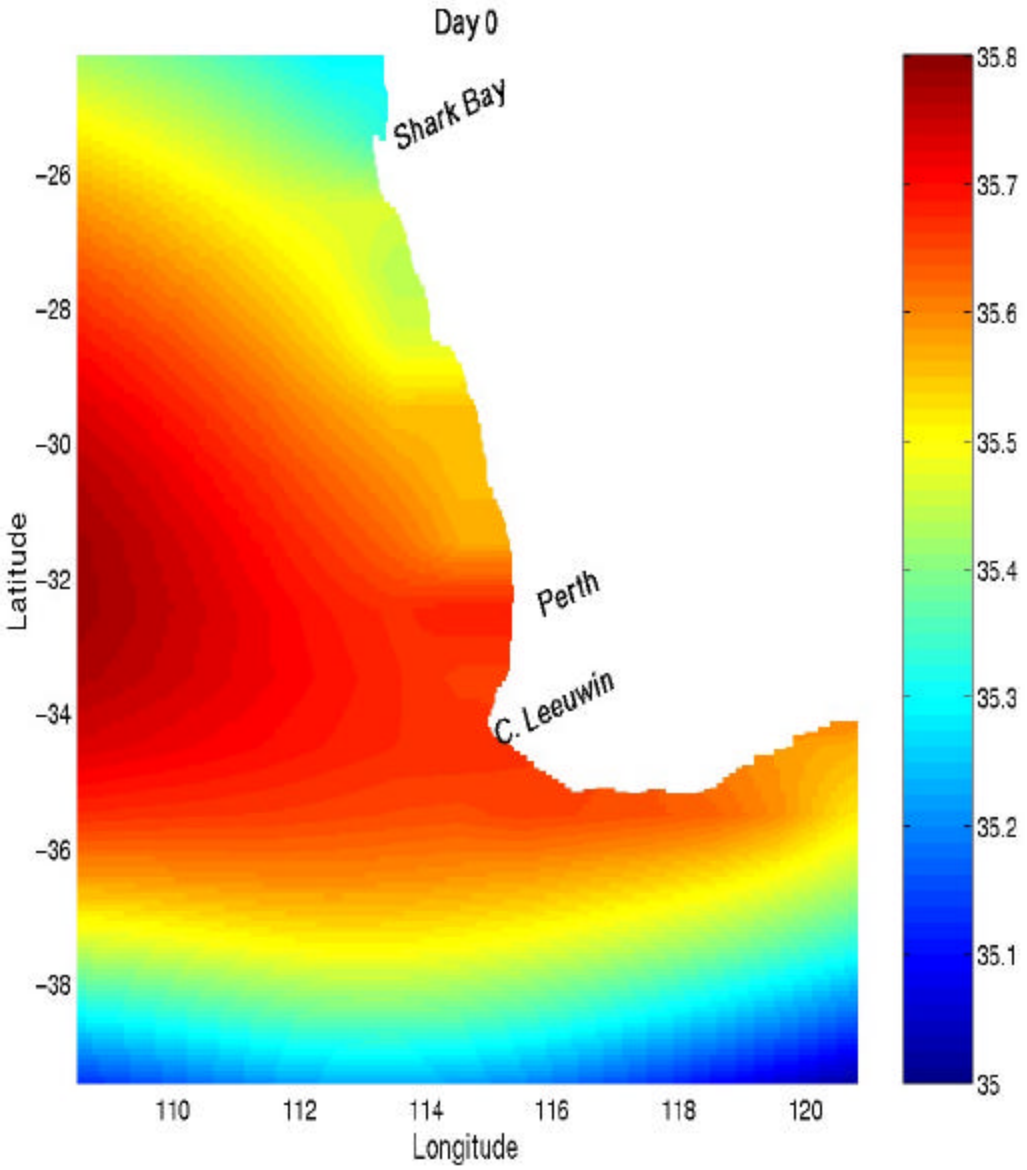

Figure 7. Annual climatological surface salinity from Levitus et al. (1994).

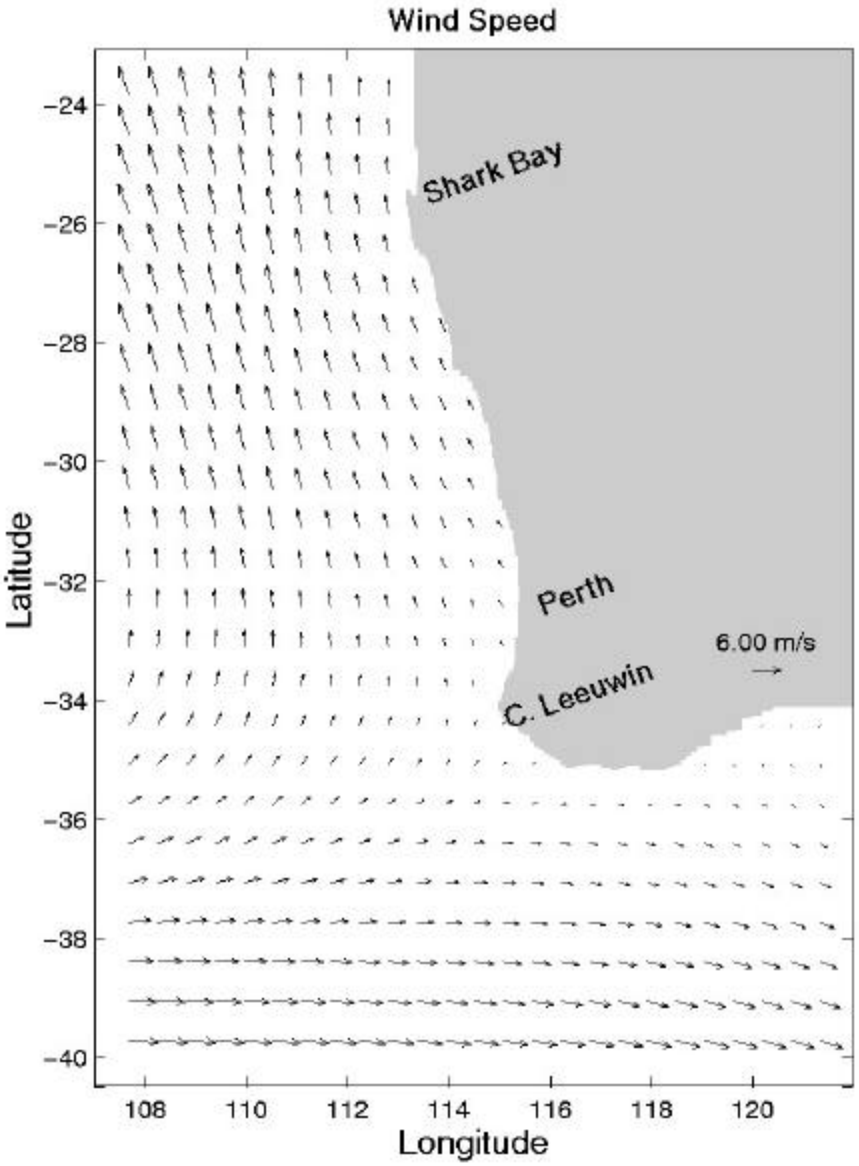

Figure 8. Annual average wind in m/s from climatological ECMWF winds obtained from Trenberth et al., 1990.

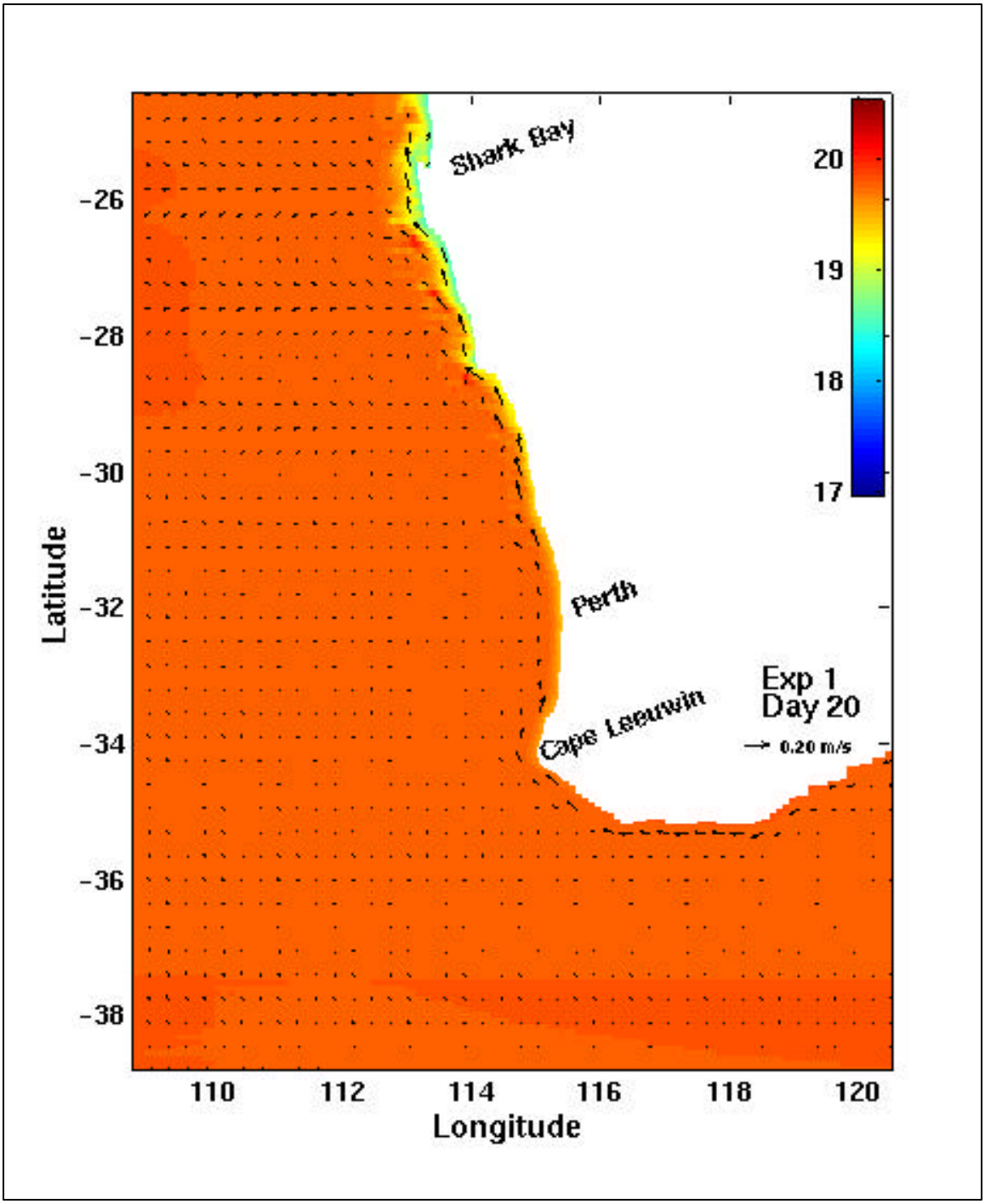

Figure 9a. Surface temperature (°C) and velocity vectors for Experiment 1 on day 20.

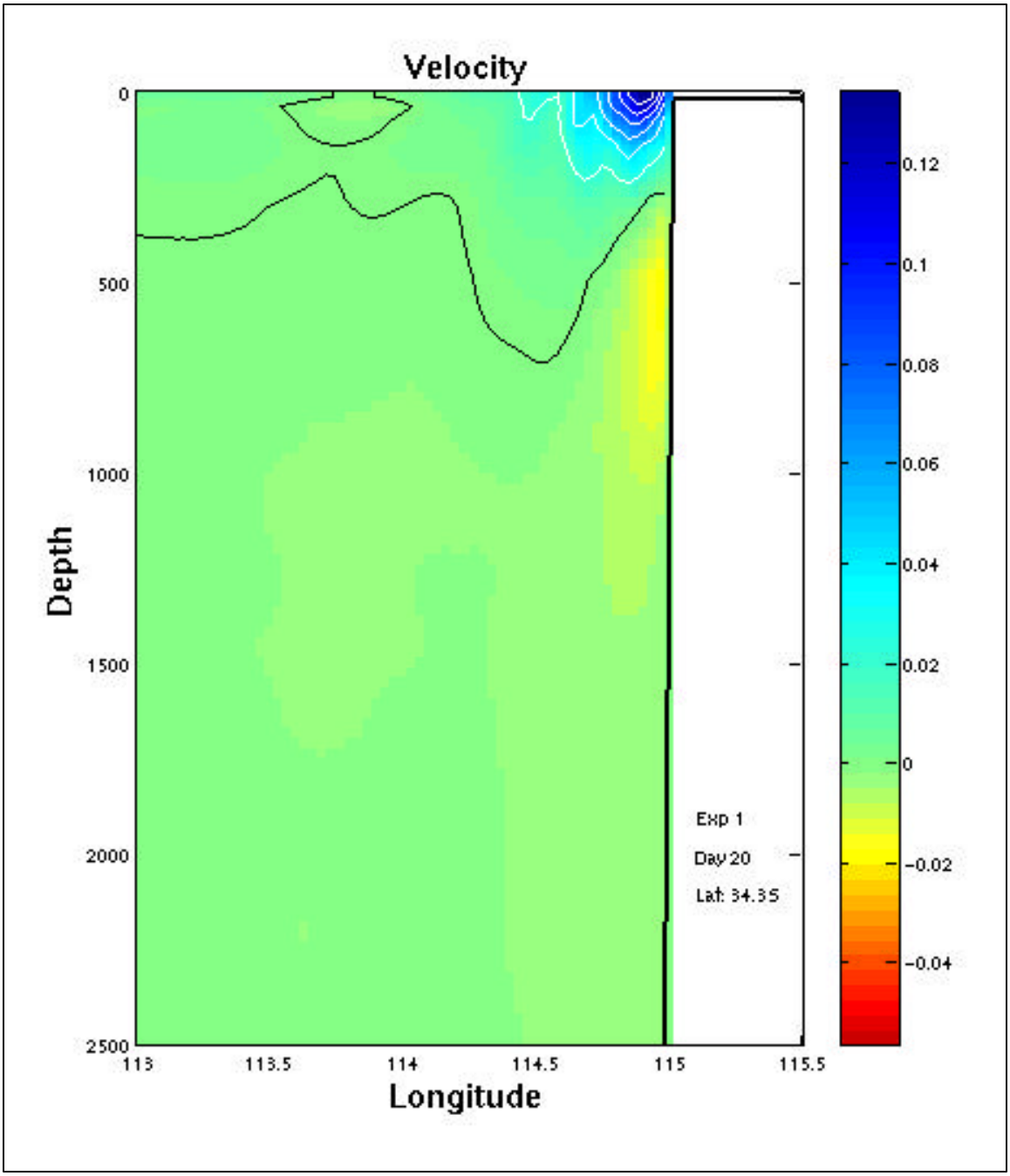

Figure 9b. Cross-section of north-south velocities (m/s) at Cape Leeuwin (34.3°S) for Experiment 1 day 20. Blue is equatorward (north).

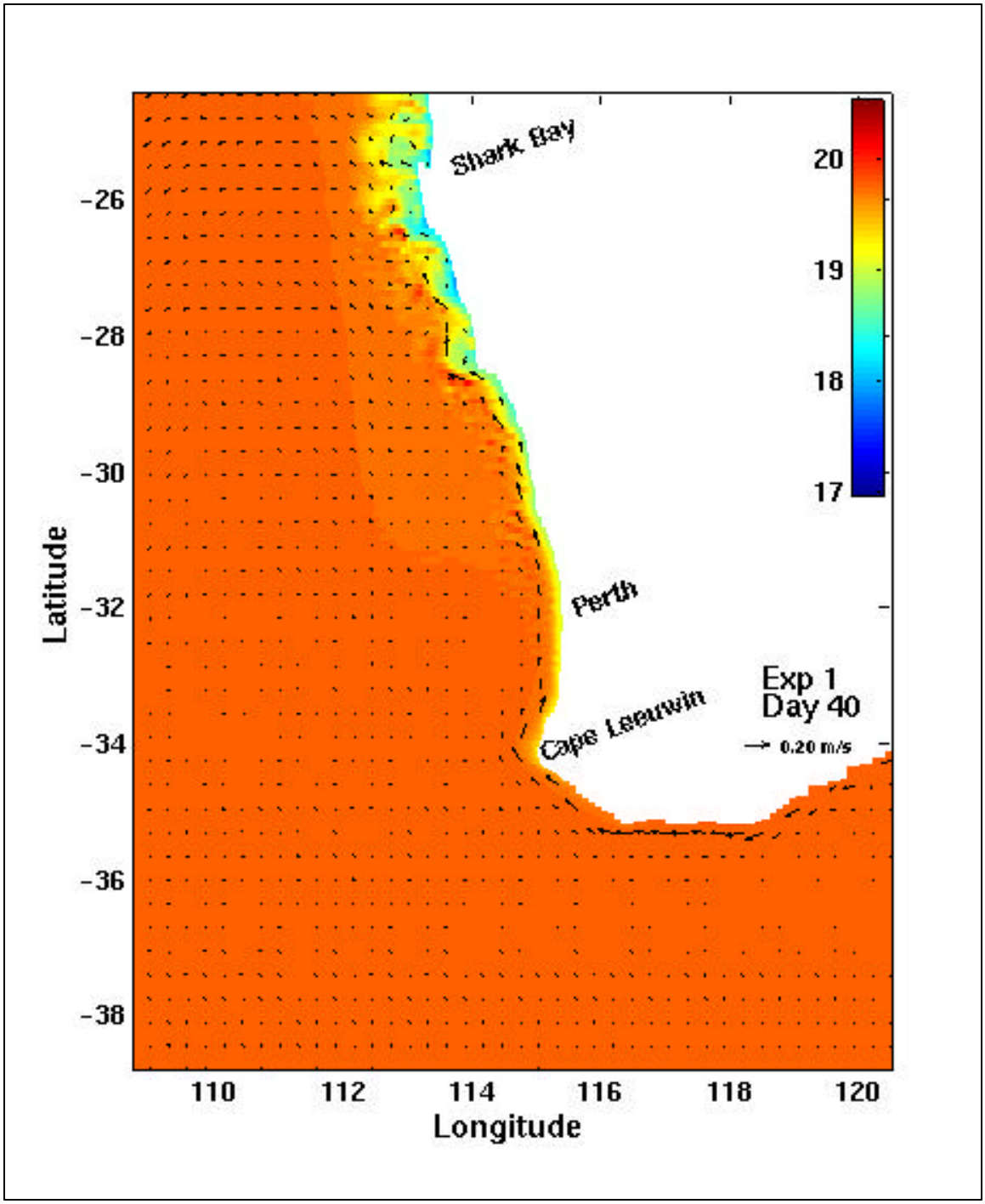

Figure 9c. Surface temperature (°C) and velocity vectors for Experiment 1 on day 40.

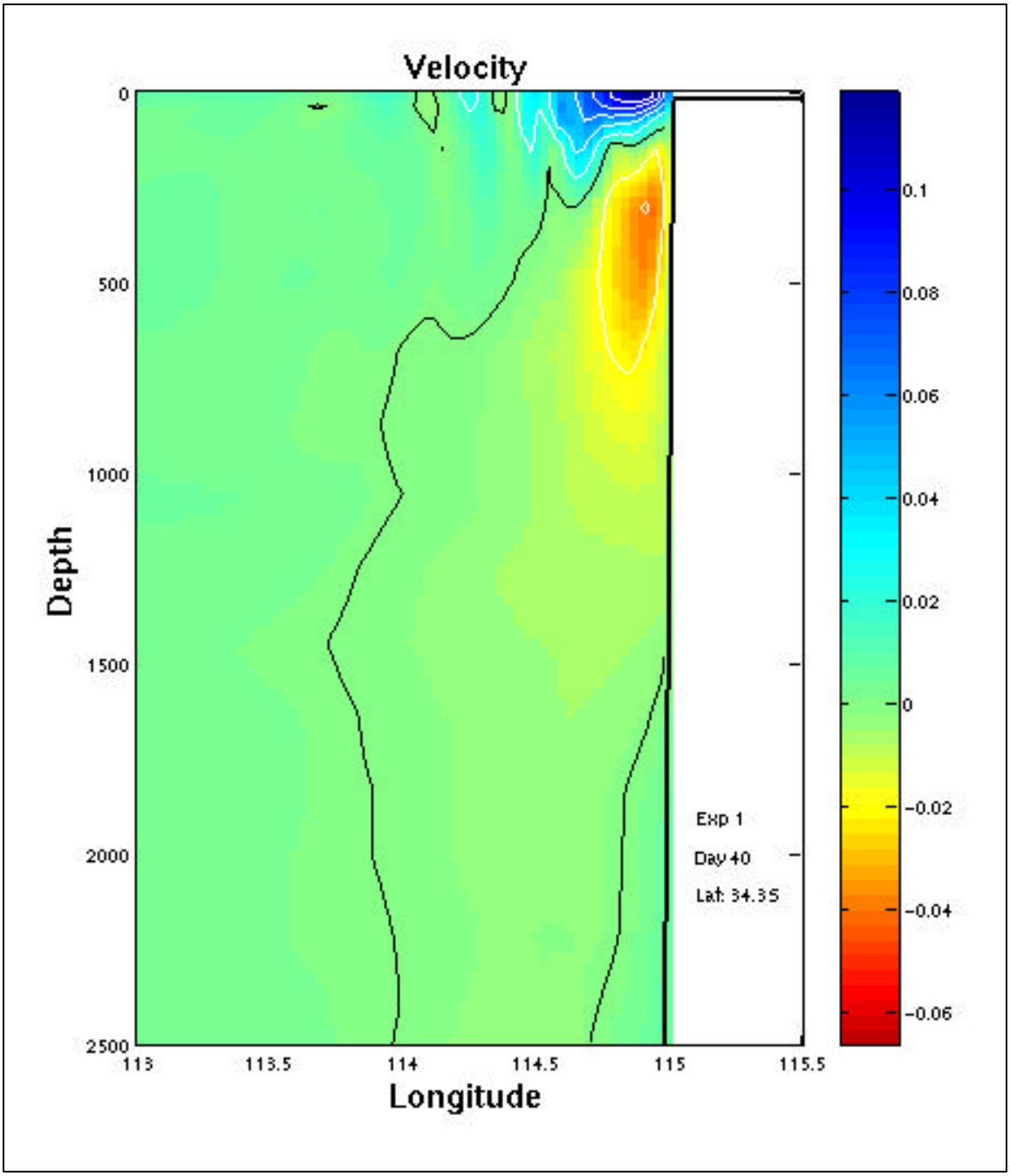

Figure 9d. Cross-section of north-south velocities (m/s) at Cape Leeuwin (34.3°S) for Experiment 1 day 40. Blue is equatorward (north).

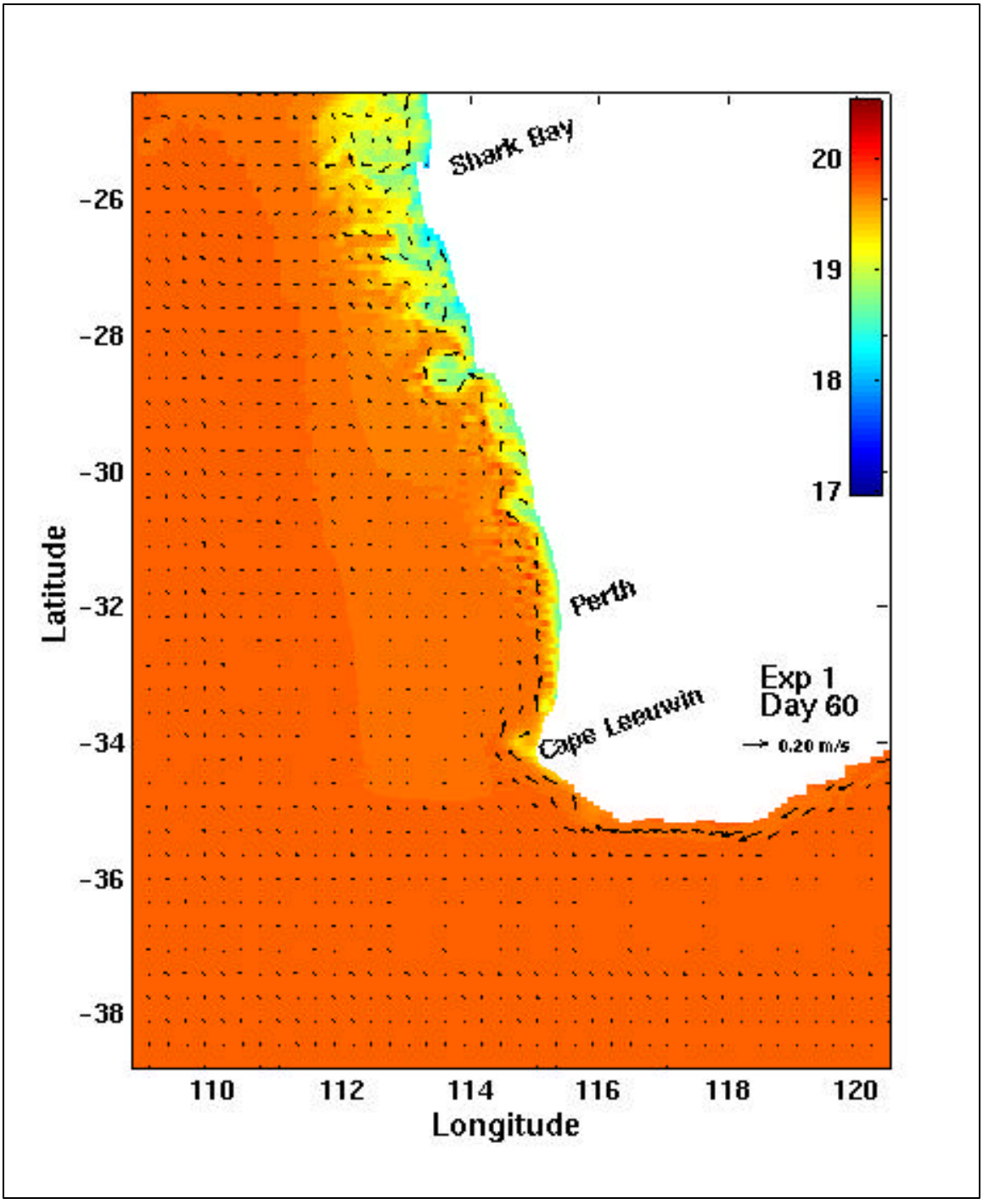

Figure 9e. Surface temperature (°C) and velocity vectors for Experiment 1 on day 60.

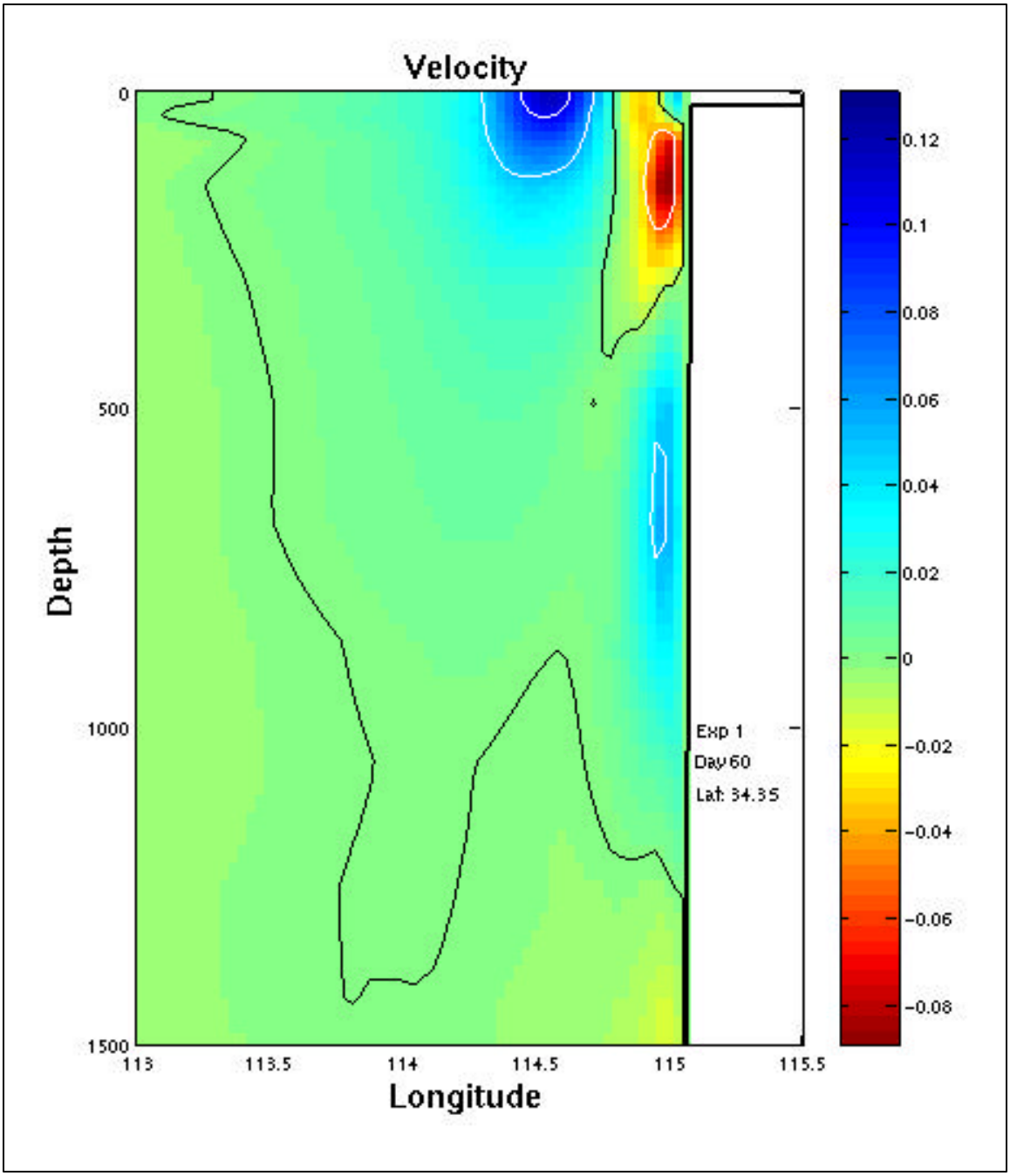

Figure 9f. Cross-section of north-south velocities (m/s) at Cape Leeuwin (34.3°S) for Experiment 1 day 60. Blue is equatorward (north).

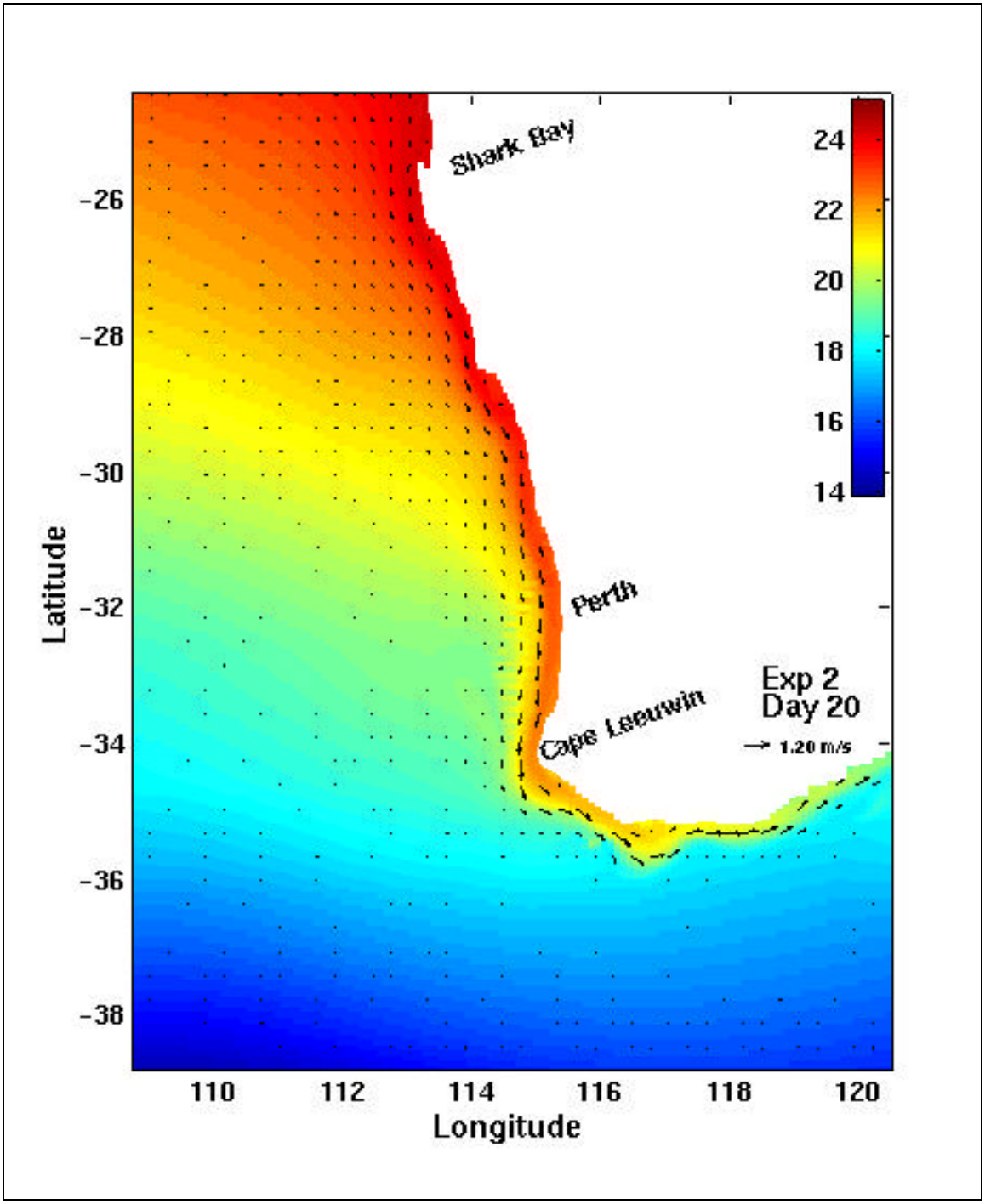

Figure 10a. Surface temperature (°C) and velocity vectors for Experiment 2 on day 20.

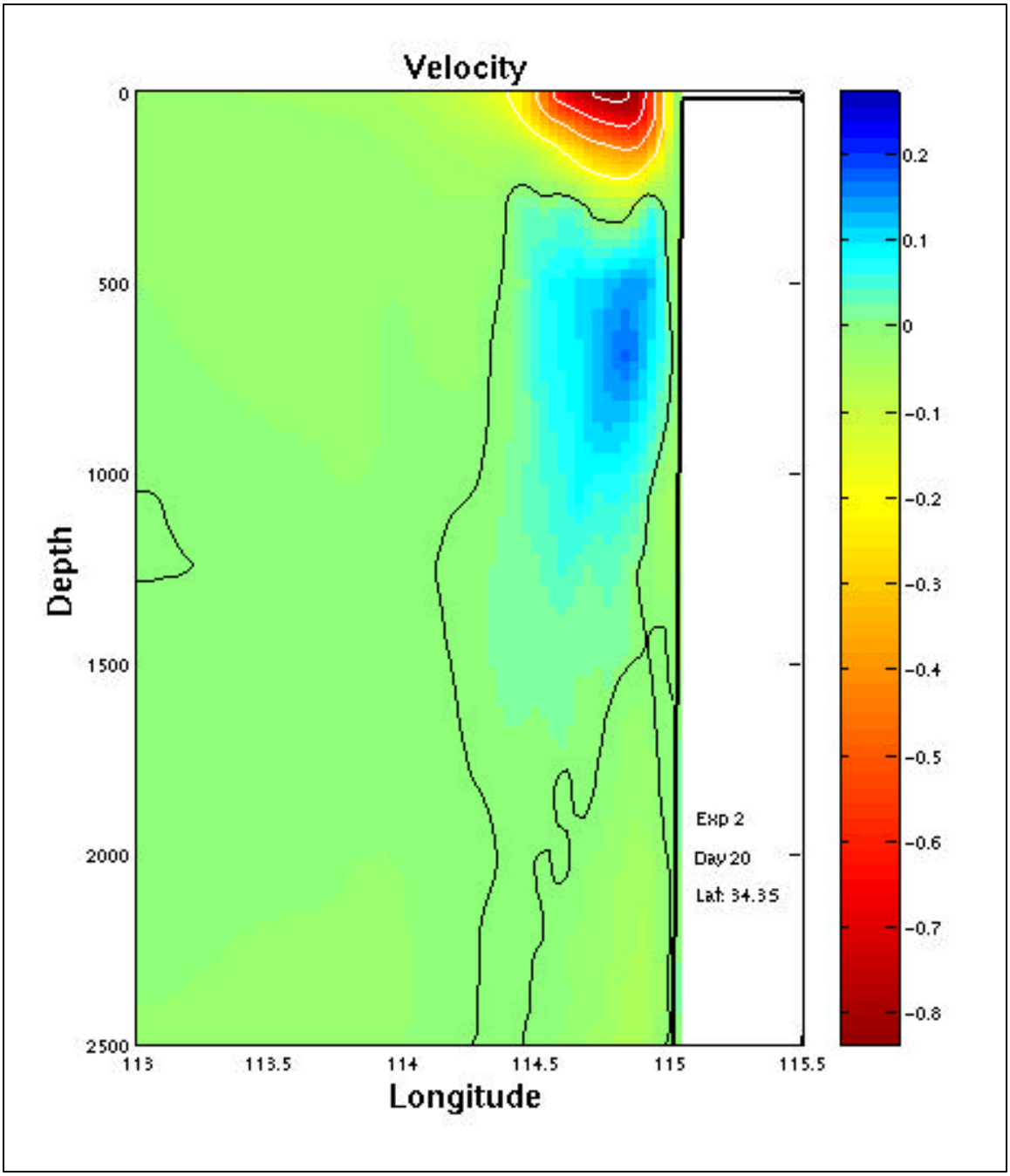

Figure 10b. Cross-section of north-south velocities (m/s) at Cape Leeuwin (34.3°S) for Experiment 2 day 20. Blue is equatorward (north).

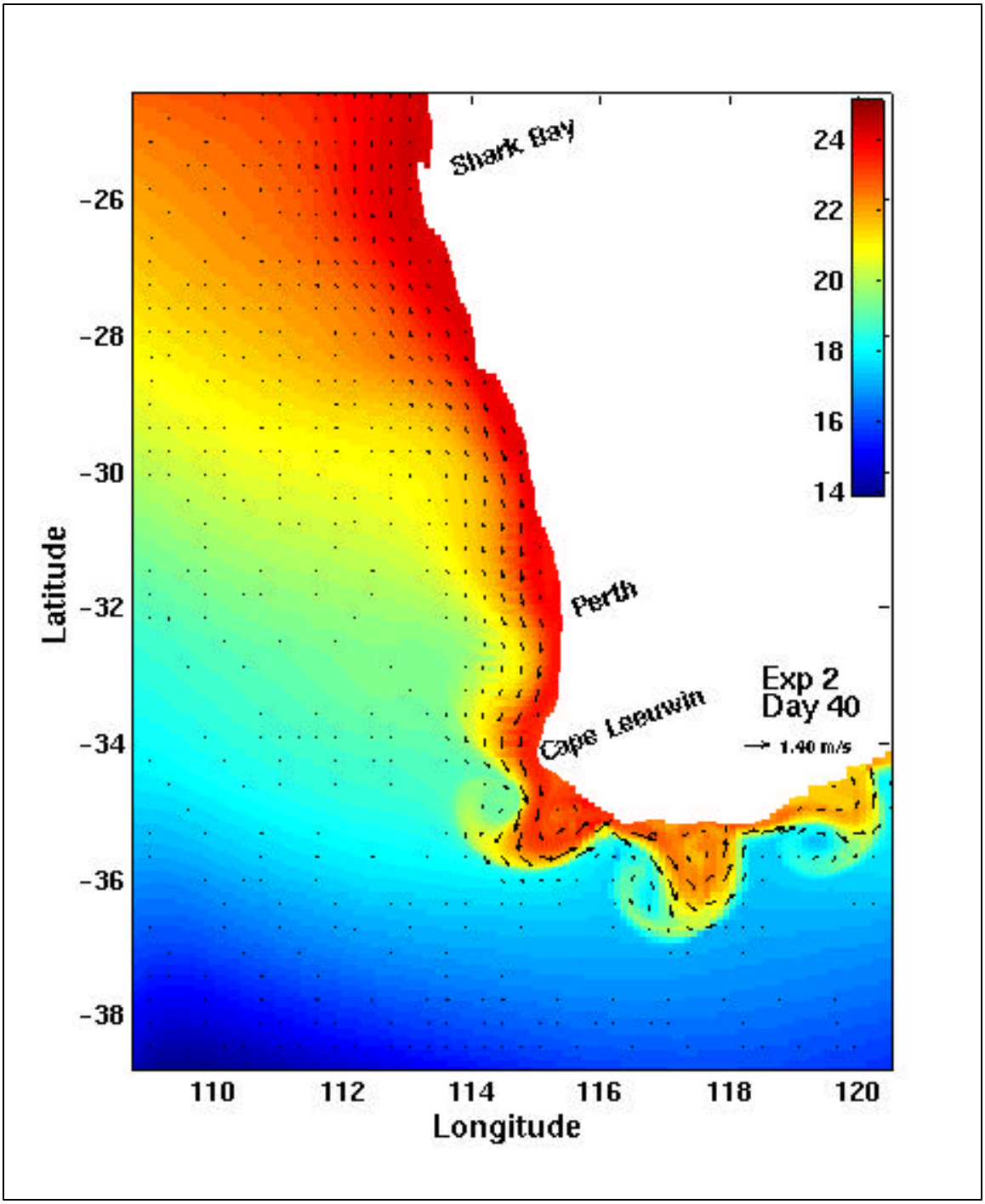

Figure 10c. Surface temperature (°C) and velocity vectors for Experiment 2 on day 40.

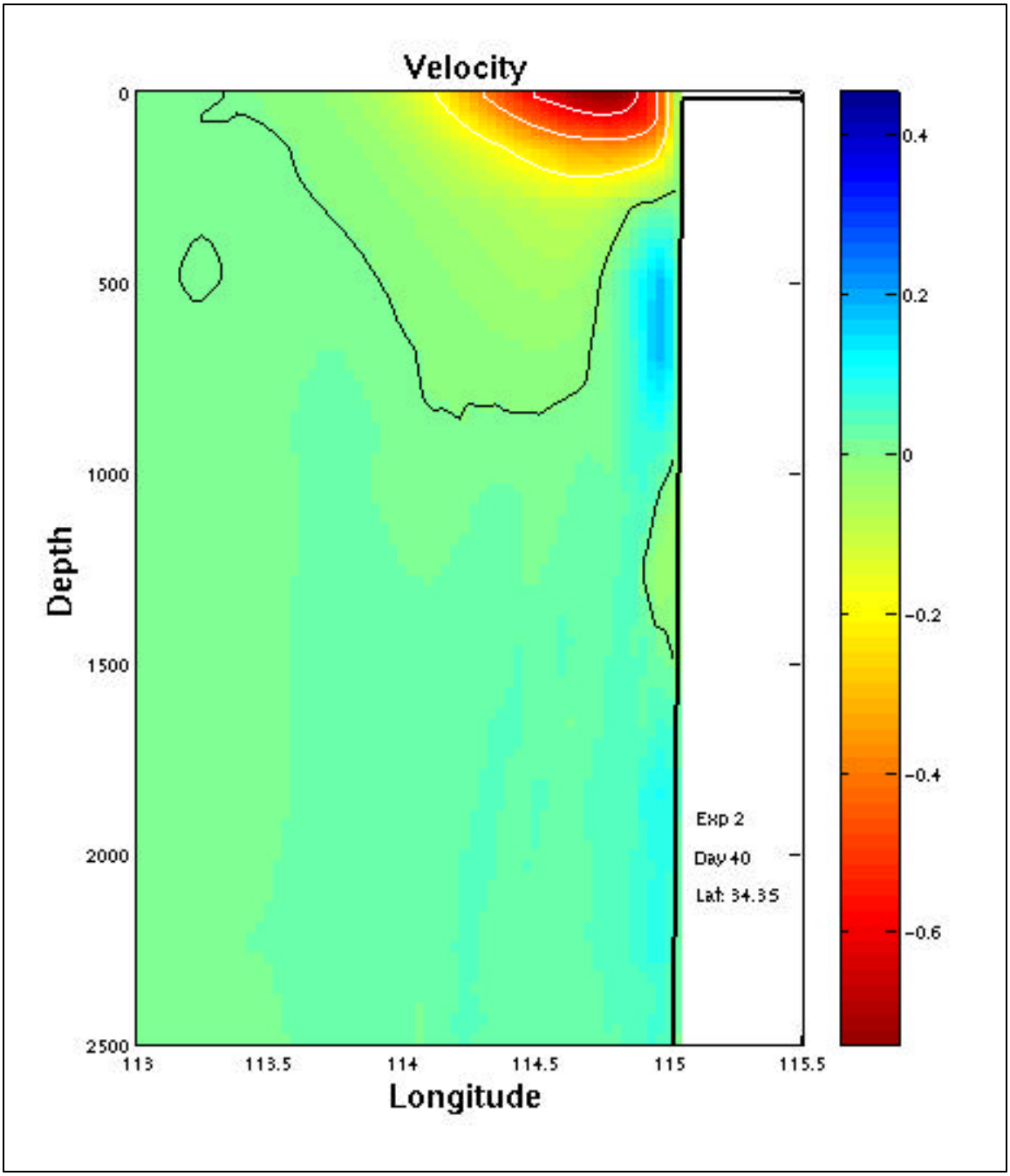

Figure 10d. Cross-section of north-south velocities (m/s) at Cape Leeuwin (34.3°S) for Experiment 2 day 40. Blue is equatorward (north).

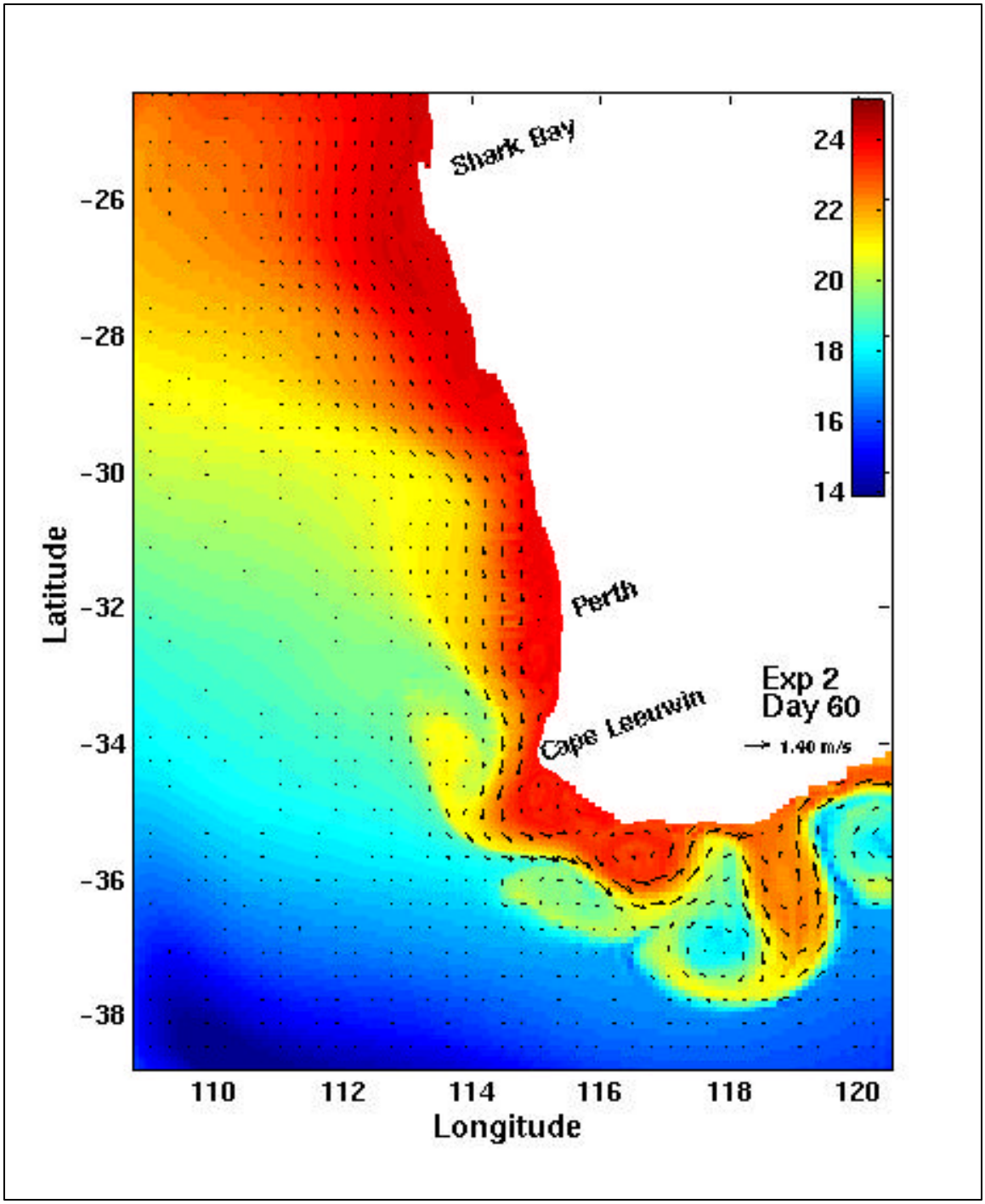

Figure 10e. Surface temperature (°C) and velocity vectors for Experiment 2 on day 60.

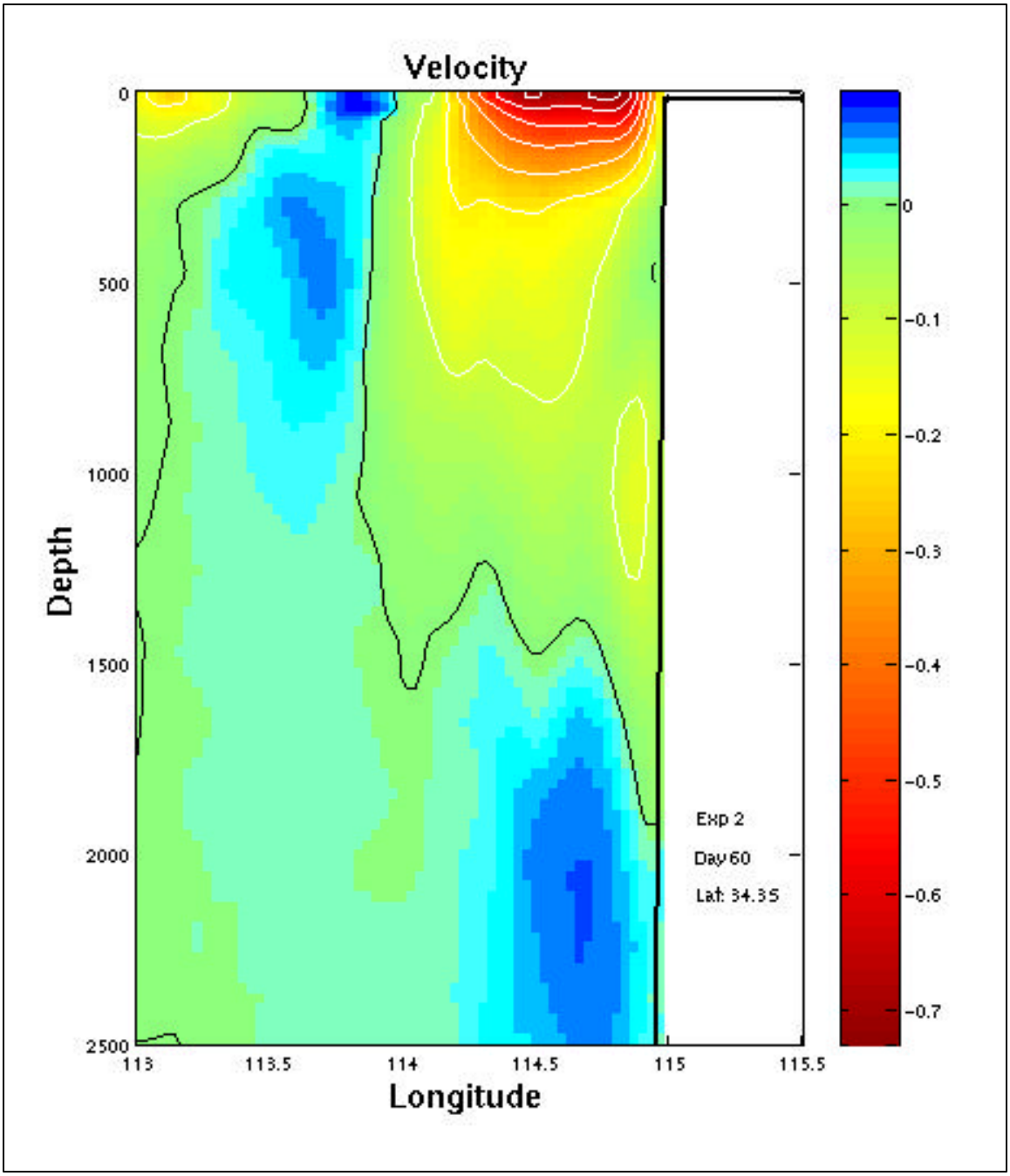

Figure 10f. Cross-section of north-south velocities (m/s) at Cape Leeuwin (34.3°S) for Experiment 2 day 60. Blue is equatorward (north).

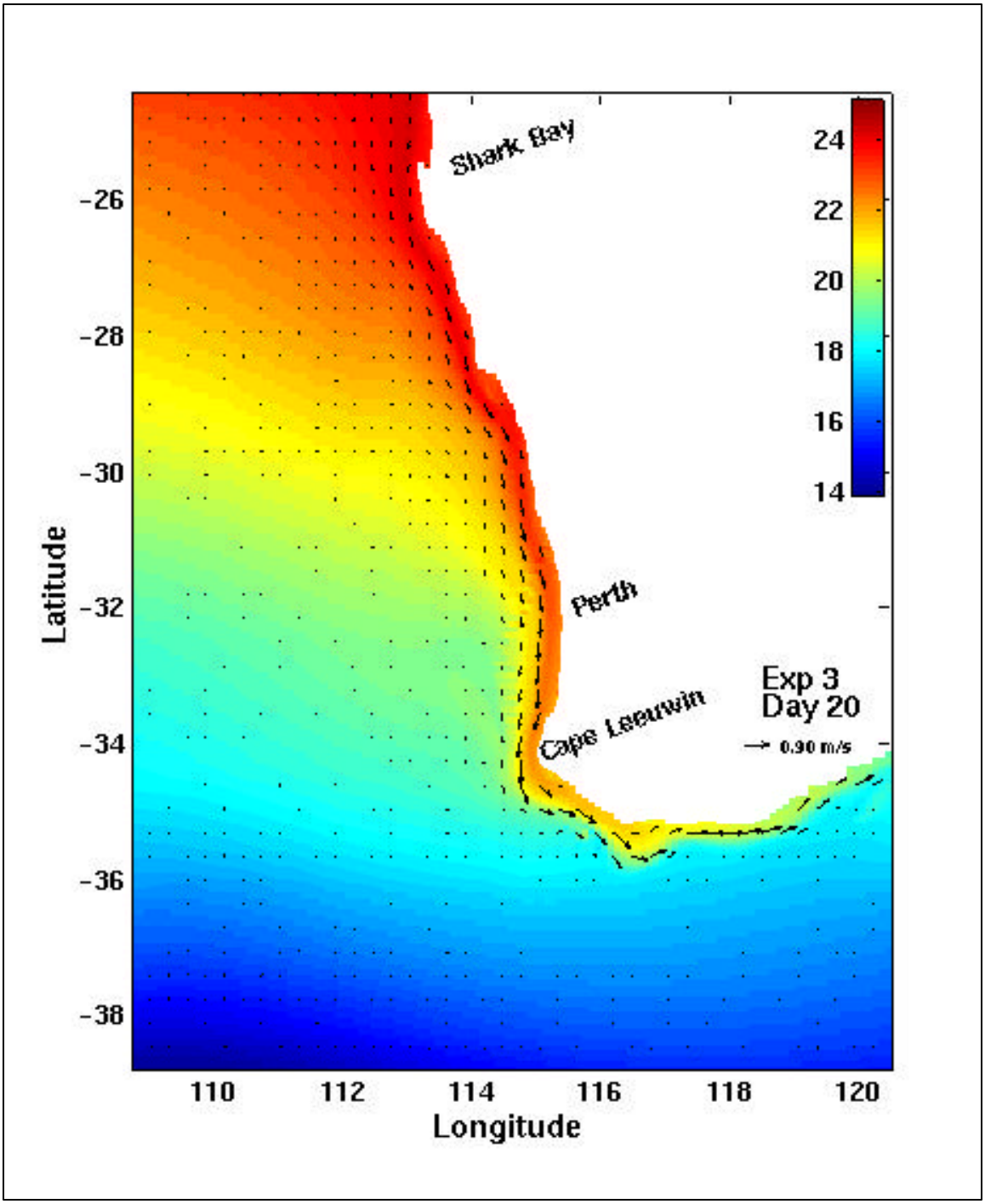

Figure 11a. Surface temperature (°C) and velocity vectors for Experiment 3 on day 20.

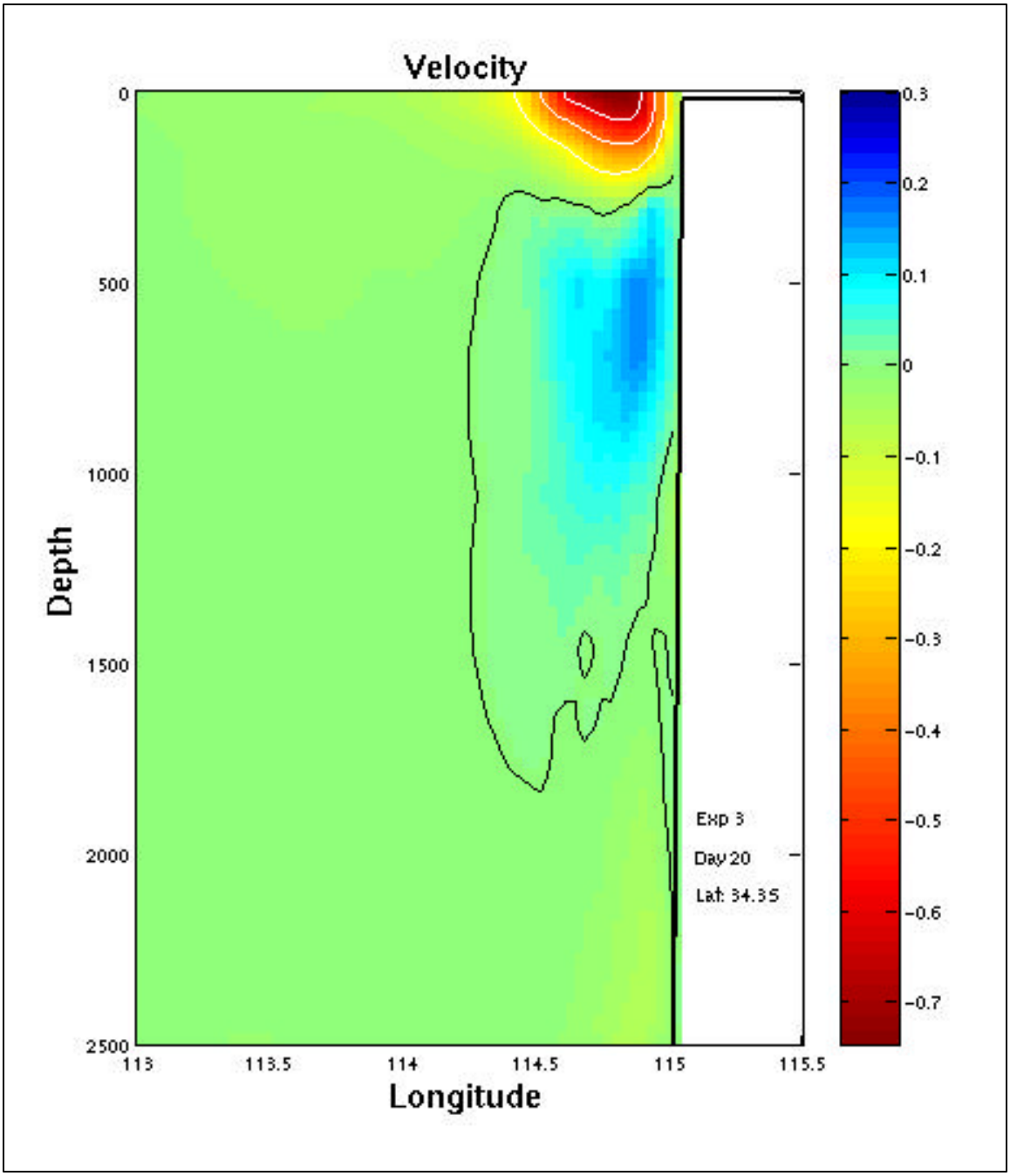

Figure 11b. Cross-section of north-south velocities (m/s) at Cape Leeuwin (34.3°S) for Experiment 3 day 20. Blue is equatorward (north).

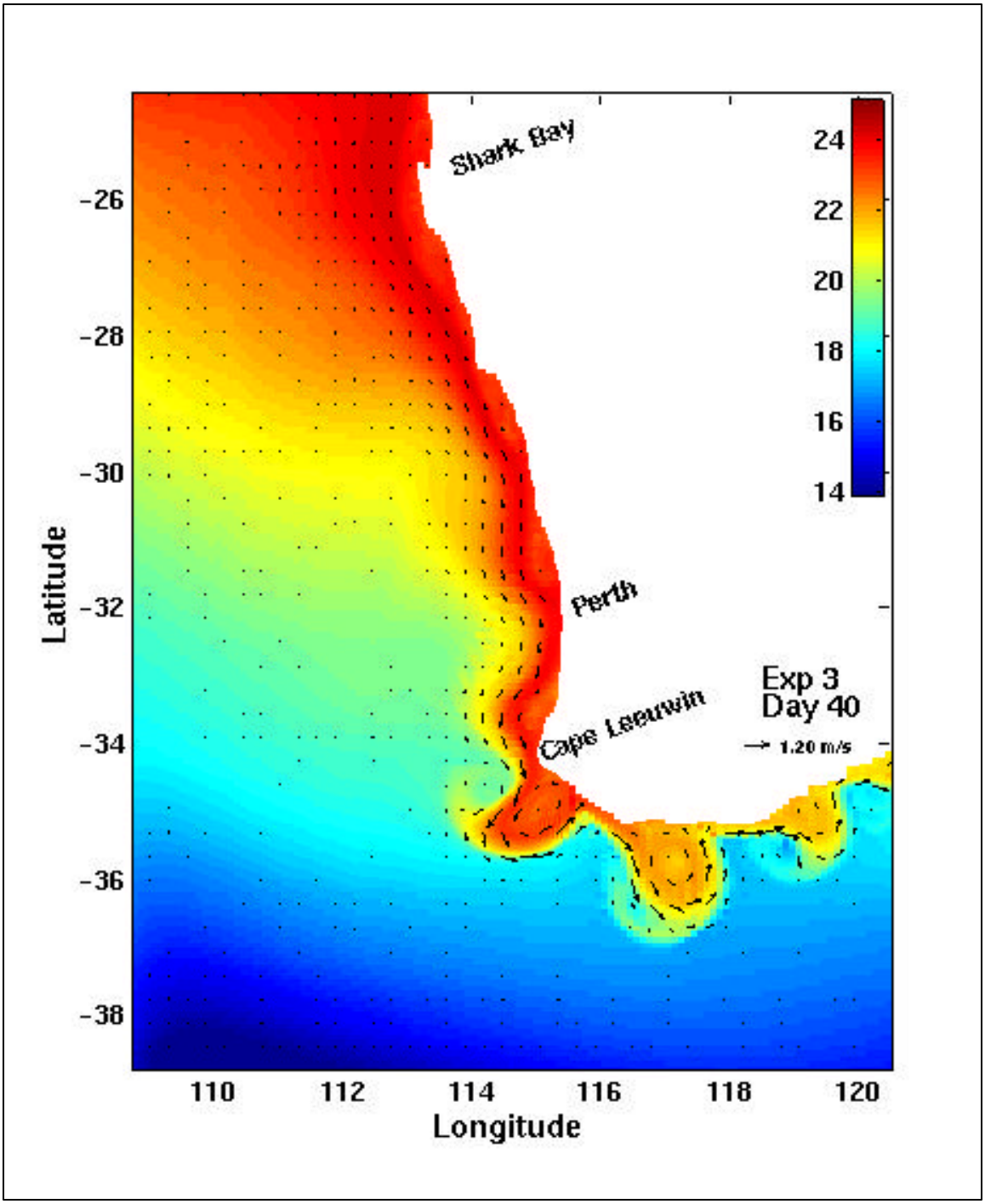

Figure 11c. Surface temperature (°C) and velocity vectors for Experiment 3 on day 40.

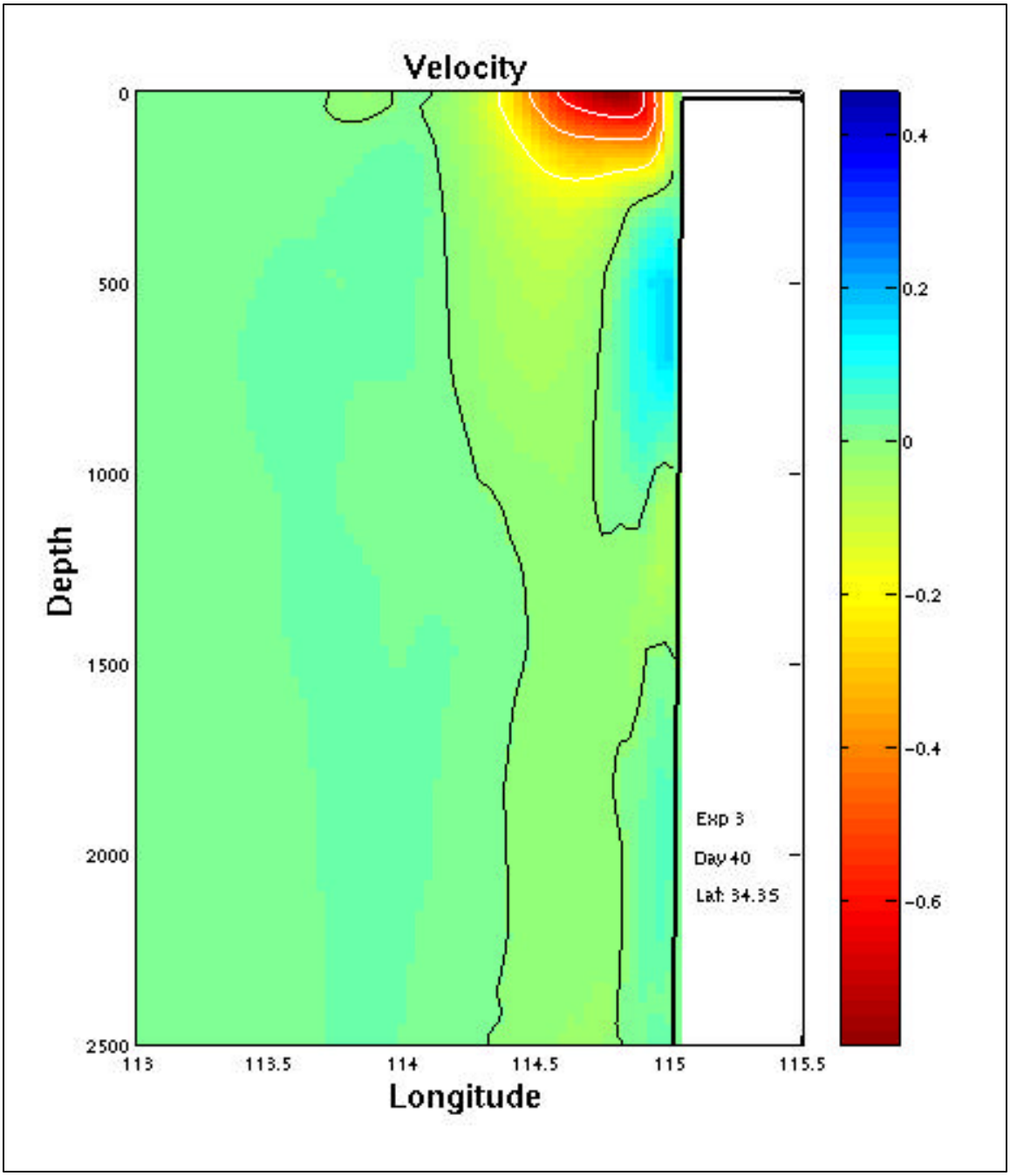

Figure 11d. Cross-section of north-south velocities (m/s) at Cape Leeuwin (34.3°S) for Experiment 3 day 40. Blue is equatorward (north).

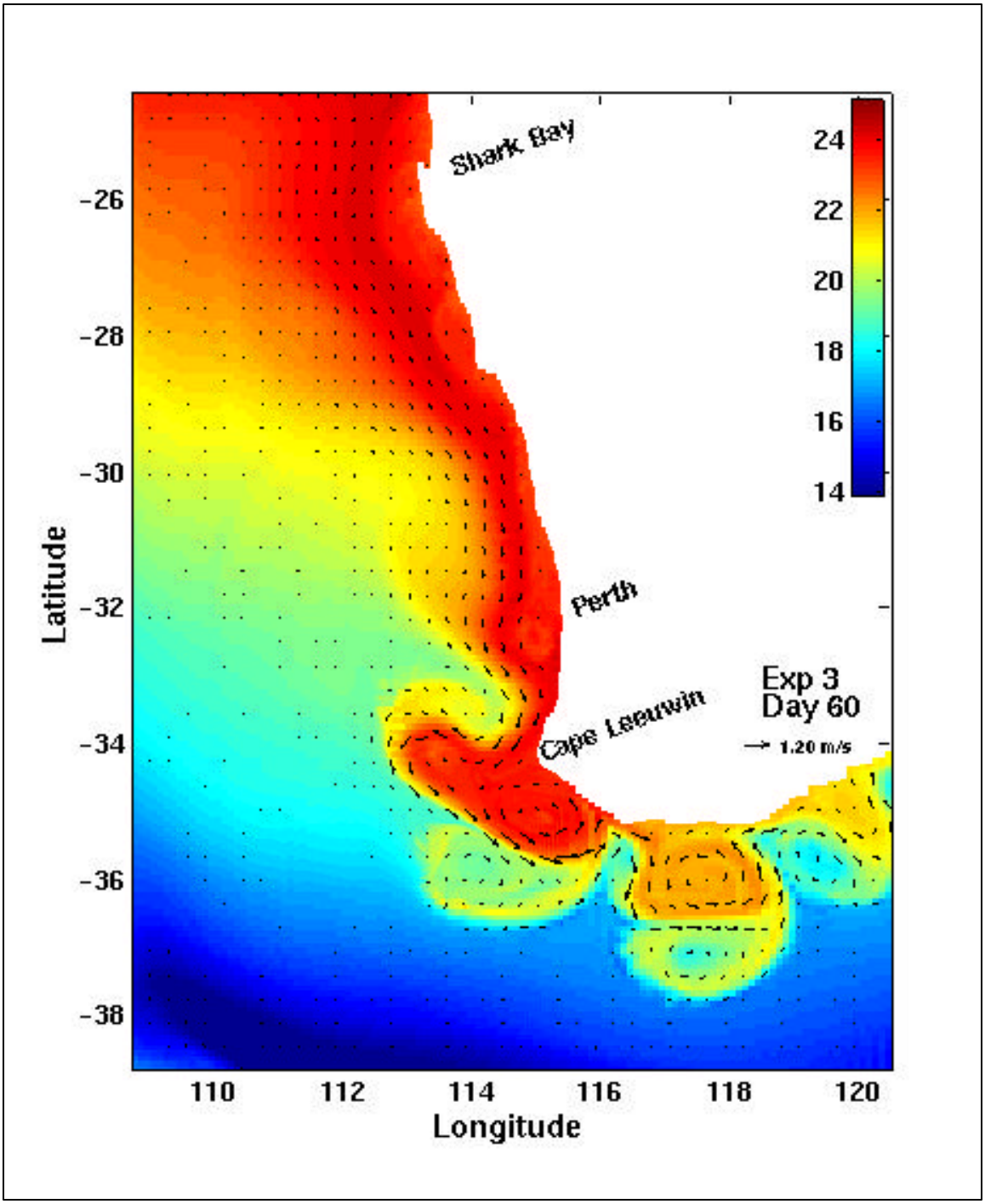

Figure 11e. Surface temperature (°C) and velocity vectors for Experiment 3 on day 60.

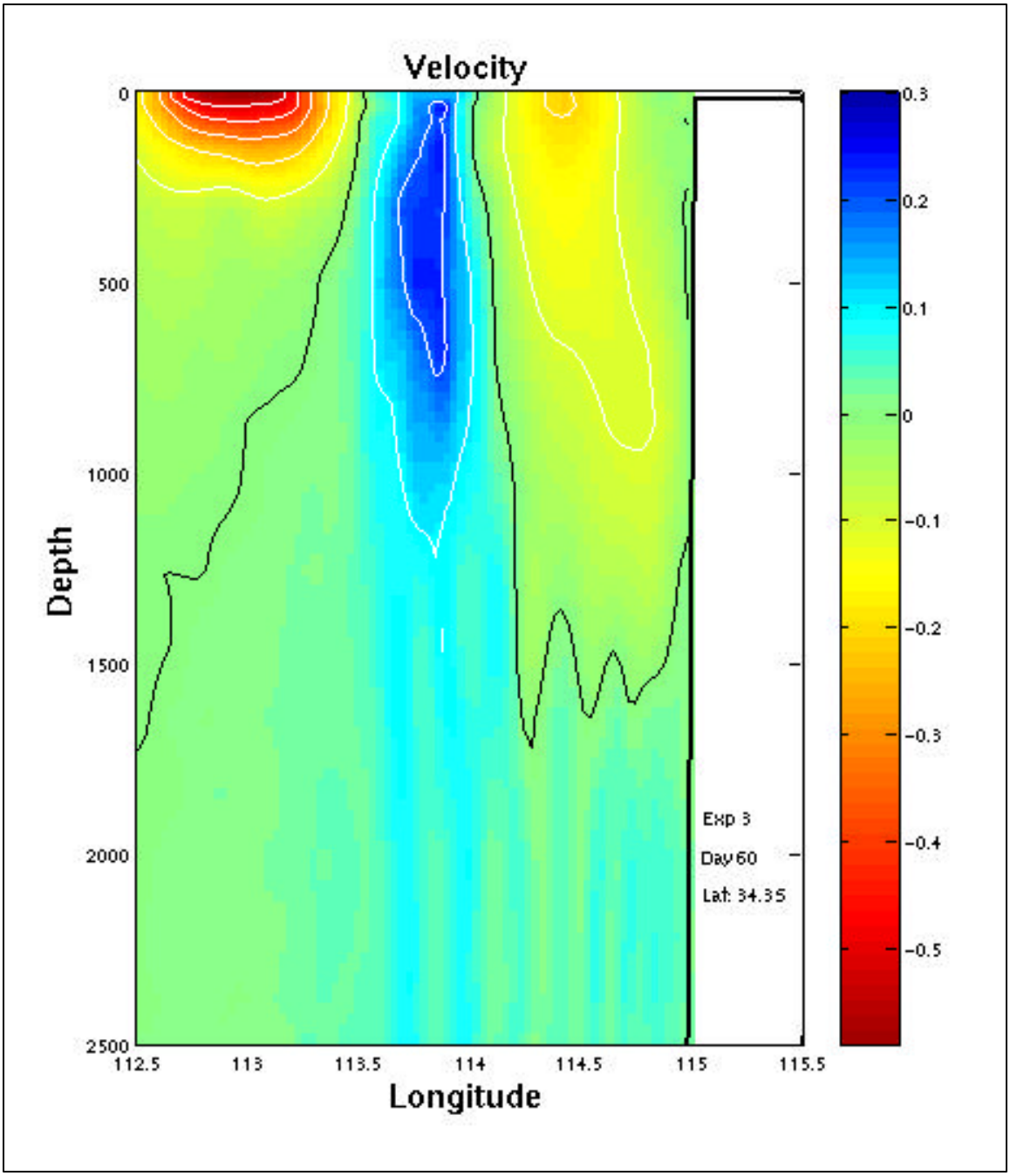

Figure 11f. Cross-section of north-south velocities (m/s) at Cape Leeuwin (34.3°S) for Experiment 3 day 60. Blue is equatorward (north).

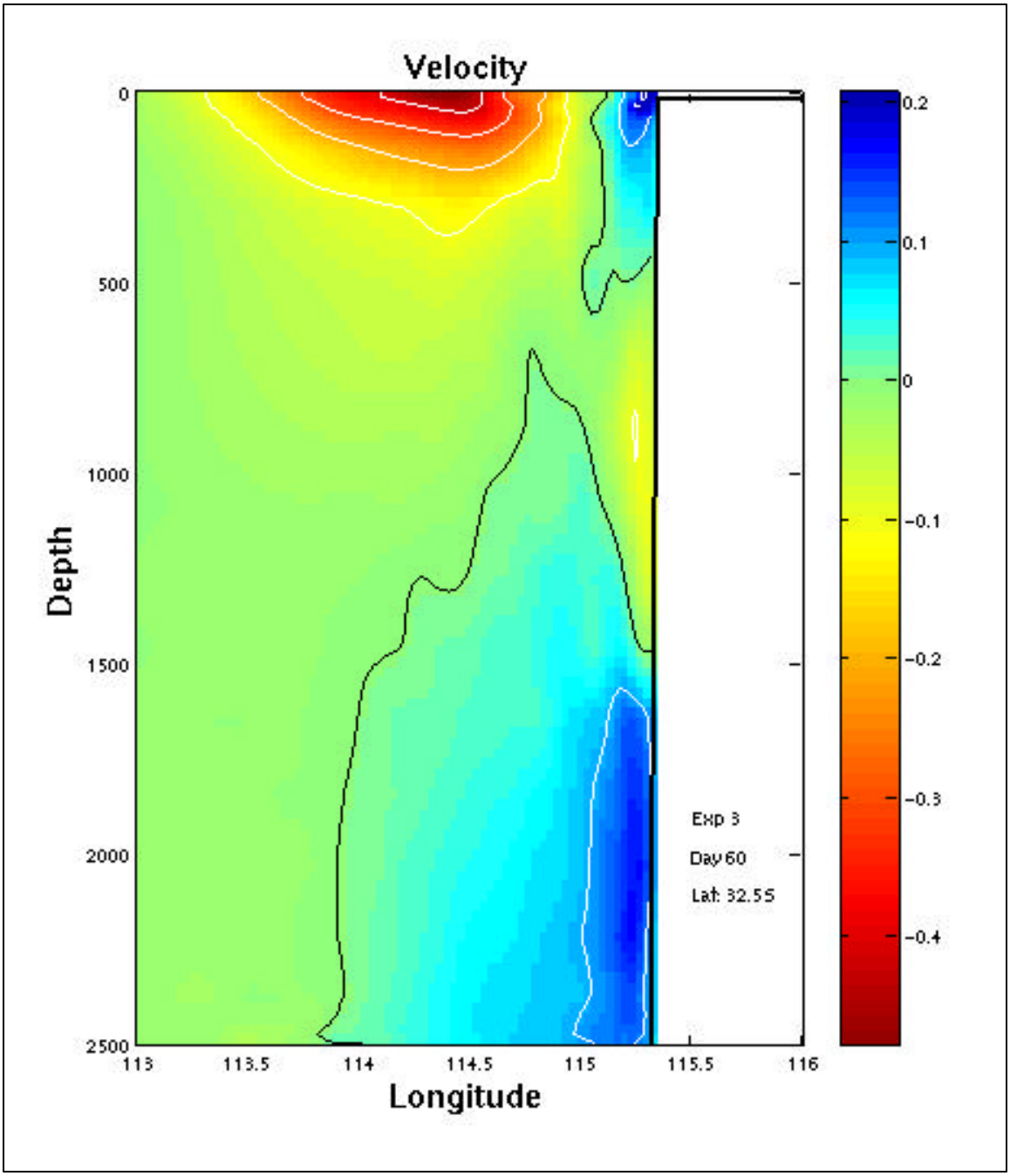

Figure 11g. Cross-section of north-south velocities (m/s) at Perth (32.5°S) for Experiment 3 day 60. Blue is equatorward (north).

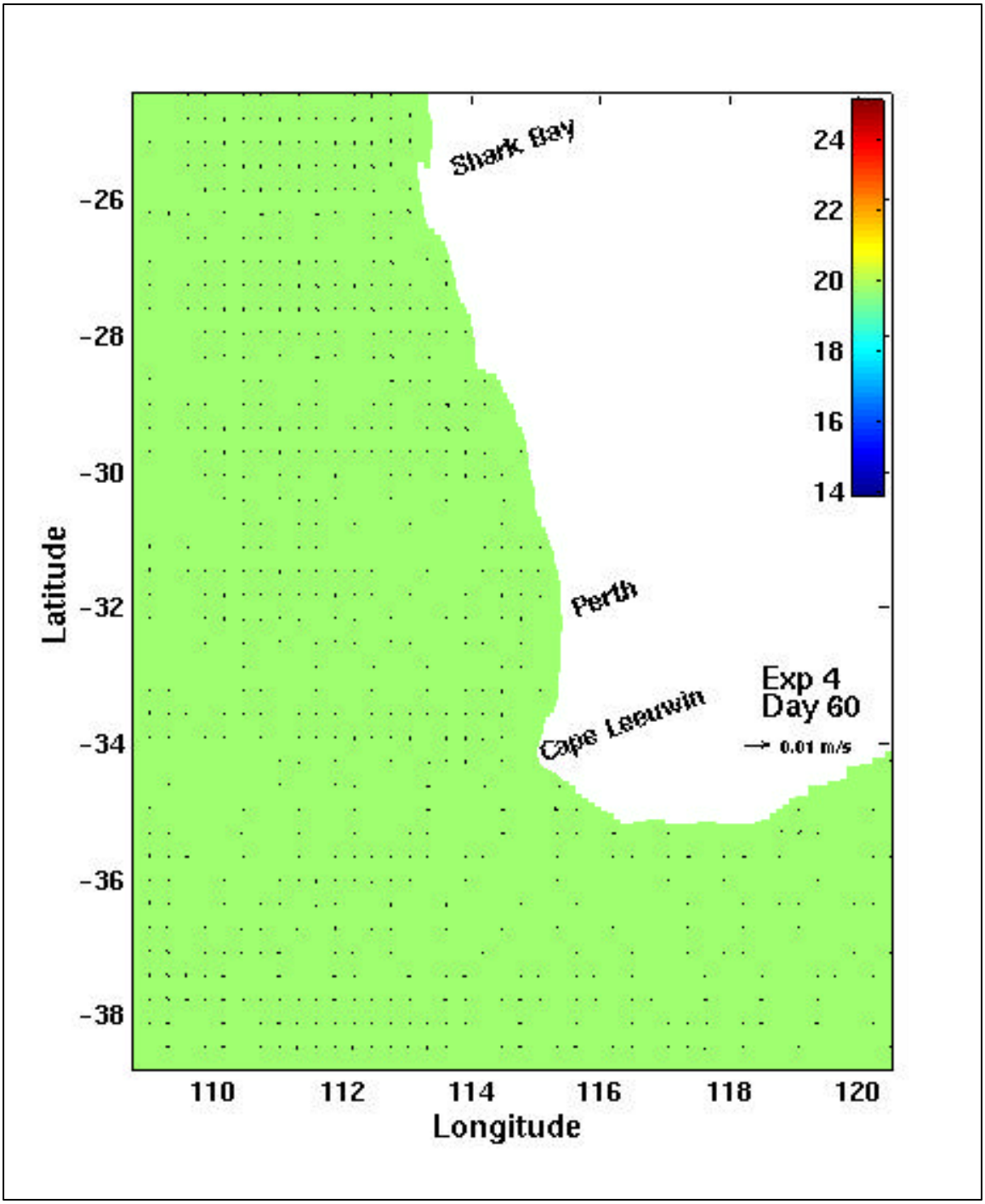

Figure 12. Surface velocity error (m/s) due to the pressure gradient force error on day 60 for Experiment 4.

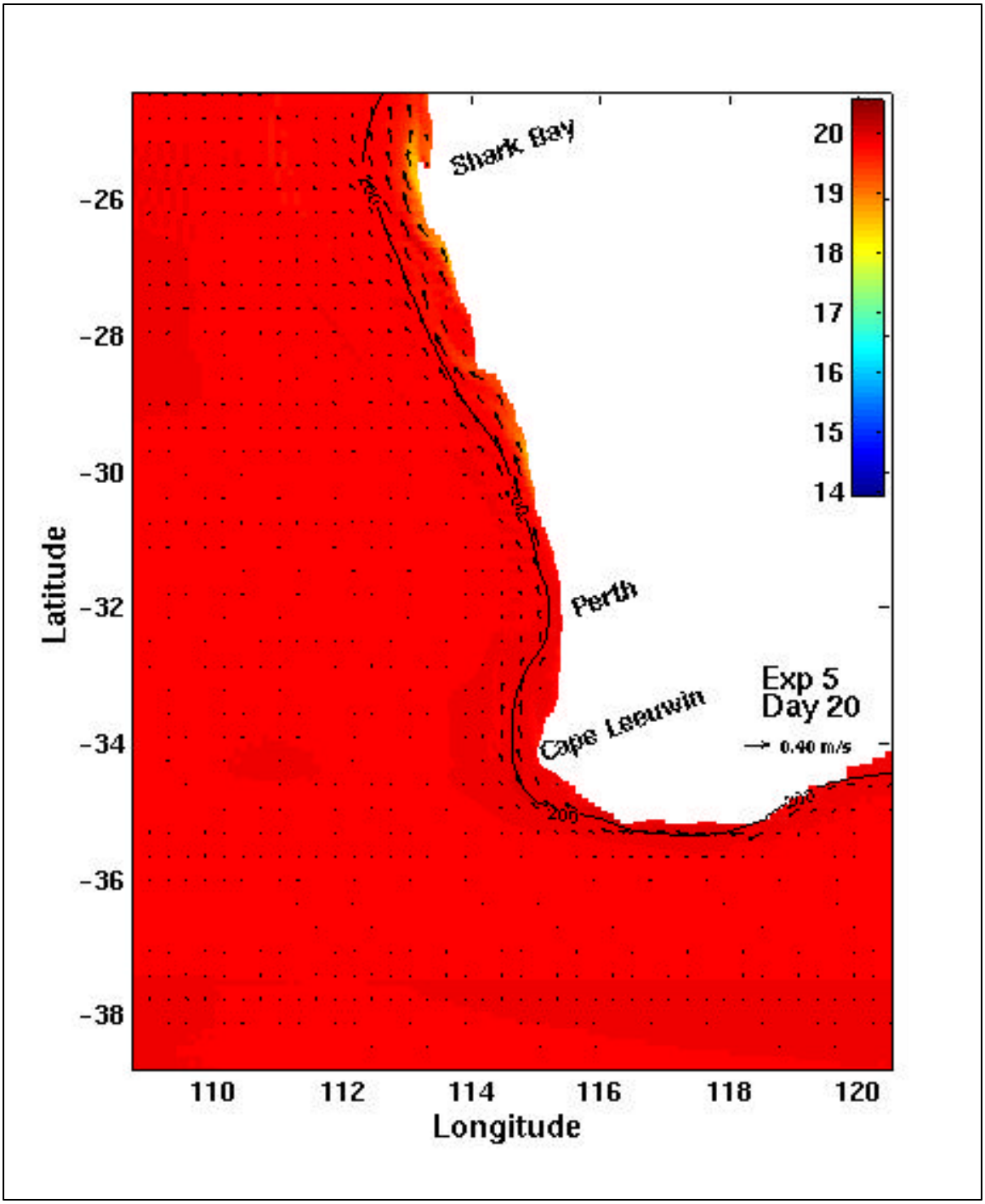

Figure 13a. Surface temperature (°C) and velocity vectors for Experiment 5 on day 20. In this and subsequent horizontal plots, the 200 m isobath is shown by the solid line.

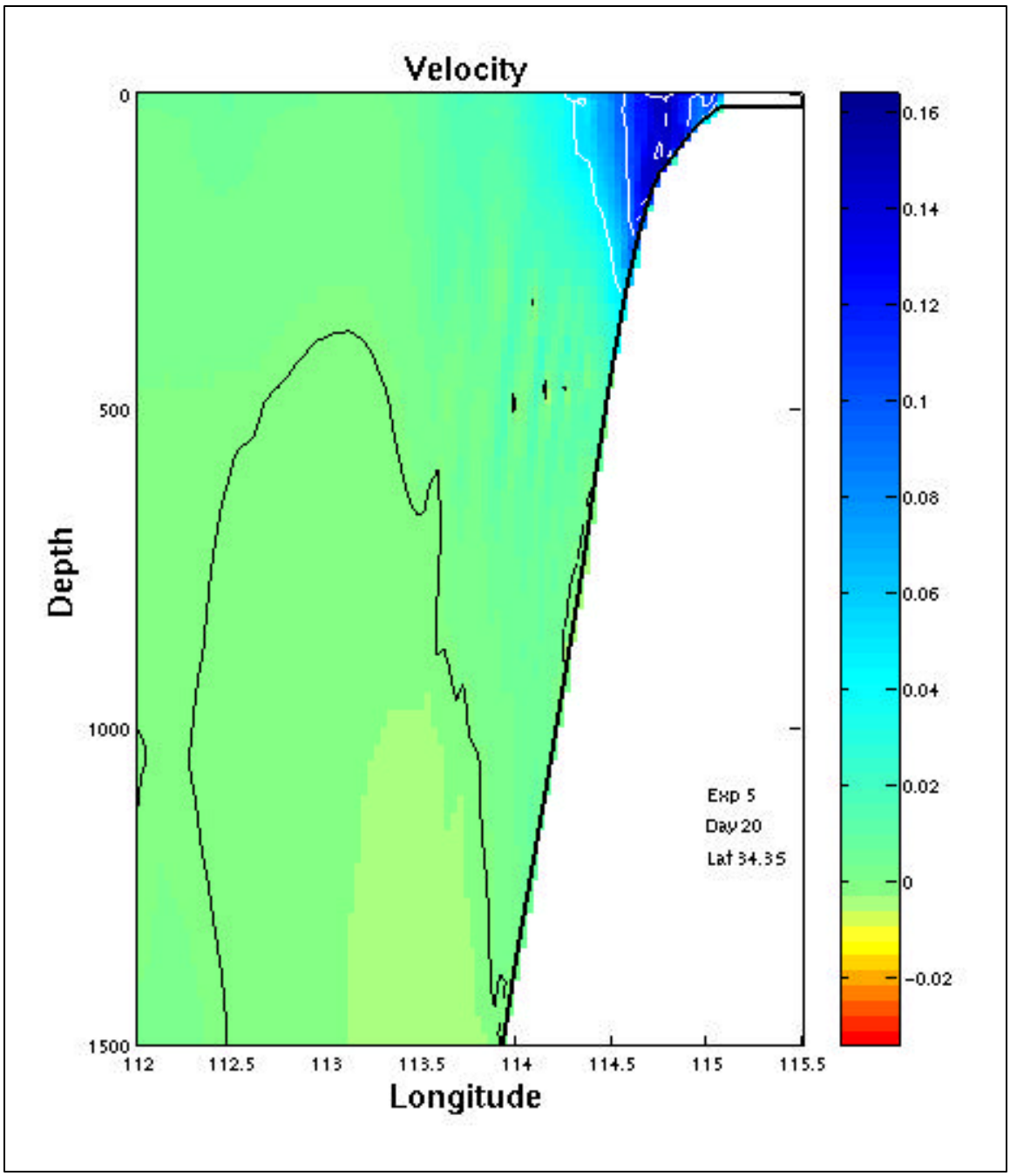

Figure 13b. Cross-section of north-south velocities (m/s) at Cape Leeuwin (34.3°S) for Experiment 5 day 20. Blue is equatorward (north).

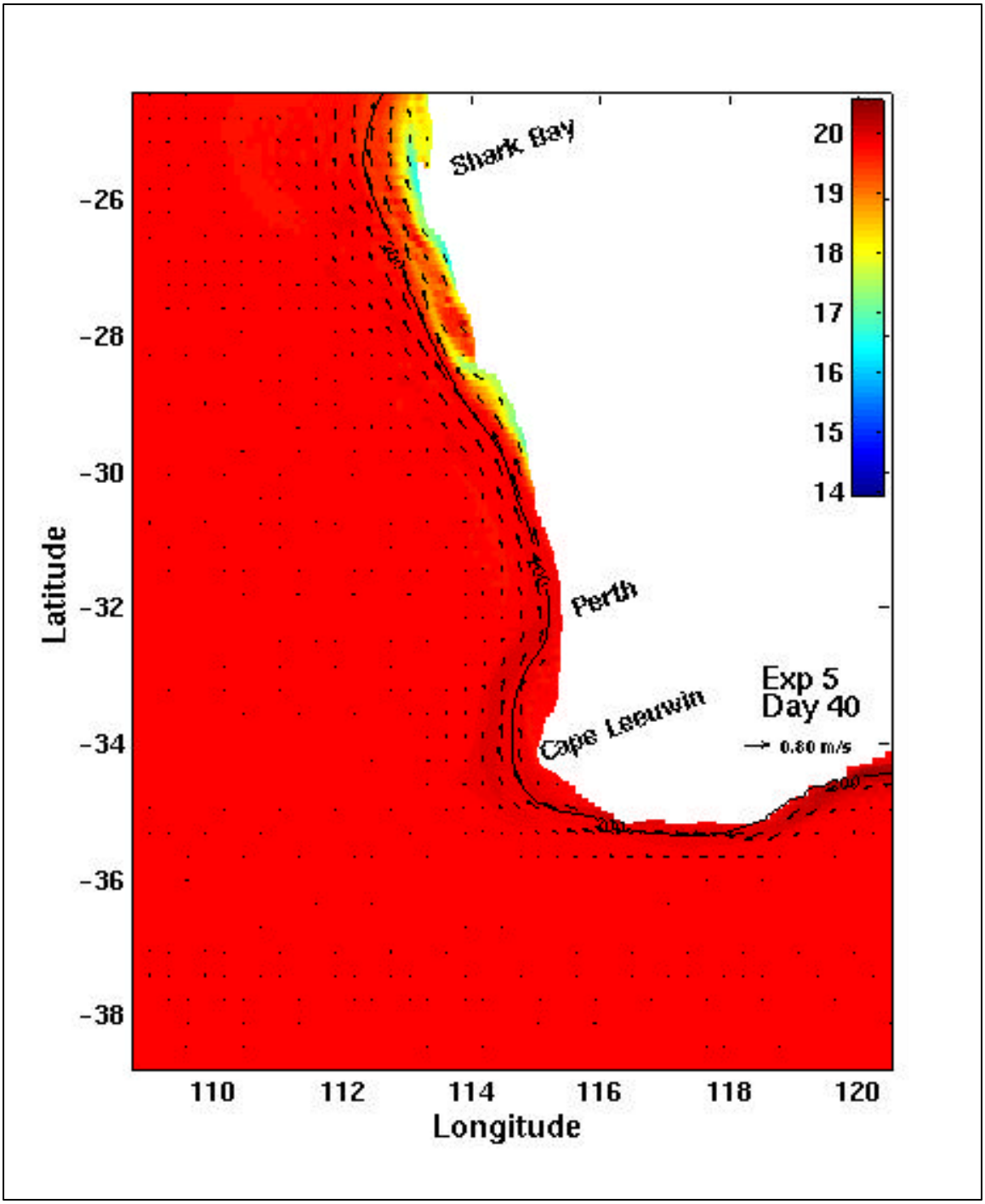

Figure 13c. Surface temperature (°C) and velocity vectors for Experiment 5 on day 40.

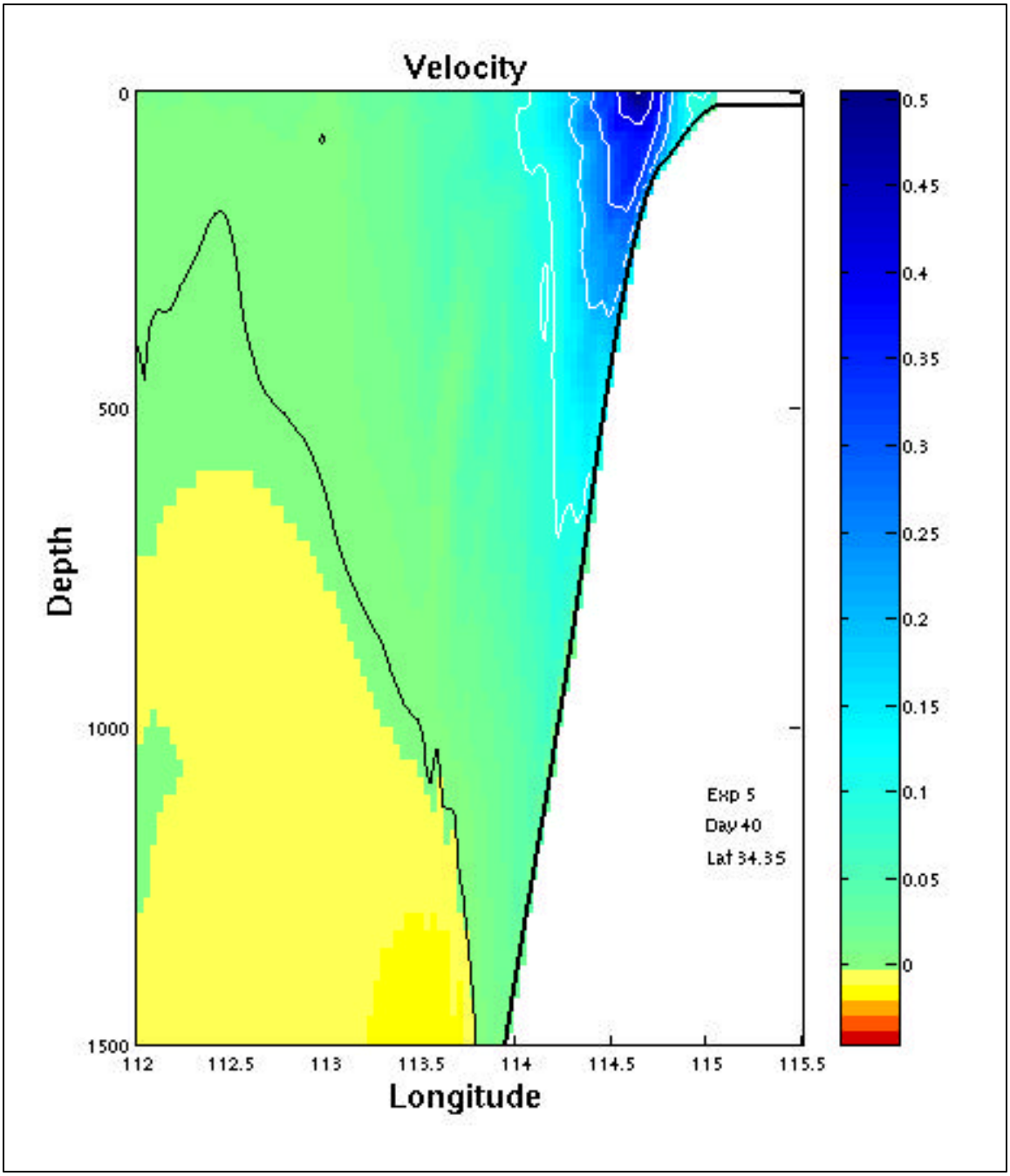

Figure 13d. Cross-section of north-south velocities (m/s) at Cape Leeuwin (34.3°S) for Experiment 5 day 40. Blue is equatorward (north).

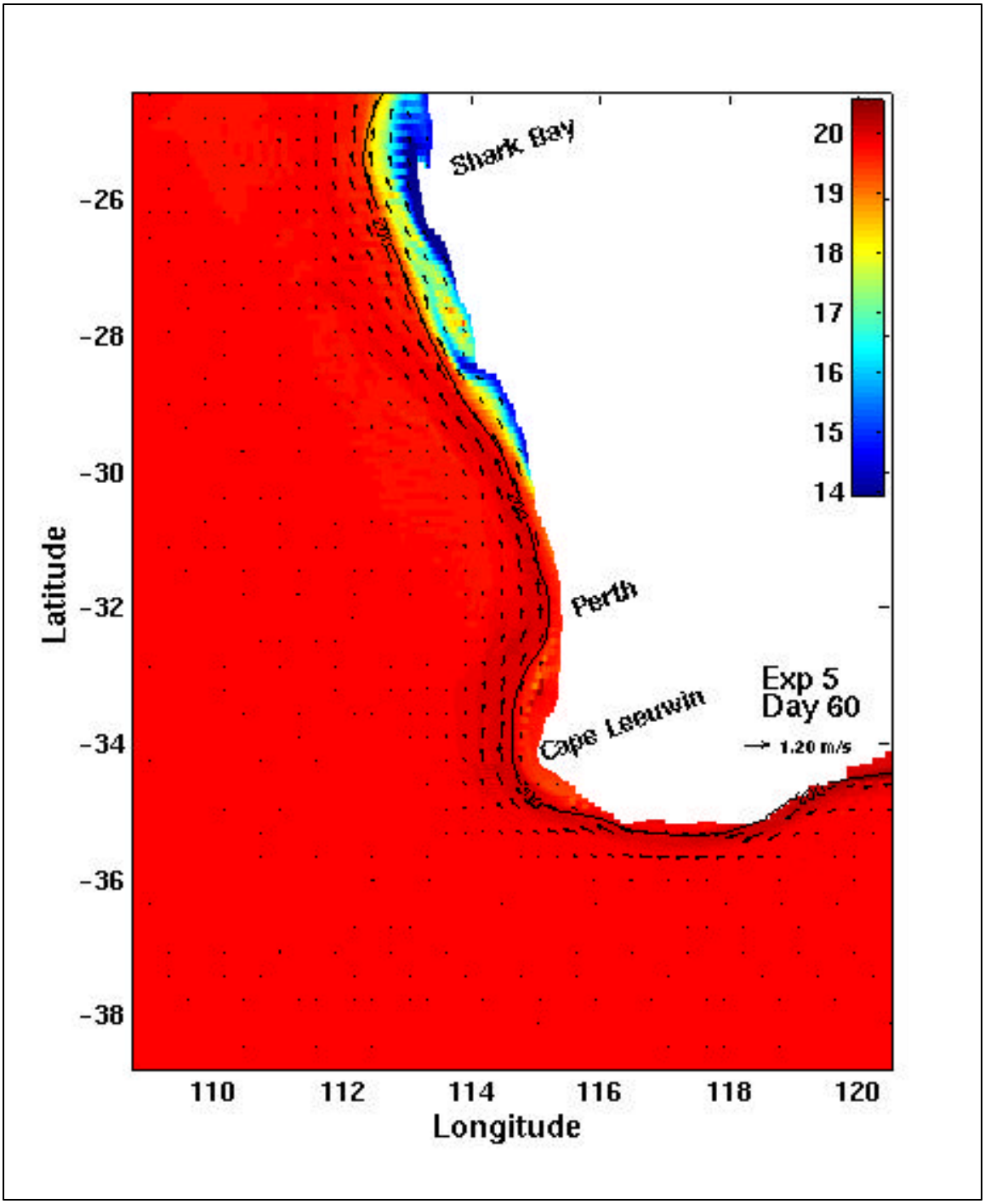

Figure 13e. Surface temperature (°C) and velocity vectors for Experiment 5 on day 60.

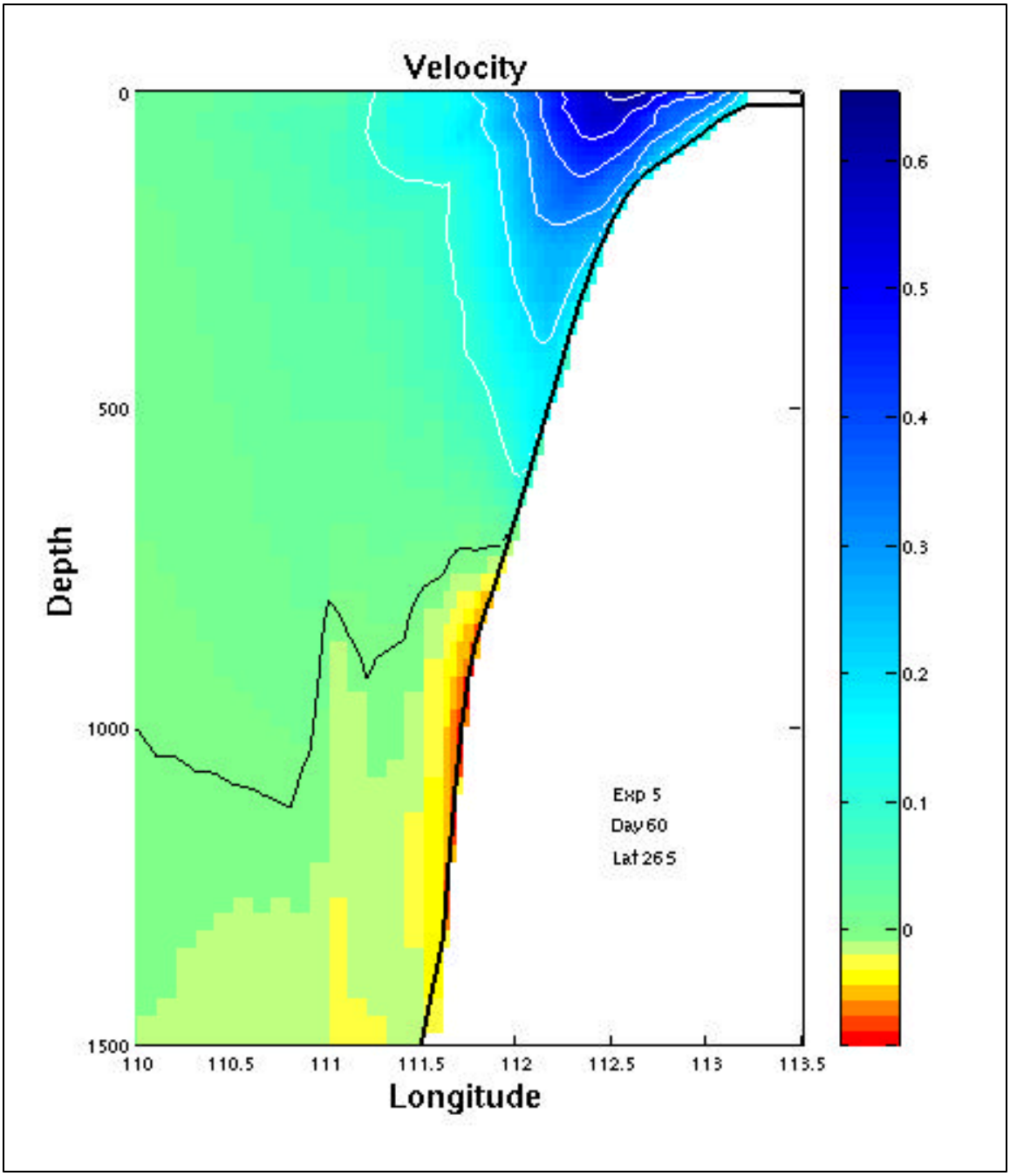

Figure 13f. Cross-section of north-south velocities (m/s) at 26°S for Experiment 5 day 60. Blue is equatorward (north).

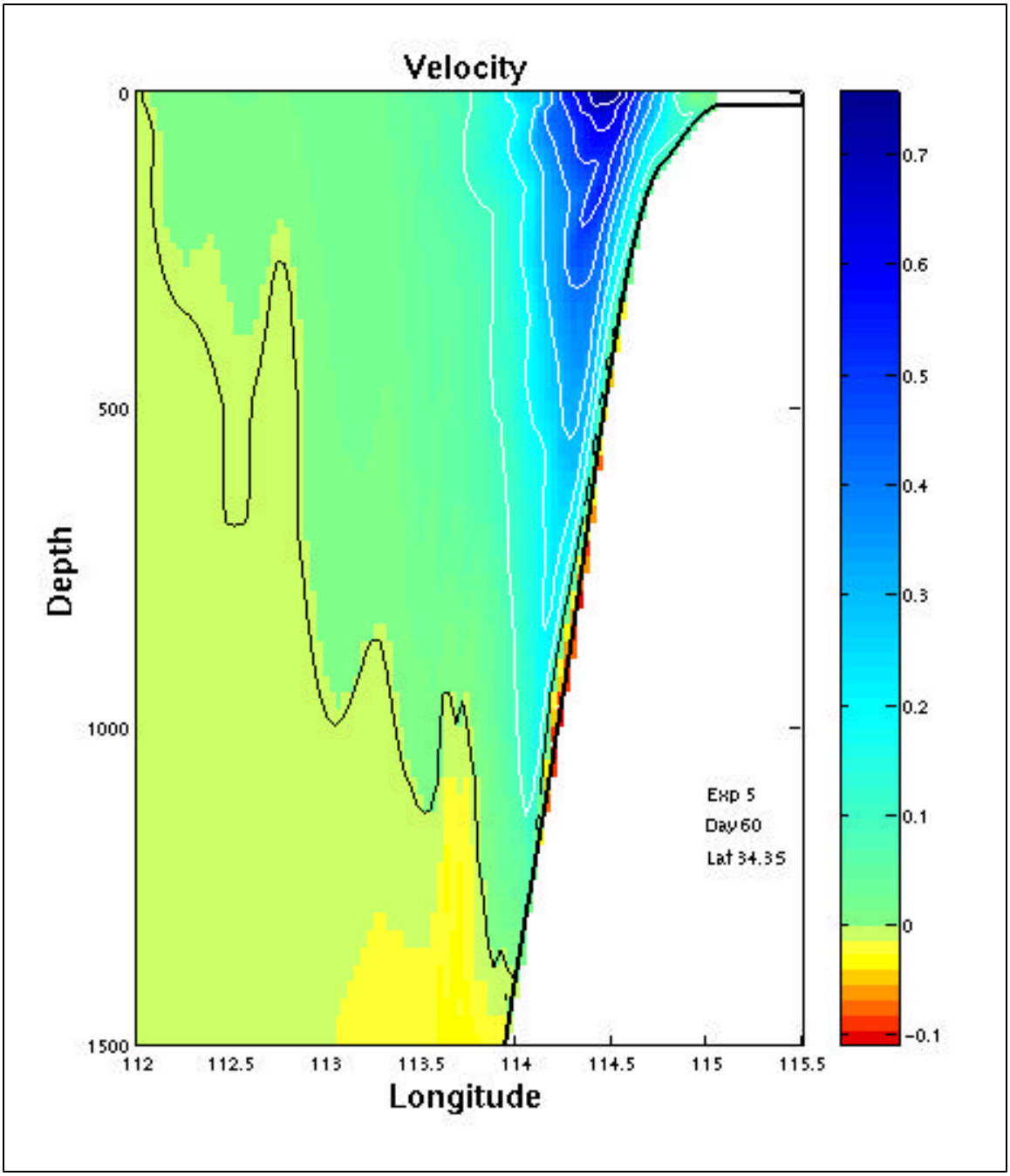

Figure 13g. Cross-section of north-south velocities (m/s) at Cape Leeuwin (34.3°S) for Experiment 5 day 60. Blue is equatorward (north).

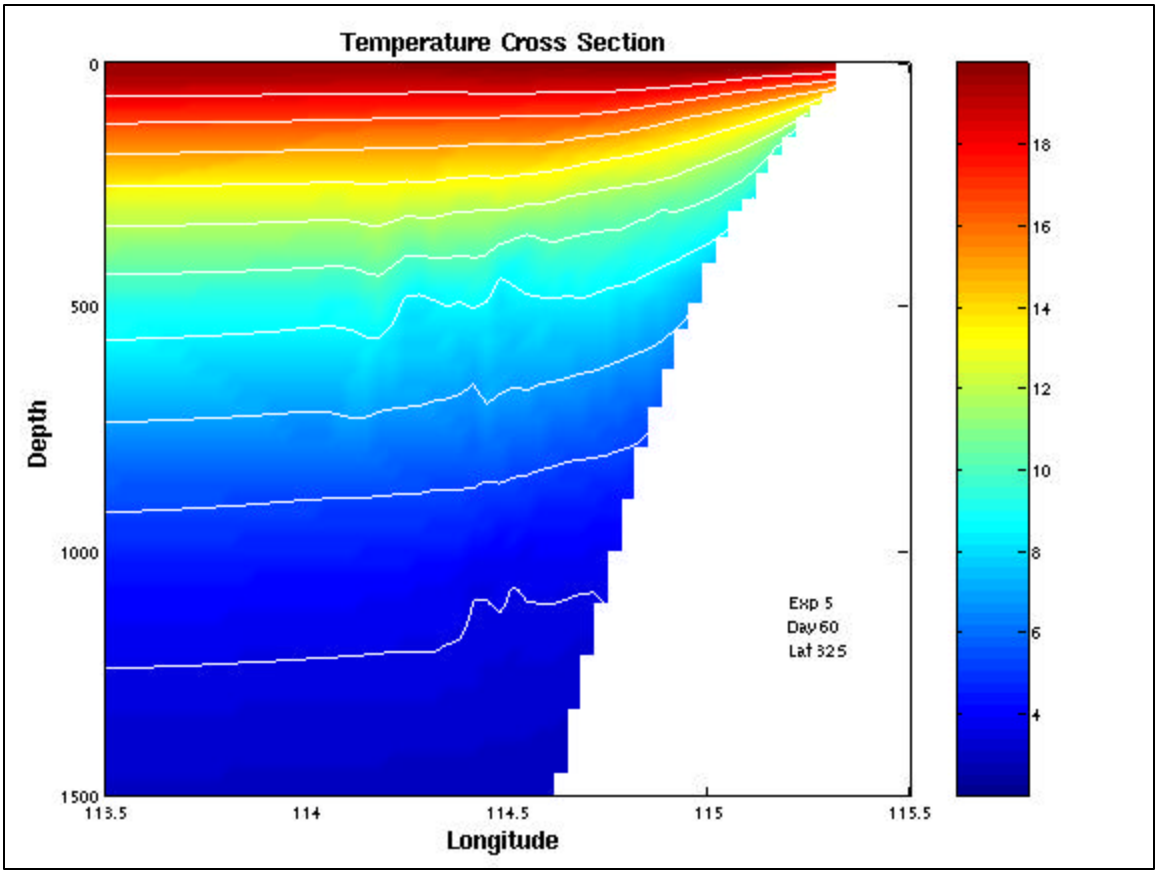

Figure 13h. Cross-section of temperature (ºC) at 32ºS for Experiment 5 day 60, with a contour intervals of two degrees.

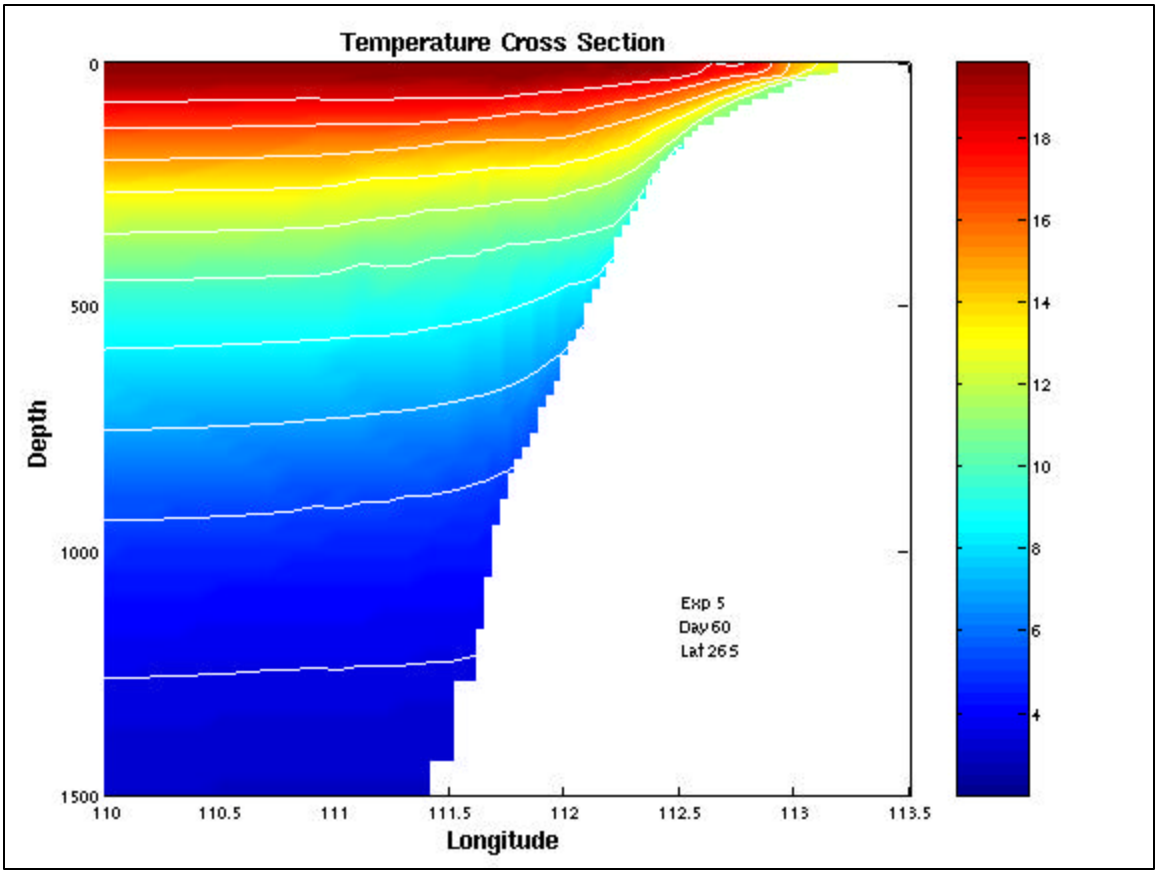

Figure 13i. Cross-section of temperature (ºC) at 26ºS for Experiment 5 day 60, with a contour intervals of two degrees.

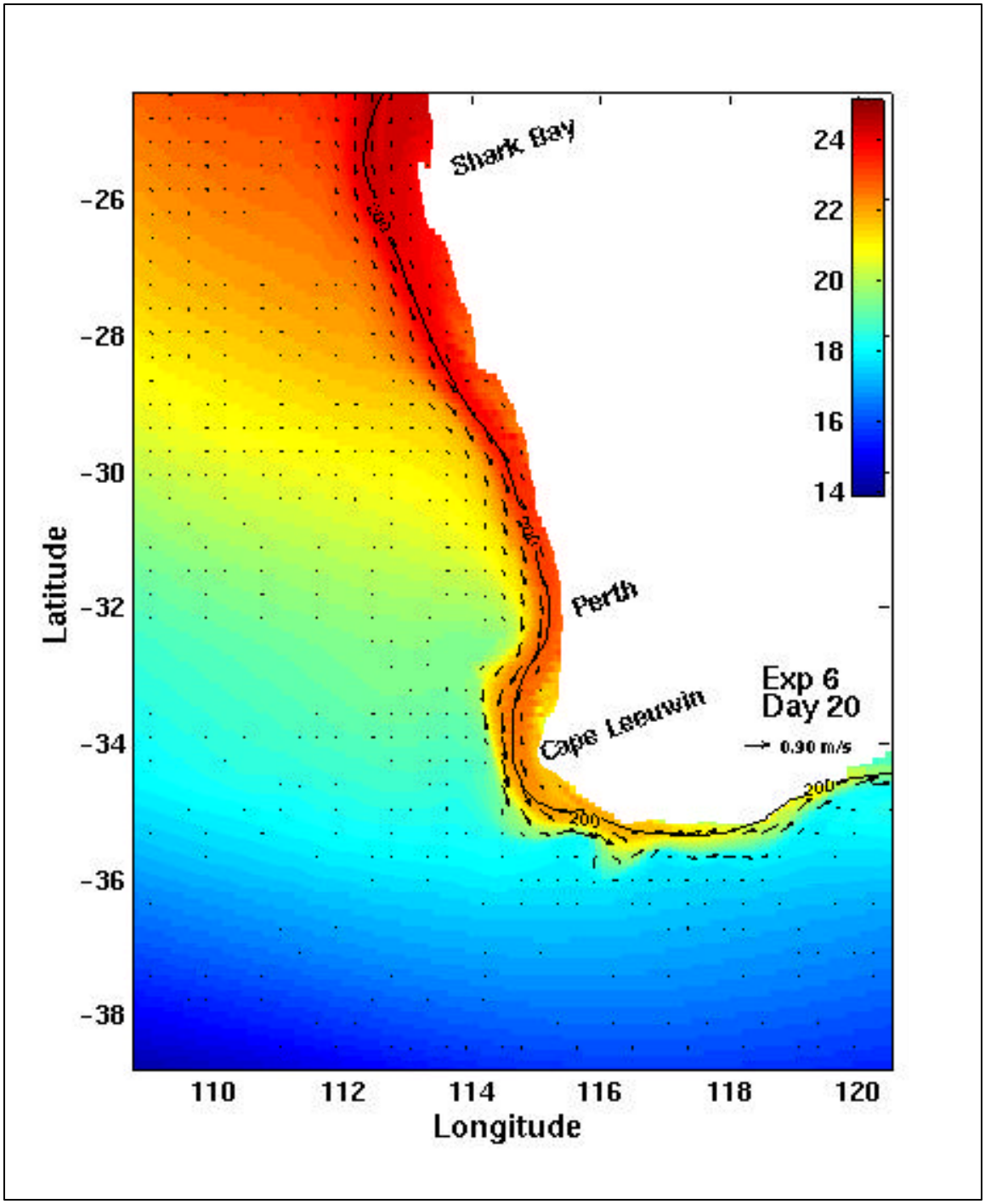

Figure 14a. Surface temperature (°C) and velocity vectors for Experiment 6 on day 20.

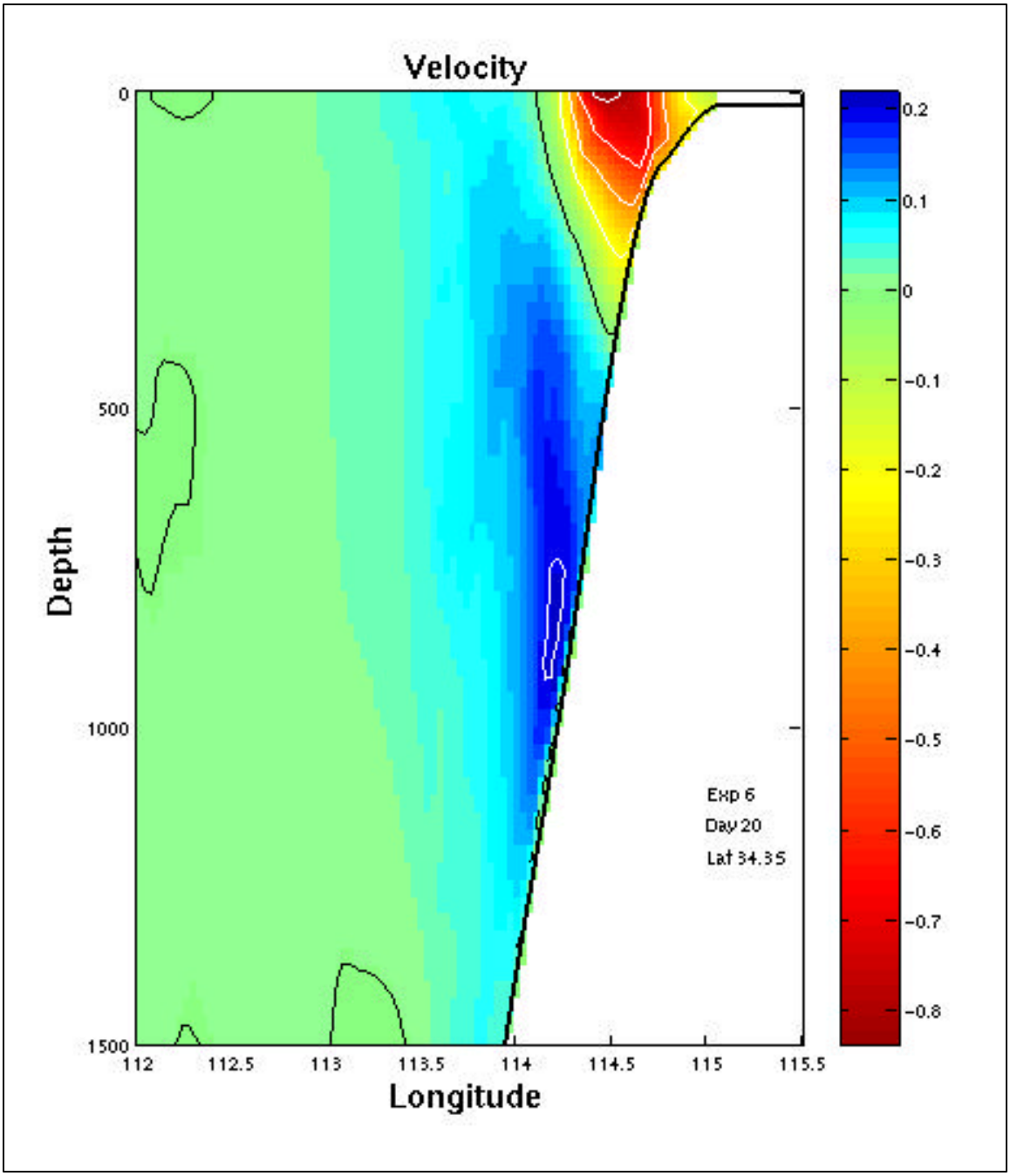

Figure 14b. Cross-section of north-south velocities (m/s) at Cape Leeuwin (34.3°S) for Experiment 6 day 20. Blue is equatorward (north).

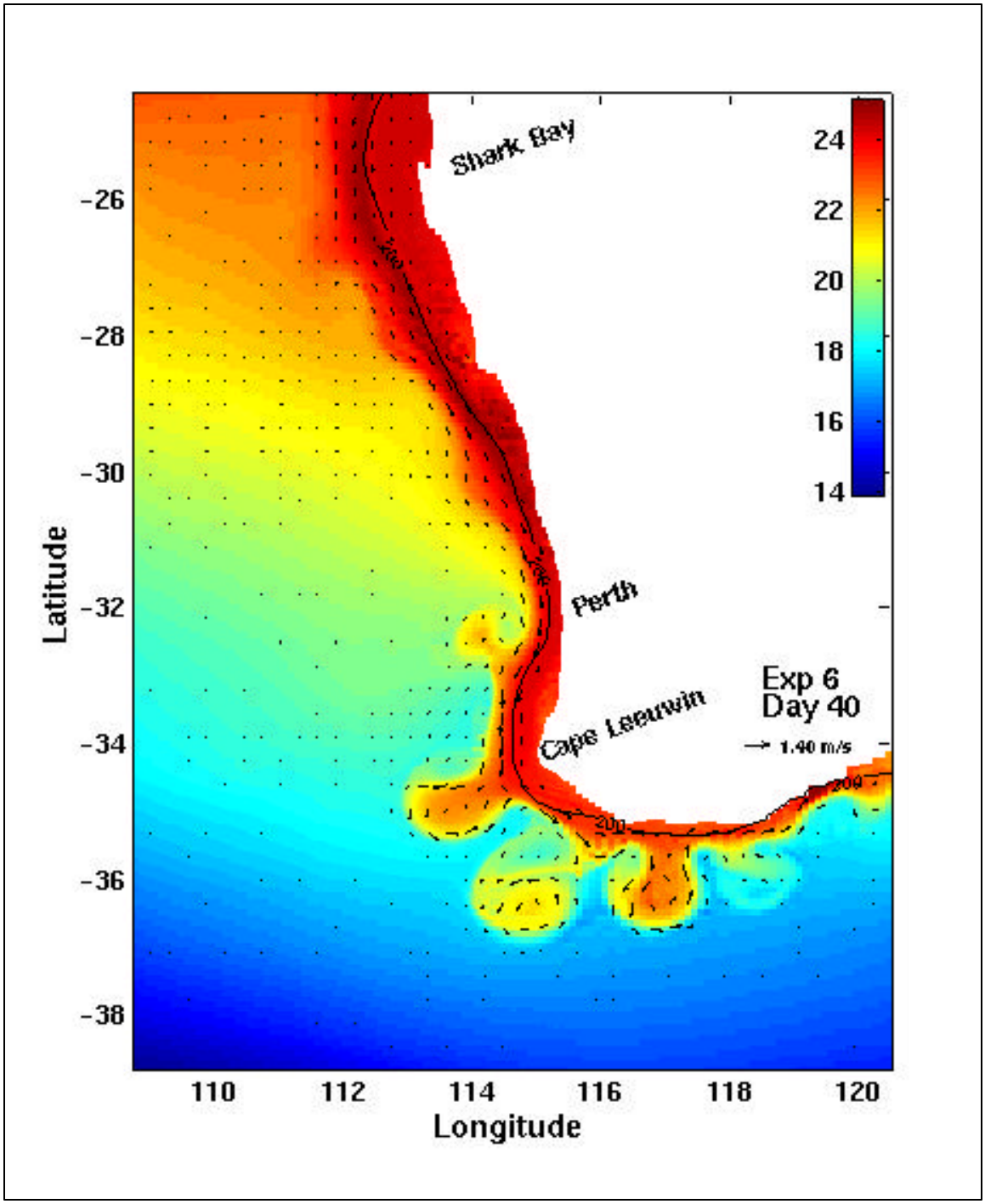

Figure 14c. Surface temperature (°C) and velocity vectors for Experiment 6 on day 40.

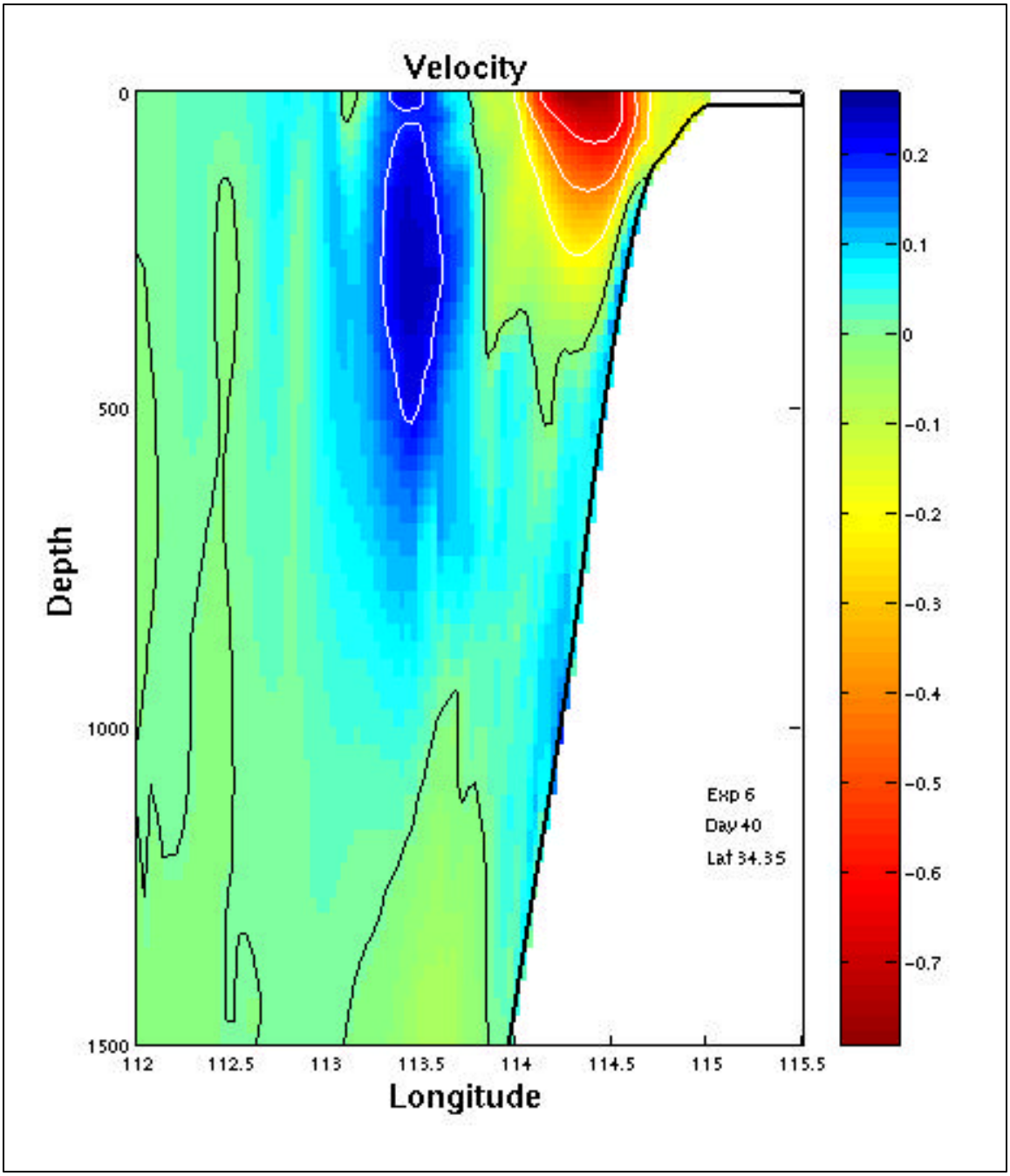

Figure 14d. Cross-section of north-south velocities (m/s) at Cape Leeuwin (34.3°S) for Experiment 6 day 40. Blue is equatorward (north).

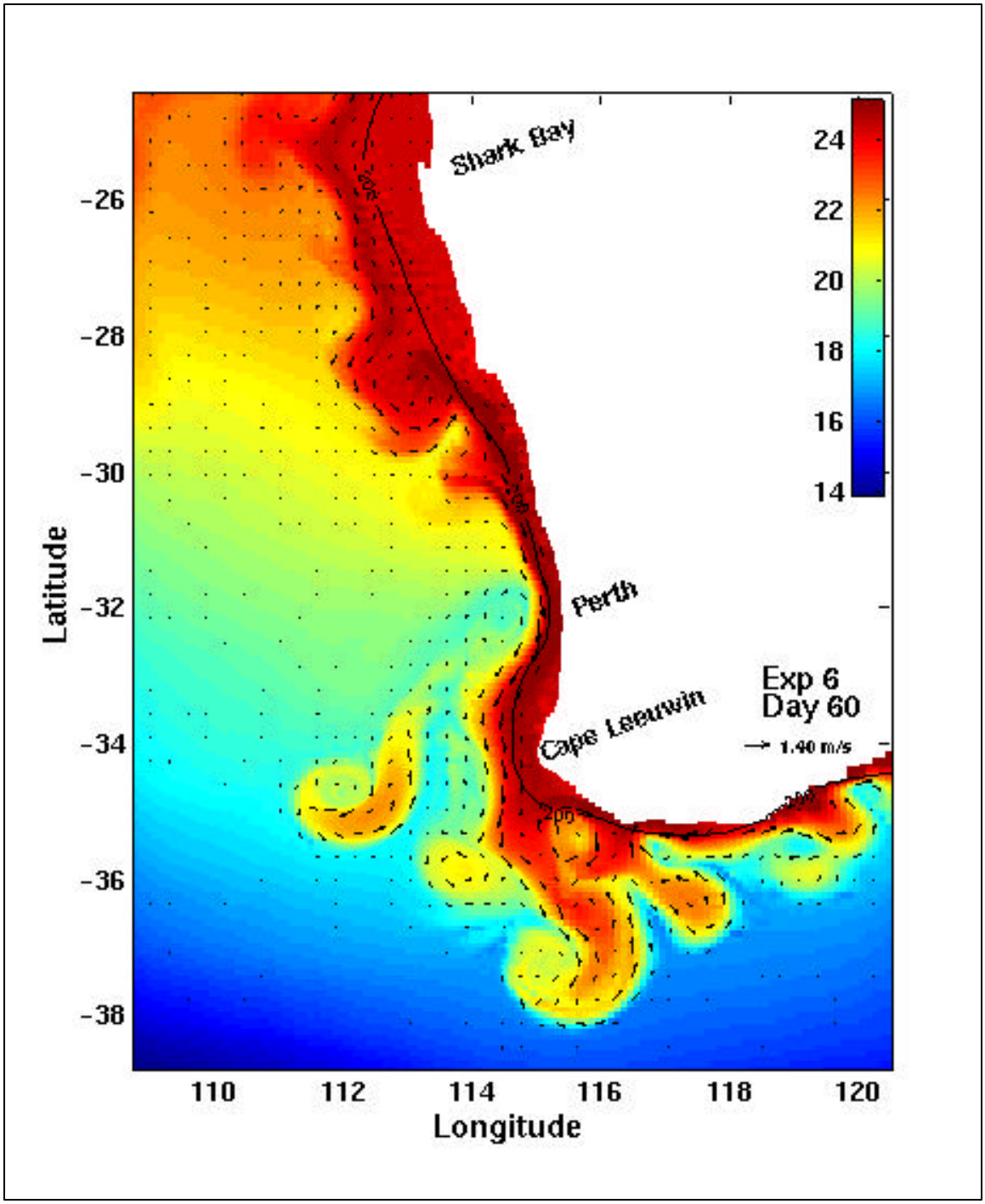

Figure 14e. Surface temperature (°C) and velocity vectors for Experiment 6 on day 60.

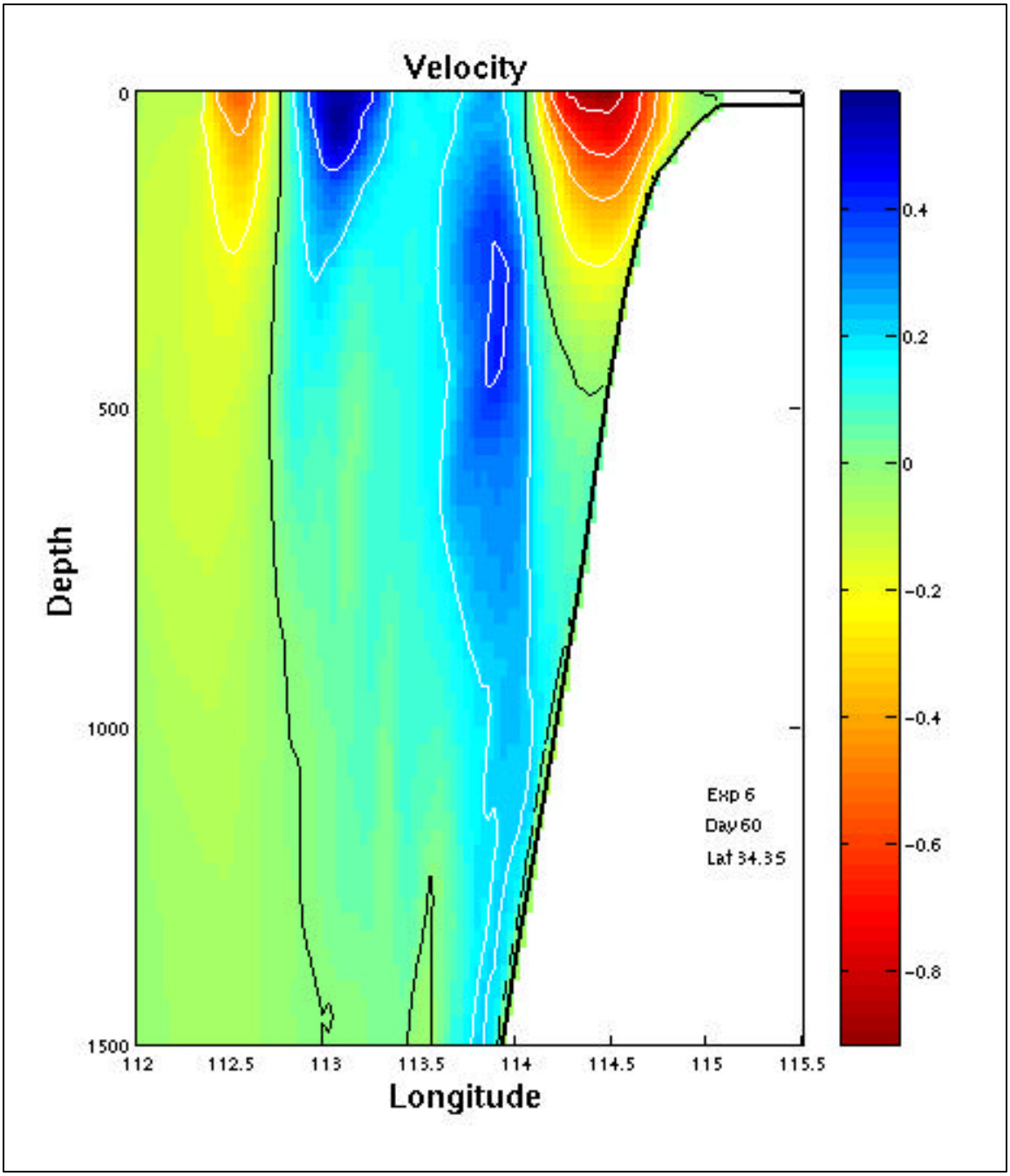

Figure 14f. Cross-section of north-south velocities (m/s) at Cape Leeuwin (34.3°S) for Experiment 6 day 60. Blue is equatorward (north).

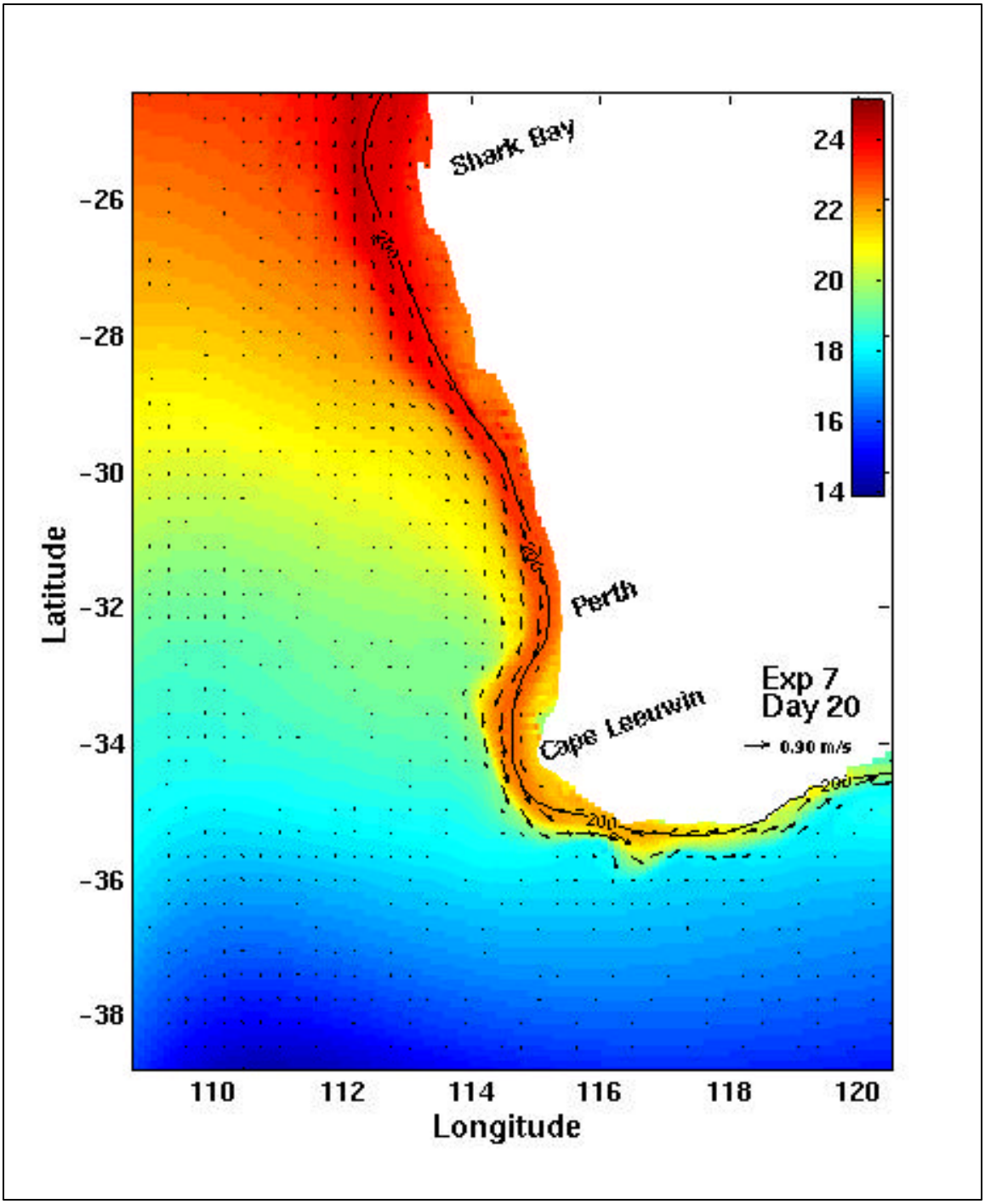

Figure 15a. Surface temperature (°C) and velocity vectors for Experiment 7 on day 20.

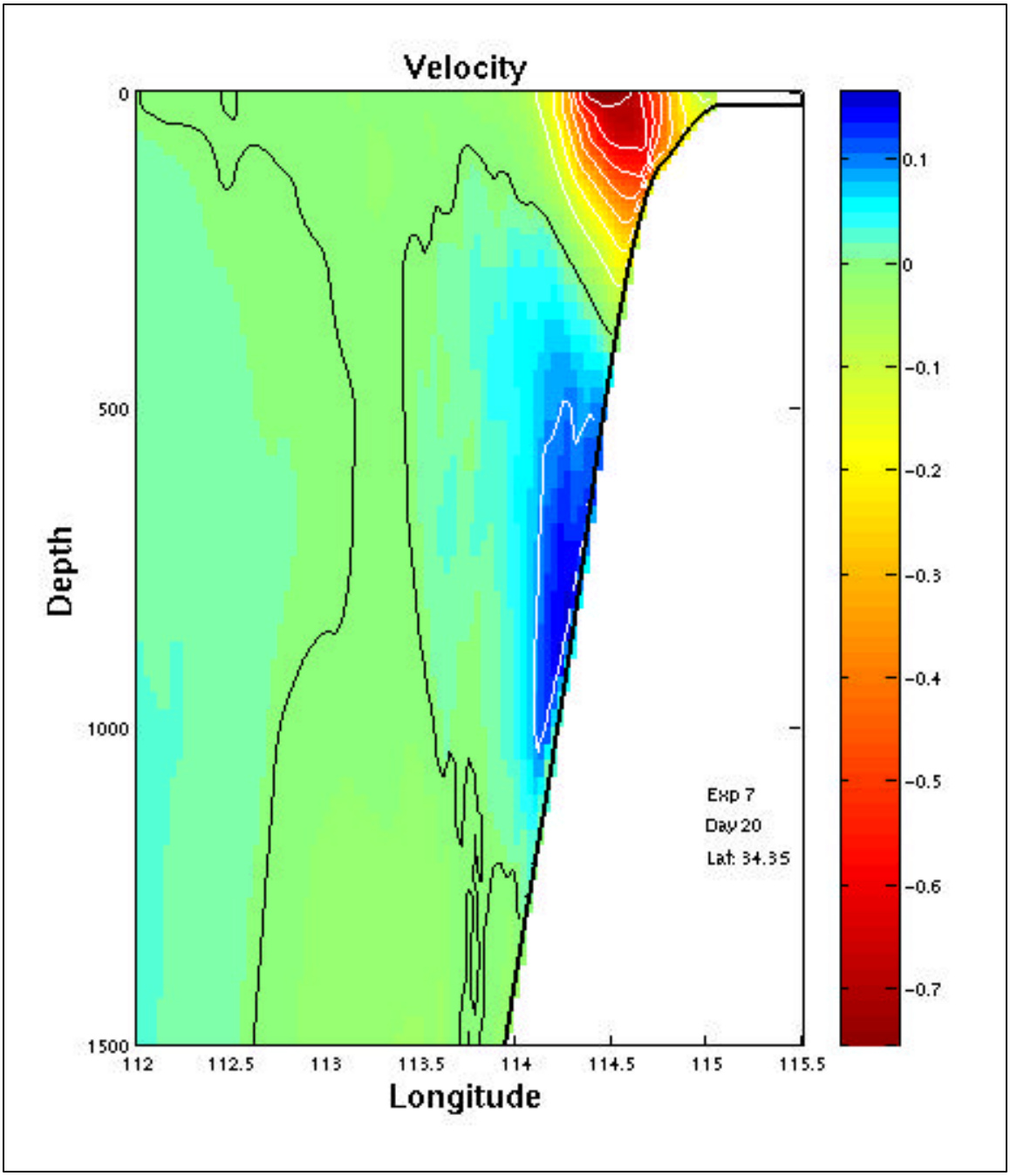

Figure 15b. Cross-section of north-south velocities (m/s) at Cape Leeuwin (34.3°S) for Experiment 7 day 20. Blue is equatorward (north).

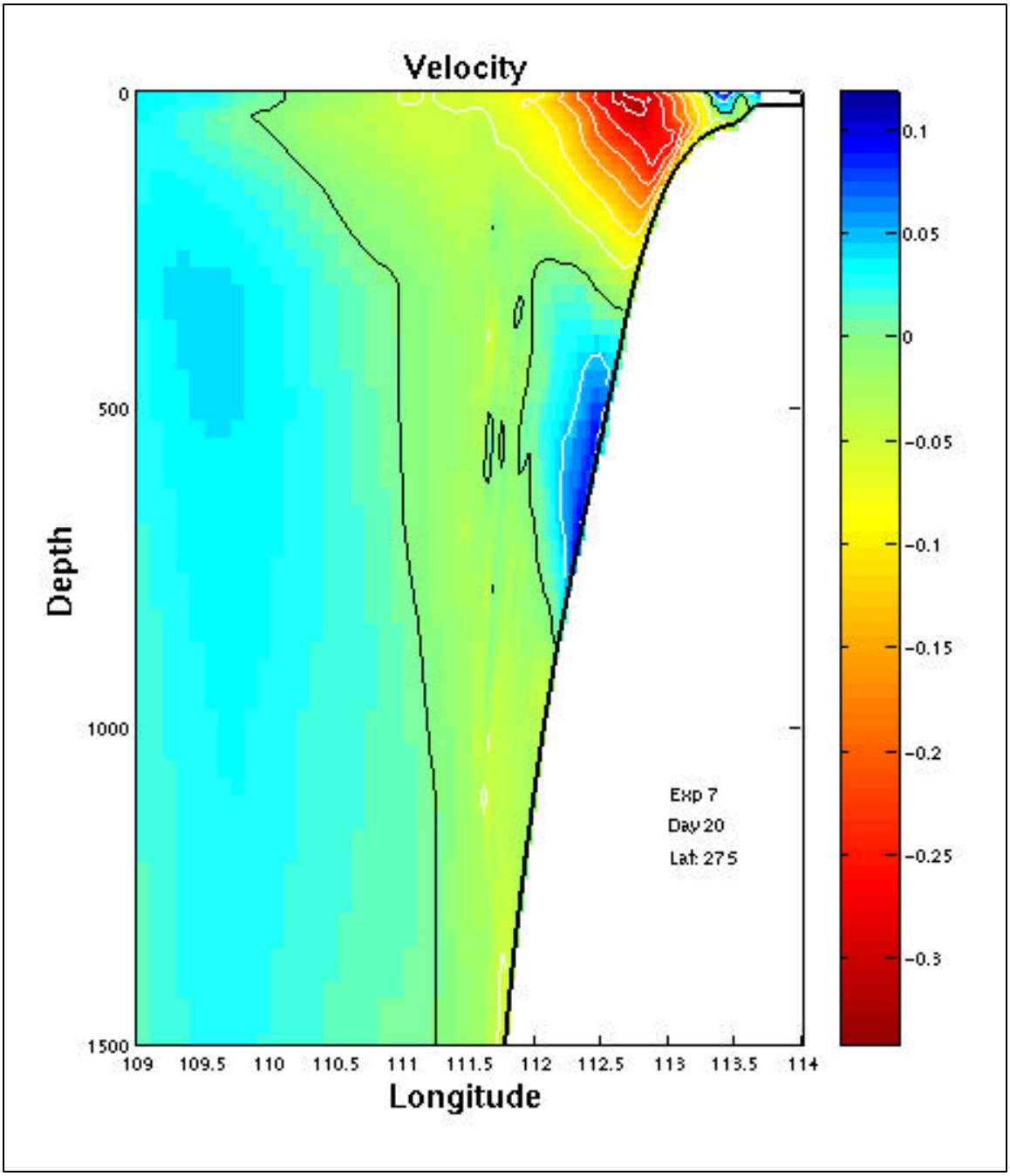

Figure 15c. Cross-section of north-south velocities (m/s) at 27°S for Experiment 7 day 20. Blue is equatorward (north).

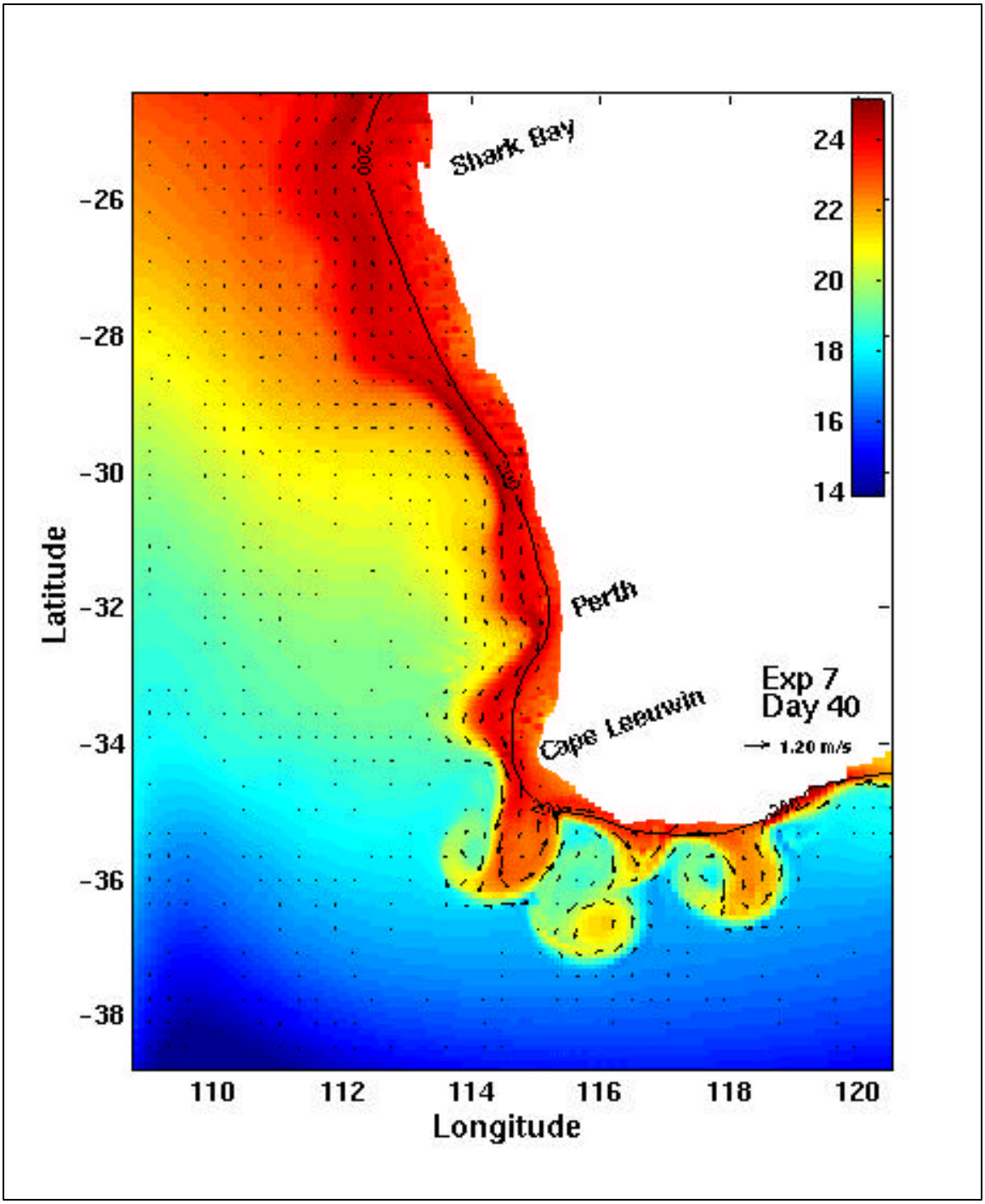

Figure 15d. Surface temperature (°C) and velocity vectors for Experiment 7 on day 40.

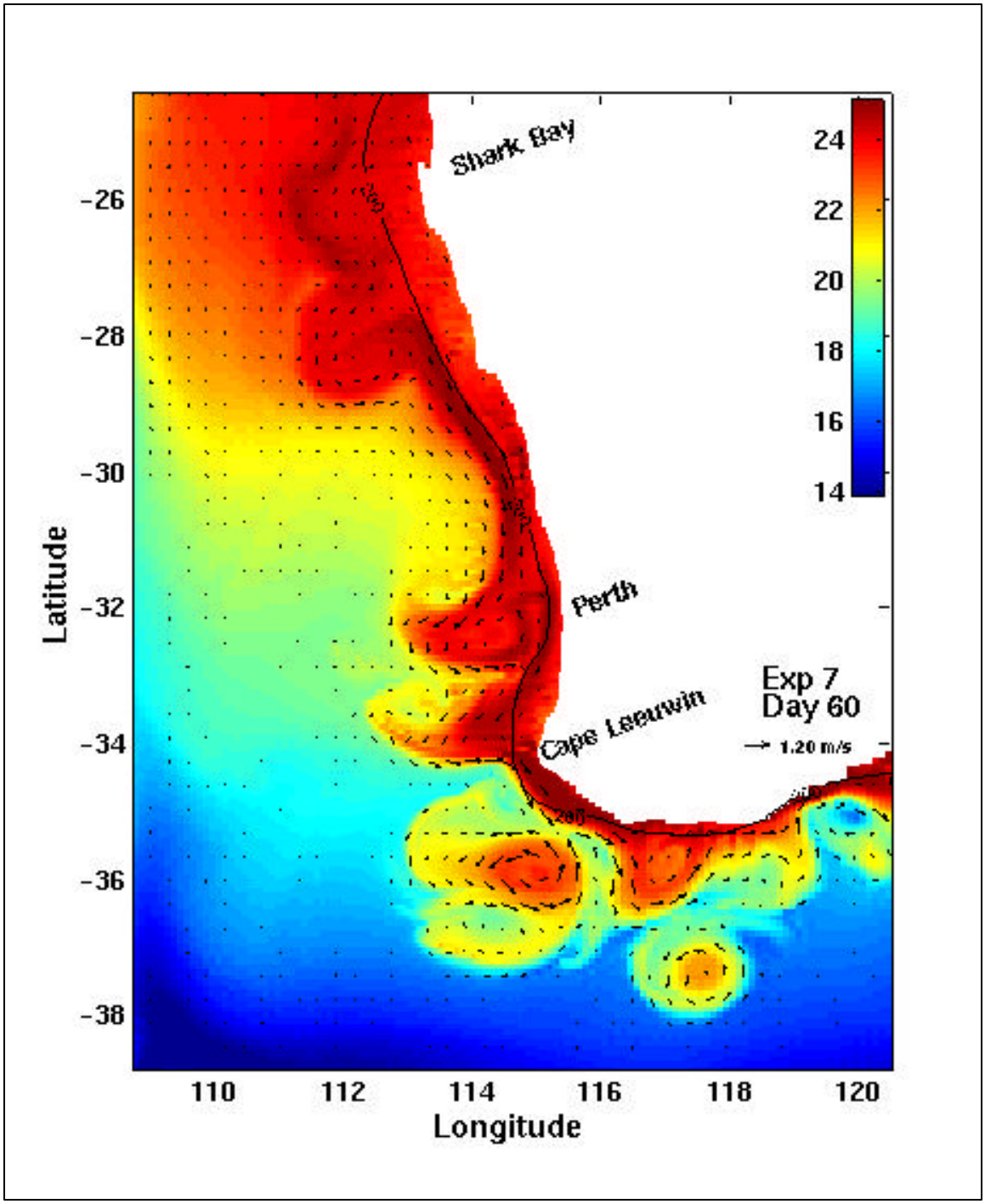

Figure 15e. Surface temperature (°C) and velocity vectors for Experiment 7 on day 60.

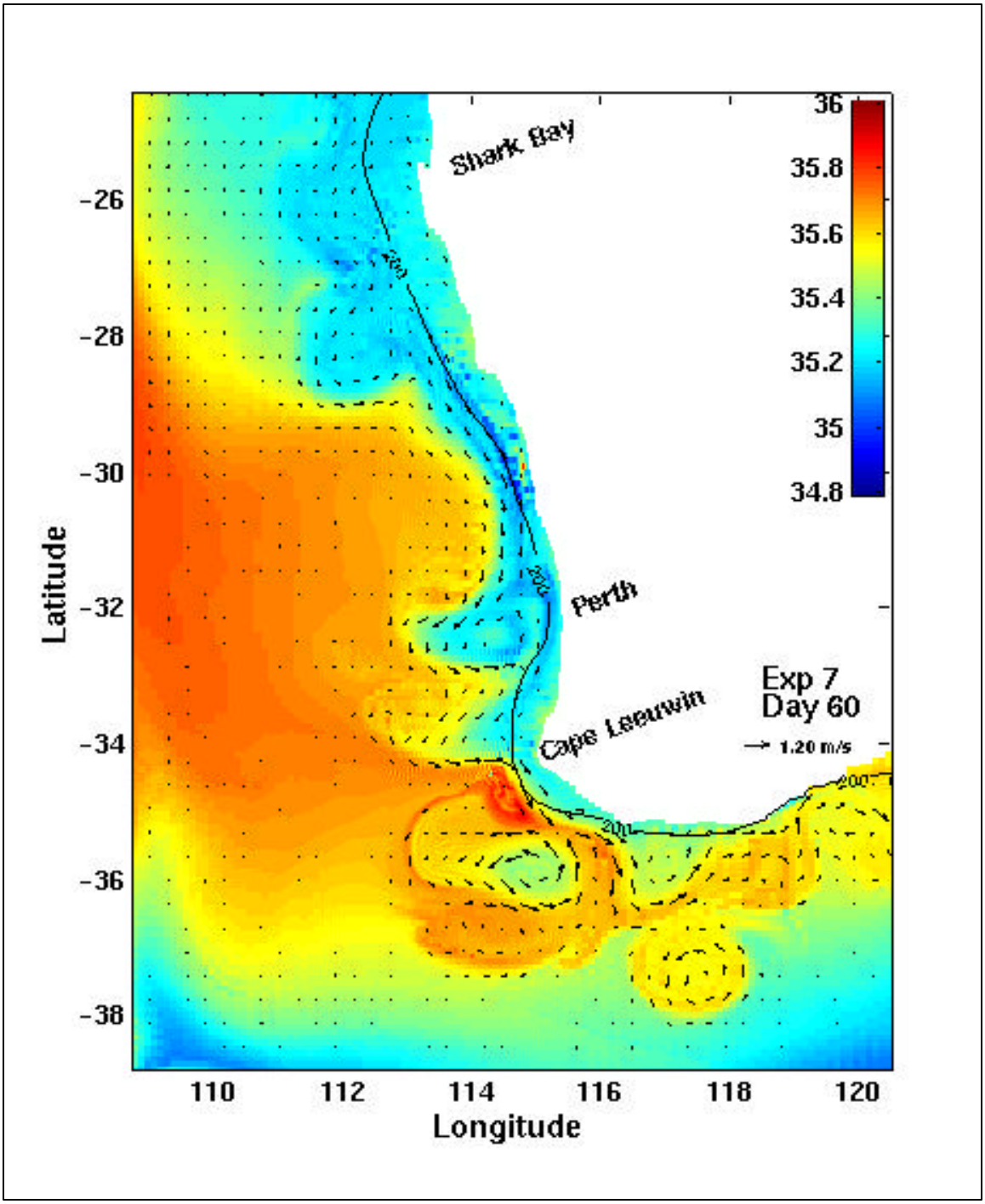

Figure 15f. Surface salinity and velocity vectors for Experiment 7 on day 60.

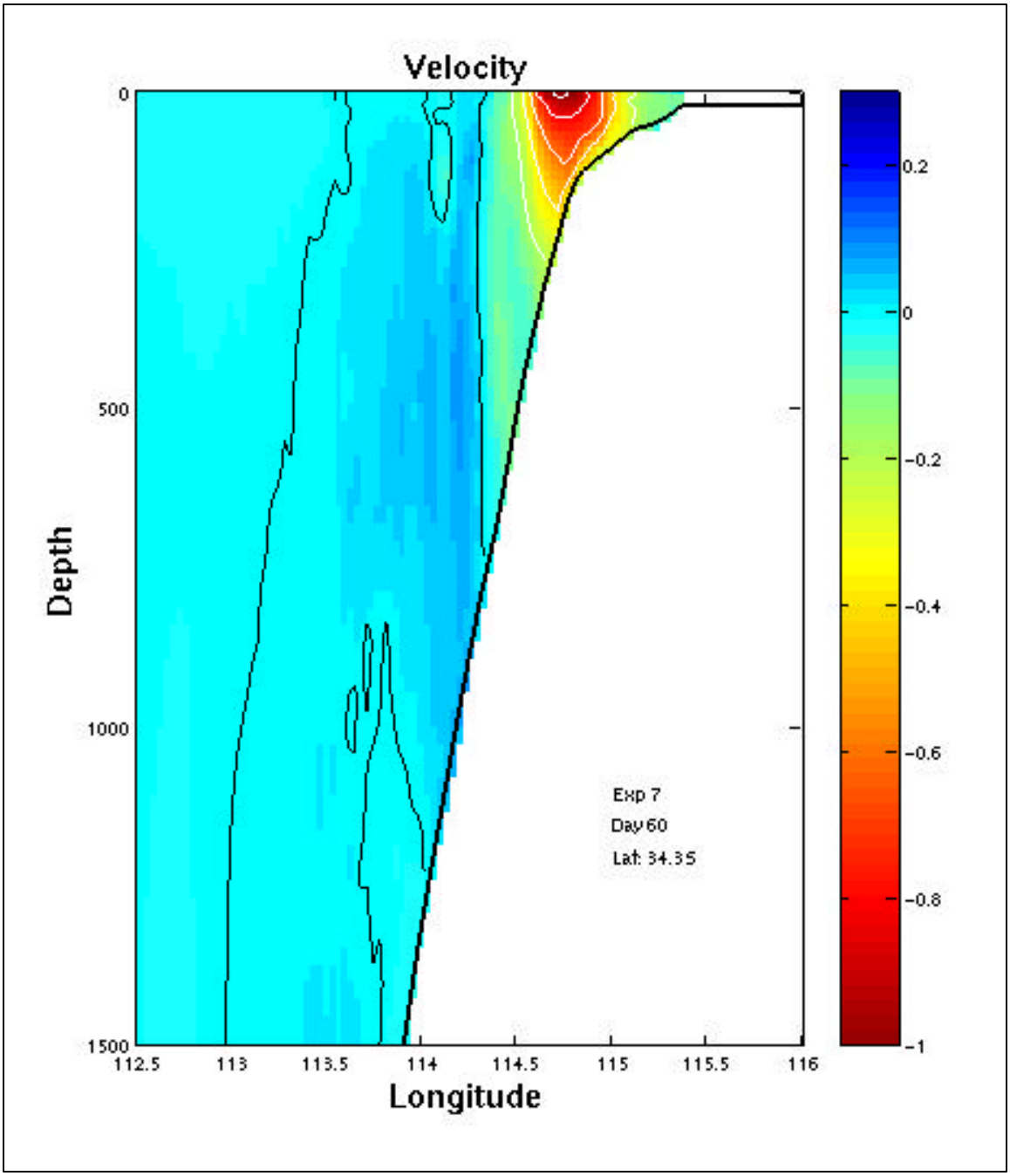

Figure 15g. Cross-section of north-south velocities (m/s) at Cape Leeuwin (34.3°S) for Experiment 7 day 60. Blue is equatorward (north).

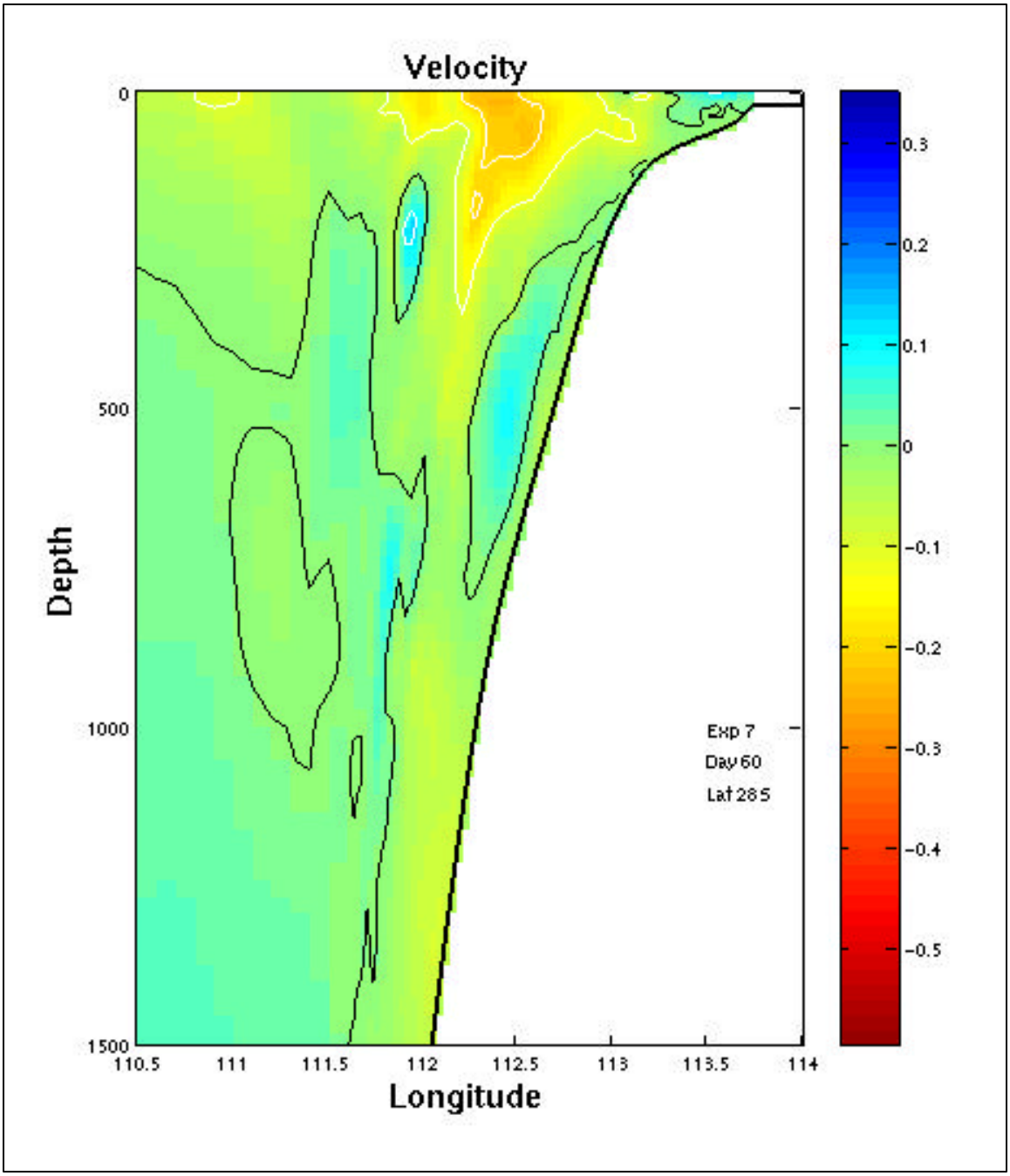

Figure 15h. Cross-section of north-south velocities (m/s) at 28°S for Experiment 7 day 60. Blue is equatorward (north).

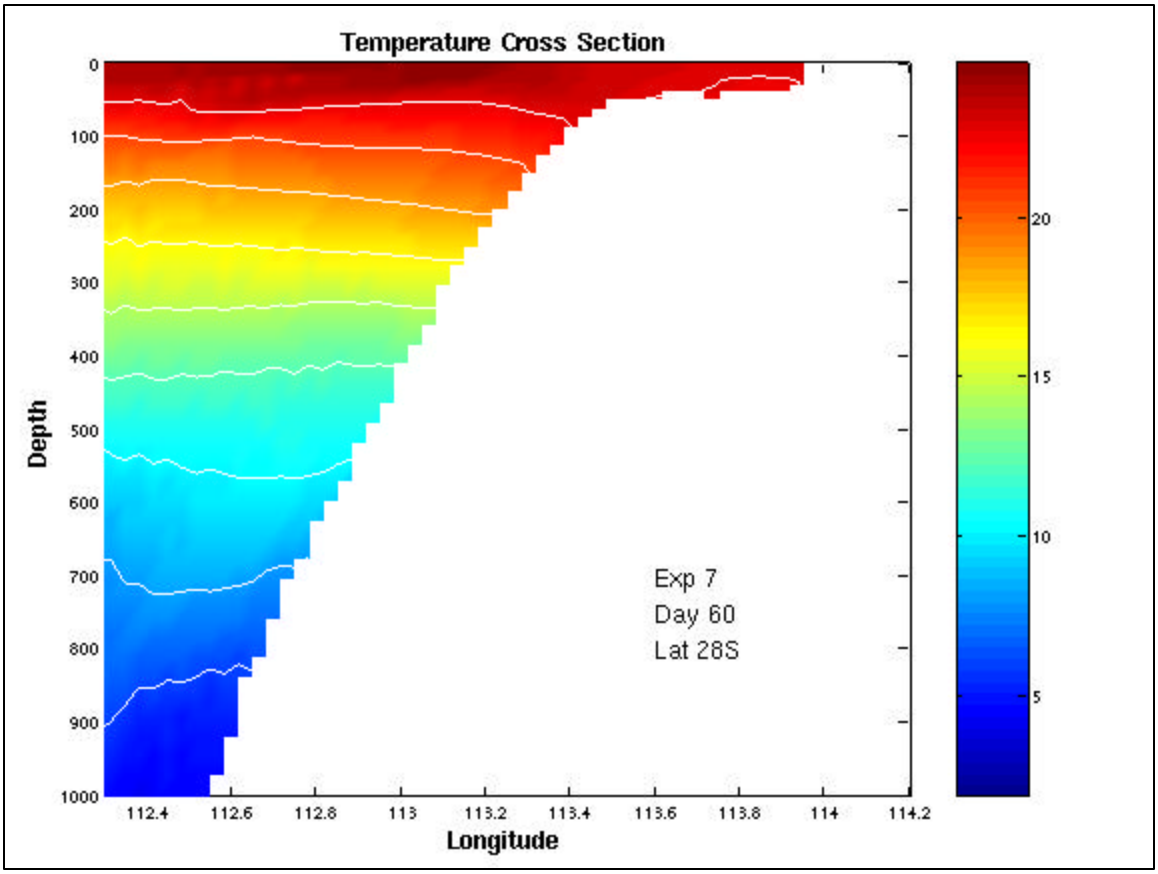

Figure 15i. Cross-section of temperature (ºC) at 26ºS for Experiment 7 day 60, with a contour interval of two degrees.

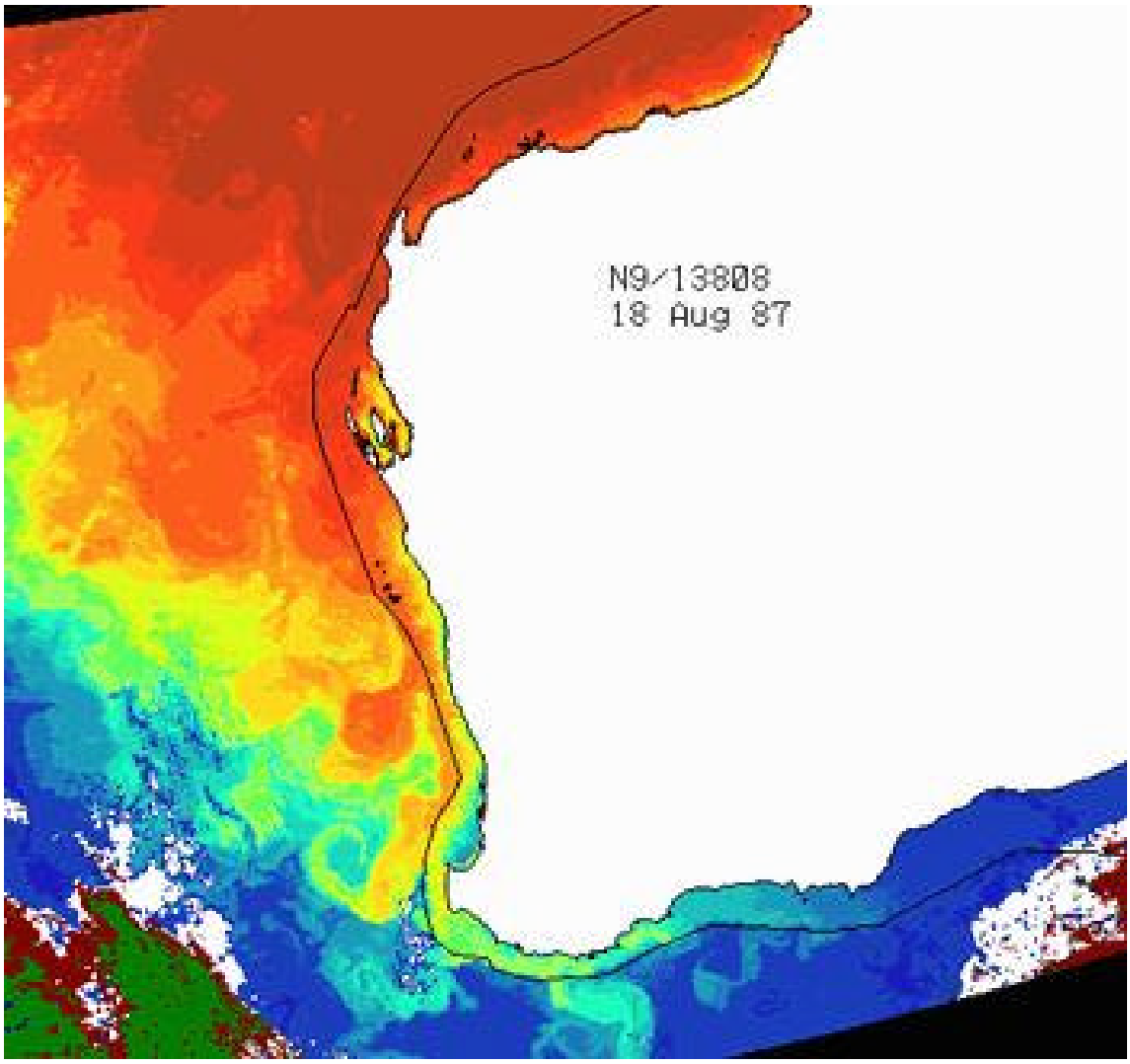

Figure 16. Satellite image of surface water temperatures off Western Australia in August 1987, showing the warm waters of the Leeuwin Current (red/orange) and the cooler offshore water in green/blue. The white and mottled blue areas are clouds, and the black line represents the edge of the continental shelf(CSIRO, Marine Research).

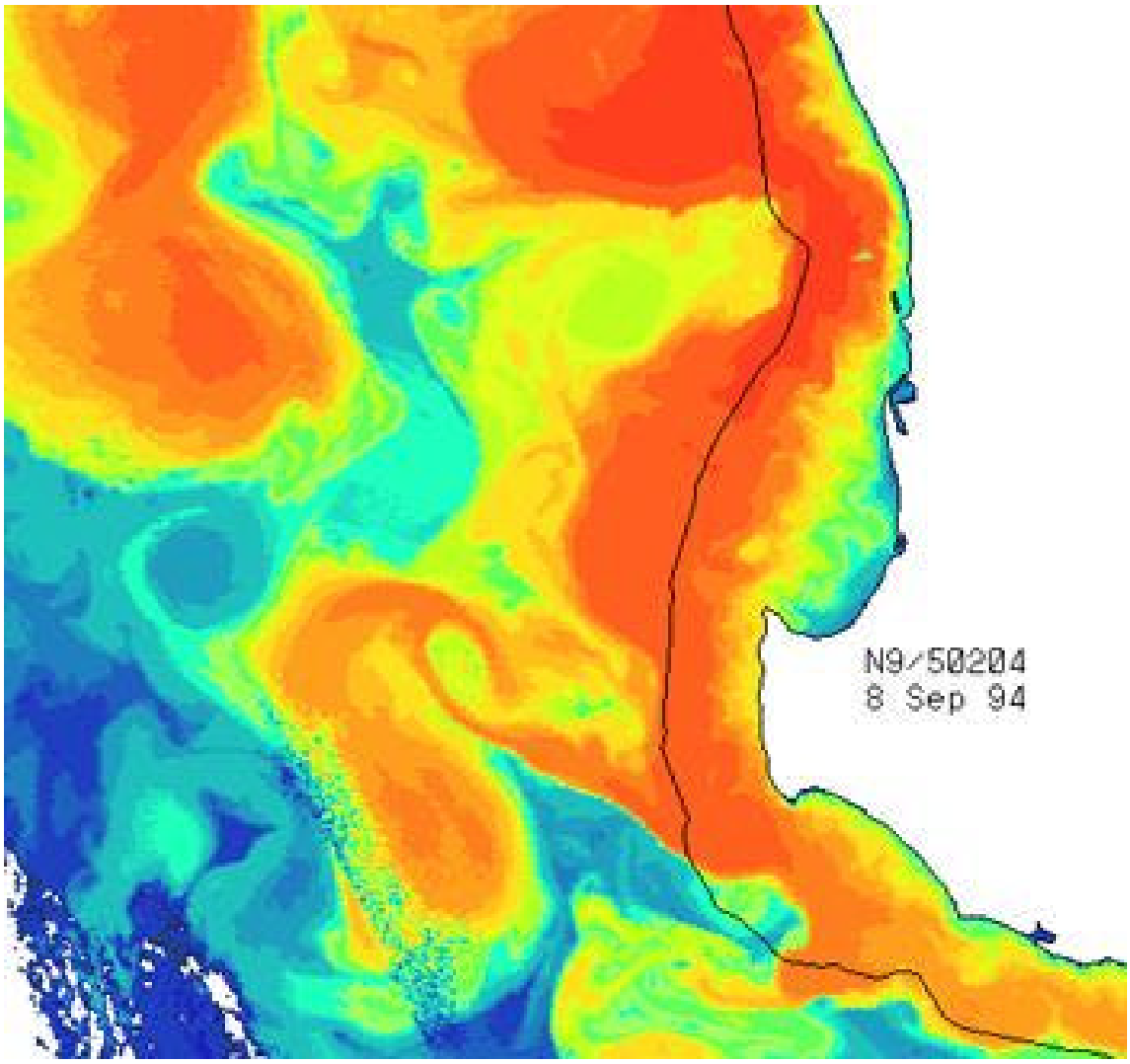

Figure 17. Satellite image of surface water temperatures off Western Australia in September 1994, showing the warm waters of the Leeuwin Current (red/orange) and the cooler offshore water in green/blue. The white and mottled blue areas are clouds, and the black line represents the edge of the continental shelf(CSIRO, Marine Research).

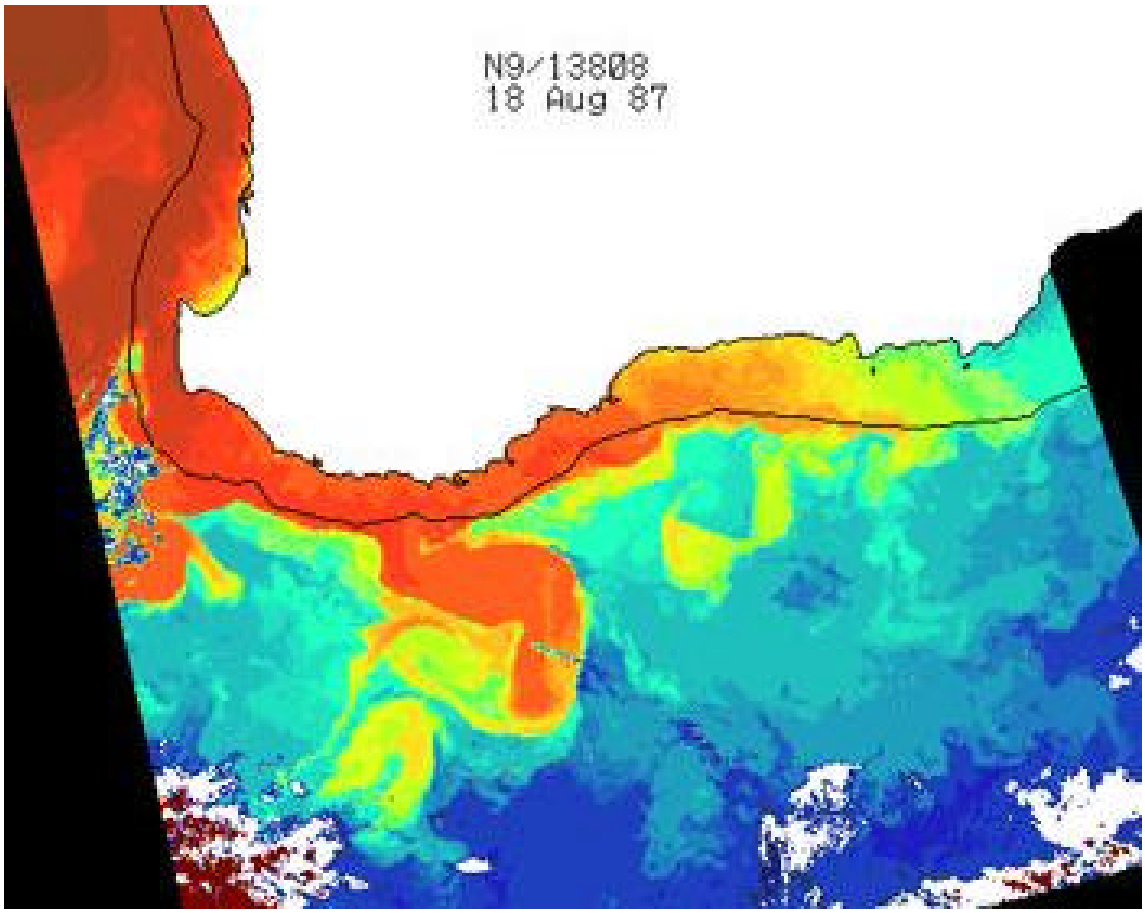

Figure 18. Satellite image of surface water temperatures off Western Australia in August 1987, showing the warm waters of the Leeuwin Current (red/orange) and the cooler offshore water in green/blue. The white and mottled areas are clouds, and the black line represents the edge of the continental shelf(CSIRO, Marine Research).

Exp #	Annual Wind	Climatology	Topography
1	YES	HORIZONTALLY AVERAGED	NO
2	NO	FULL	NO
3	YES	FULL	NO
4	NO	HORIZONTALLY AVERAGED	YES
5	YES	HORIZONTALLY AVERAGED	YES
6	NO	FULL	YES
7	YES	FULL	YES

Table 1. Summary of experimental design.

Level	Depth (m)	Level	Depth (m)	Level	Depth (m)
1	0	12	300	23	1400
2	10	13	400	24	1500
3	20	14	500	25	1750
4	30	15	600	26	2000
5	50	16	700	27	2500
6	75	17	800	28	3000
7	100	18	900	29	3500
8	125	19	1000	30	4000
9	150	20	1100	31	4500
10	200	21	1200	32	5000
11	250	22	1300	33	5500

Table 2. Vertical levels and depths used by Levitus and Boyer (1994) and Levitus et al. (1994)

Level	Sigma Value	Level	Sigma Value
1	0	12	-0.61538
2	-0.00961	13	-0.69231
3	-0.01923	14	-0.76923
4	-0.03846	15	-0.84615
5	-0.07692	16	-0.92308
6	-0.15385	17	-0.96154
7	-0.23077	18	-0.98077
8	-0.30769	19	-0.99038
9	-0.38462	20	-0.99519
10	-0.46154	21	-1.0
11	-0.53846		

Table 3. Values of sigma levels

LIST OF REFERENCES

Batteen, M. L. and C. L. Butler, Modeling Studies of the Leeuwin Current Off Western and Southern Australia, *J. Phys. Oceanography*, 28, 2199-2221, 1998.

Batteen, M. L. and M.-J. Huang, The Effect of Salinity on Density in the Leeuwin Current System, *J. Geophys. Res.,* 103(C11), 24,693-24,721, 1998.

Batteen, M. L., R. L. Haney, T. A. Tiekling and P. G. Renaud, 1989, A Numerical Study of Wind Forcing of Eddies and Jets in the California Current System. *J. Mar. Research,* 47(3), 493-523, 1989.

Batteen, M. L., M. J. Rutherford, and E. J. Bayler, A Numerical Study of Wind and Thermal Forcing Effects on the Ocean Circulation Off Western Australia, *J. Phys. Oceanography*, 22, 1406-1433, 1992.

Batten, M. L., T. J. Tworek, and A. W. Cox, Modeling Studies of the Effects of Seasonal Wind Forcing and Thermohaline Gradients on the Leeuwin Current System, *Progress in Oceanography*, 2000, submitted.

Blumberg, A. F., and G. L. Mellor, A Description of a Three-Dimensional Coastal Ocean Circulation Model, In: *Three-Dimensional Coastal Ocean Models, Coastal Estuarine Sci*., 4, edited by N. Heaps, pp 1-16, AGU, Washington, DC, 1987.

Chapman, D. C., Numerical Treatment of Cross-Shelf Open Boundaries in a Barotropic Coastal Ocean Model, *Journal of Phys. Oceanography*, 25, 1060-1075, 1985.

Church, J. A., G. R. Cresswell, and J. S. Godfrey, The Leeuwin Current. In: *Poleward Flows Along Eastern Ocean Boundaries*, S. Neshhyba, C. N. K. Moorers, R. I. Smith, and R. T. Barber, Eds., Springer-Verlag, 230-252, 1989.

“Commonwealth Scientific & Industrial Research Organisation (CSIRO)”, http://www.csiro.au/.

Cresswell, G. R. and T. J. Golding, Observations of a South-Flowing Current in the Southeastern Indian Ocean, *Deep-Sea Res.*, 27A, 449-466, 1980.

Cresswell, G. R. and J. L. Peterson, The Leeuwin Current South of Western Australia, *Aust. J. Mar. Freshwater Res.*, 44, 285-303, 1993.

Ezer, T. and G. L. Mellor, Diagnostic and Prognostic Calculations of the North Atlantic Circulation and Sea Level Using a Sigma Coordinate Ocean Model, *J. of Geophys. Res.*, 99(C7), 14159-14171, 1994.

Ezer, T. and G. L. Mellor, Simulations of the Atlantic Ocean With a Free Surface Sigma Coordinate Ocean Model, *J. of Geophys. Res.*, 102(C7), 15647-15657, 1997.

Godfrey, J. S. and K. R. Ridgway, The Large-Scale Environment of the Poleward-Flowing Leeuwin Current, Western Australia: Longshore Steric Height Gradients, Wind Stresses and Geostrophic Flow, *J. Phys. Oceanography*, 15, 481-495, 1985.

Gill, A., *Atmosphere-Ocean Dynamics*. International Geophysics Series, 30, 662 pp, 1982.

Godfrey, J. S., D. J. Vaudrey, and S. D. Hahn, Observations of the Shelf-Edge Current South of Australia Winter 1982, *J. Phys. Oceanography*, 16, 668-679, 1986.

Hirst, A. C., and J. S. Godfrey, The role of Indonesian Throughflow in a Global Ocean GCM, *J. Phys. Oceanography*, 23,1057-1086, 1993.

Levitus, S., and T. P. Boyer, World Ocean Atlas 1994, Vol. 4: Temperature, *NOAA Atlas NESDI 4*, 117 pp., U. S. Dept. of Commerce, Washington, D.C., 1994.

Levitus, S., R. Burgett, and T. P. Boyer, World Ocean Atlas 1994, Vol. 3: Salinity, *NOAA Atlas NESDI 3*, 99 pp., U. S. Dept. of Commerce, Washington, D.C., 1994.

Marchesiello, P., J. C. McWilliams, and A. Shchepetkin, Open Boundary Conditions for Long-Term Integration of Regional Oceanic Models, *Ocean Modeling*, 3, 1-20, 2001.

Martinho, A. C., A Fine Resolution Model of the Coastal Eastern Boundary Current Systems Off Iberia and Morocco, Masters Thesis, Naval Postgraduate School, Monterey, CA, 93 pp, 2001.

McCreary, J. P., S. R. Shetye, and P. K. Kundu, Thermohaline Forcing of Eastern Boundary Currents: With Application to the Circulation Off the West Coast of Australia, *J. Mar. Res.*, 44, 71-92, 1986.

Mellor, G. L., User's guide for a Three-Dimensional, Primitive Equation, Numerical Ocean Model, 40 pp, Program in Atmos. And Ocean Sci. Report, Princeton Univ., Princeton, NJ 1996.

Mellor, G. L., L. Y. Oey, and T. Ezer, Sigma Coordinate Pressure Gradient Errors and the Seamount Problem, *J. Atmospheric and Ocean Technology*, 15, 1122-1131, 1998.

Mellor, G. L., and T. Yamada, Development of a Turbulence Closure Model for Geophysical Fluid Problems, *Rev. Geophys. Space Phys*., 20, 851-875, 1982.

Palma, E. D., and R. P. Matano, On the Implementation of Passive Open Boundary Conditions for a General Circulation Model: the Barotropic Mode, *J. Geophys. Res.*, 103(C1), 1319-1341, 1998.

Palma, E. D., and R. P. Matano, On the Implementation of Passive Open Boundary Conditions for a General Circulation Model: the Three-Dimensional Case, *Journal of Geophysical Research*, 105(C4), 8605-8627, 2000.

Parrish, R. H., A. Bakun, D. M. Husby, and C. S. Nelson, Comparitive Climatology of Selected Environmental Processes in Relation to Eastern Boundary Current Pelagic Fish Reproduction. In: *Proc. Expert Consultation to Examine Changes in Abundance and Species of Neritic Fish Resources*, G. D. Sharp and J. Csirke, Eds., San Jose, Costa Rica, FAO Fish Rep. 291, Vol. 3, 731-778, 1983.

Pearce, A. F. and R. W. Griffiths (1991). The mesoscale structure of the Leeuwin Current : a comparison of laboratory model and satellite images. Journal of Geophysical Research 96, 16739-16757.

Sandwell, D. T., and W. F. Smith, Global Bathymetric Prediction for Ocean Modeling and Marine Geophysics, 1996.

Smagorinsky, J., S. Manabe, and J. L. Holloway, Numerical Results From a Nine-Level General Circulation Model of the Atmosphere, *Mon. Weather Rev.,* 93, 727-768, 1965.

Smith, R. L., A. Huyer, J. S. Godfrey, and J. A. Church, The Leeuwin Current Off Western Australia, 1986-1987, *J. Phys. Oceanography*, 21, 323-345, 1991.

Thompson, R. O. R. Y., Observations of the Leeuwin Current Off Western Australia, *J. Phys. Oceanography*, 14, 623-628, 1984.

Thompson, R. O. R. Y., Continental-Shelf Scale Model of the Leeuwin Current, *J. Mar. Res.*, 45, 813-827, 1987.

Trenberth, K. E., W. G. Large, J. G. Olsen, The Mean Annual Cycle in Global Ocean Wind Stress, *J. Phys. Oceanography*, 20, 1742-1760, 1990.

Wooster, W. S., and J. L. Reid Jr., Eastern boundary currents, in *The Seas*, Vol. 2, edited by M. N. Hill, pp. 253-280, John Wiley, New York, 1963.

INITIAL DISTRIBUTION LIST

1. Defense Technical Information Center
   Ft. Belvoir, VA

2. Dudley Knox Library
   Naval Postgraduate School
   Monterey, CA

3. Chairman, Department of Oceanography
   (Code OC/Bv)
   Naval Postgraduate School
   Monterey, CA

4. Dr. Mary L. Batteen (Code OC/Bv)
   Naval Postgraduate School
   Monterey, CA

5. Dr. Curtis Collins (Code OC/Co)
   Naval Postgraduate School
   Monterey, CA

6. LT Richard Kennedy
   632 Analii St
   Diamondhead, MS 39525

7. Maury Oceanographic Library
   Naval Oceanographic Office
   1100 Balch Blvd
   Stennis Space Center, MS 39529